

WASHINGTON UNIVERSITY

Sever Institute
School of Engineering and Applied Science

Department of Mechanical, Aerospace and Structural Engineering

Dissertation Examination Committee:

David A. Peters, Chair

Philip V. Bayly

Kenneth L. Jerina

Swami Karunamoorthy

Ervin Y. Rodin

Michael A. Swartwout

APPLYING DYNAMIC WAKE MODELS TO INDUCED POWER CALCULATIONS FOR
AN OPTIMUM ROTOR

by

Cristina Garcia-Duffy

A dissertation presented to the
Graduate School of Arts and Sciences
of Washington University in
partial fulfillment of the
requirements for the degree
of Doctor of Philosophy

December 2008

Saint Louis, Missouri

Revised August 2009

Report Documentation Page				Form Approved OMB No. 0704-0188	
Public reporting burden for the collection of information is estimated to average 1 hour per response, including the time for reviewing instructions, searching existing data sources, gathering and maintaining the data needed, and completing and reviewing the collection of information. Send comments regarding this burden estimate or any other aspect of this collection of information, including suggestions for reducing this burden, to Washington Headquarters Services, Directorate for Information Operations and Reports, 1215 Jefferson Davis Highway, Suite 1204, Arlington VA 22202-4302. Respondents should be aware that notwithstanding any other provision of law, no person shall be subject to a penalty for failing to comply with a collection of information if it does not display a currently valid OMB control number.					
1. REPORT DATE 28 SEP 2009		2. REPORT TYPE		3. DATES COVERED 01-04-2005 to 30-09-2008	
4. TITLE AND SUBTITLE Applying Dynamic Wake Models to Induced Power Calculations for an Optimum Rotor				5a. CONTRACT NUMBER W911NF-05-1-0096	
				5b. GRANT NUMBER	
				5c. PROGRAM ELEMENT NUMBER	
6. AUTHOR(S)				5d. PROJECT NUMBER 61102	
				5e. TASK NUMBER	
				5f. WORK UNIT NUMBER	
7. PERFORMING ORGANIZATION NAME(S) AND ADDRESS(ES) Washington University Research Office, 276 North Skinker Bldg., 2nd Floor, St. Louis, MO, 63130-4899				8. PERFORMING ORGANIZATION REPORT NUMBER ; 46665-EG.1	
9. SPONSORING/MONITORING AGENCY NAME(S) AND ADDRESS(ES)				10. SPONSOR/MONITOR'S ACRONYM(S)	
				11. SPONSOR/MONITOR'S REPORT NUMBER(S) 46665-EG.1	
12. DISTRIBUTION/AVAILABILITY STATEMENT Approved for public release; distribution unlimited					
13. SUPPLEMENTARY NOTES					
14. ABSTRACT This work continues previous inflow work in that it extends it to the flow below the disk both in and out of the shed wake. In addition, the work utilizes that new inflow model to offer optimum power states for rotors in hover and in forward flight.					
15. SUBJECT TERMS					
16. SECURITY CLASSIFICATION OF:			17. LIMITATION OF ABSTRACT Same as Report (SAR)	18. NUMBER OF PAGES 192	19a. NAME OF RESPONSIBLE PERSON
a. REPORT unclassified	b. ABSTRACT unclassified	c. THIS PAGE unclassified			

ABSTRACT OF THE DISSERTATION

Applying Dynamic Wake Models

to Induced Power Calculations

for an Optimum Rotor

by

Cristina Garcia-Duffy

Doctor of Philosophy in Aerospace Engineering

Washington University in Saint Louis, 2008

Professor David. A. Peters, Chairperson

Recent studies have pointed out that conventional lifting rotors in forward flight have efficiencies far lower than the optimum efficiencies predicted by theory.

This dissertation explains how a closed-form optimization of induced power with finite-state models is expanded to successfully reproduce the results for the optimization of induced power given by classical theories for axial flow and for a rotor in forward flight. Results for induced power change in forward flight and for different conditions will help the determination of what produces the efficiency in real rotors to be inferior to the predicted values by theoretical calculations.

Mainly three factors contribute to the decreased efficiency for real rotors: a finite number of blades, the effect of lift tilt and the lift distribution. The ultimate goals of the present research effort are to: 1) develop a complete and comprehensive inflow model, and 2) determine which of these contribute to the drastic increase in induced power.

Acknowledgments

I would like to thank Dr. David A. Peters for his support throughout the years. It has been a pleasure to know him. He is the most enthusiastic and supportive of advisors.

Thank you to the members of my committee —Dr. Philip Bayly, Dr. Kenneth Jerina, Dr. Swami Karunamoorthy, Dr. Ervin Rodin and Dr. Michael Swartwout— for their support.

This work was sponsored by the Army Research Office, Agreement #DAAD19-01-1-0697, Tom Doligalski, Technical Monitor.

Cristina Garcia-Duffy

Washington University in St. Louis

December 2008

To my husband, my parents and my sister. Os quiero.

Contents

Abstract	ii
Acknowledgements	iii
List of Tables	vii
List of Figures	viii
Nomenclature	x
Chapter 1 Introduction	1
1.1 Previous Work	5
1.1.1 Classical Work on Optimally Efficient Propellers	5
1.1.2 Classical Work on Inflow Theories	7
1.1.3 Motivation of Optimization Work	10
1.2 Optimization Problem Statement	12
1.3 Present Approach	14
Chapter 2 Complete Inflow Theory Formulation	16
2.1 Potential Flow Equations	17
2.2 Pressure Potentials	19
2.3 Velocity Potentials	21
2.4 Galerkin Approach	25
2.5 Equations in Terms of Derived Potentials	29
2.6 Effect of Lift Tilt	33
2.7 Velocity in Lower Hemisphere	35
2.8 Nonlinearities	38
2.9 Results from previous models	42
Chapter 3 Development of the Solution Approach	44
3.1 Induced Power Derivation from He-Peters Model	45
3.2 Induced Power Theorem	51
3.3 General Optimization	55
3.4 General Figure of Merit Definition	56
Chapter 4 Results	58
4.1 Classical Theories: Axial and Skewed Flows	58
4.1.1 Momentum Theory	58
4.1.2 Prandtl's Approximation	63
4.1.3 Betz Distribution	64

4.1.4	Goldstein's Distribution	66
4.2	Finite-State Methods: Axial Flow	67
4.2.1	Optimization	68
4.2.2	Figure of Merit	71
4.2.3	Infinite Number of Blades	74
4.2.4	Finite Number of Blades	92
4.3	Finite-State Methods: Skewed Flow	100
4.3.1.	Infinite Number of Blades	100
4.3.2.	Finite Number of Blades	132
4.4	Special Case of Hover	135
4.4.1.	Closed-Form Results in Hover	136
4.4.2.	Example Calculation	141
Chapter 5	Summary, Conclusions and Future Work	145
5.1	Summary and Conclusions	145
5.2	Future Work	147
5.2.1.	Theory	147
5.2.2.	Optimization	148
Appendix A	Ellipsoidal Coordinate System	149
Appendix B	Normalized Associated Legendre Functions	153
Appendix C	General Galerkin Method	155
Appendix D	Transformation Matrices in Closed Form	157
Appendix E	Table Method	158
Appendix F	Influence coefficients as fit of $\text{Cos}\varphi$	163
References	172
Vita	175

List of Tables

Table 1.1:	Cases studied using finite state methods	3
Table 4.1:	Cases for F.M., Pressure and Inflow Figures	104
Table E.1:	Choice for the number of spatial modes.....	158
Table E.2:	Figure of Merit for various Number of Harmonics	160

List of Figures

Figure 1.1: Harris' power coefficient with advance ratio plot for a helicopter.....	11
Figure 1.2: Basic illustrative problem for a rotor, [22]	13
Figure 2.1: Regions on, off and around an actuator disk.....	17
Figure 2.2: Coordinate system	18
Figure 3.1: Normalized velocity components.....	49
Figure 3.2: Inflow velocity components for a moving rotor.....	51
Figure 3.3: Rotor blade generic position and rotating angle	52
Figure 3.4: Geometry of the forces on the blade.....	53
Figure 3.5: Geometry of the flow.....	54
Figure 4.1: Flow model for an actuator disk in axial flow	60
Figure 4.2: Prantl and Goldstein circulation distributions	67
Figure 4.3: Optimum pressure distribution for an actuator disk in axial flow	77
Figure 4.4: Optimum velocity distribution for an actuator disk in axial flow.....	78
Figure 4.5: Optimum lift distribution for an actuator disk in axial flow	78
Figure 4.6: Pressure Distribution, $\chi = 0$, $v = 0.0$, FM=1.0	79
Figure 4.7: Pressure Distribution, $\chi = 0$, $v = 0.2$, FM=0.87	79
Figure 4.8: Pressure Distribution, $\chi = 0$, $v = 0.4$, FM=0.69	80
Figure 4.9: Pressure Distribution, $\chi = 0$, $v = 0.6$, FM=0.52	80
Figure 4.10: Pressure Distribution, $\chi = 0$, $v = 0.8$, FM=0.40.....	81
Figure 4.11: Pressure Distribution, $\chi = 0$, $v = 1.0$, FM=0.31.....	81
Figure 4.12: Induced Velocity Distribution, $\chi = 0$, $v = 0.0$, FM=1.0.....	82
Figure 4.13: Induced Velocity Distribution, $\chi = 0$, $v = 0.2$, FM=0.81.....	82
Figure 4.14: Induced Velocity Distribution, $\chi = 0$, $v = 0.4$, FM=0.69.....	83
Figure 4.15: Induced Velocity Distribution, $\chi = 0$, $v = 0.6$, FM=0.52.....	83
Figure 4.16: Induced Velocity Distribution, $\chi = 0$, $v = 0.8$, FM=0.40.....	84
Figure 4.17: Induced Velocity Distribution, $\chi = 0$, $v = 1.0$, FM=0.31.....	84
Figure 4.18: Figure of merit comparison of the finite-state to Betz distribution	89
Figure 4.19: Figure of merit versus climb rate for different thrust coefficients.....	90
Figure 4.20: Induced power coefficient versus climb rate	91
Figure 4.21: Effect of tip loss on figure of merit, lightly-loaded rotor.....	93
Figure 4.22: Induced power coefficient for various numbers of blades ($C_T=0.02$)	96
Figure 4.23: Circulation at any blade radial location, $Q=2$	98
Figure 4.24: Circulation at any blade radial location, $Q=4$	99
Figure 4.25: Figure of Merit change with Skew Angle. 20 harmonics.....	105
Figure 4.26: Figure of Merit change with Total Inflow. 20 harmonics	105
Figure 4.27: Figure of Merit change with Skew Angle. 1 harmonic	106
Figure 4.28: Figure of Merit change with Total Inflow. 1 harmonics	106
Figure 4.29: FM change with Skew Angle. 20 harm., constrained inflow states.....	107
Figure 4.30: FM change with Total Inflow. 20 harm., constrained inflow states	107

Figure 4.31 Pressure Distribution, $\chi = 30, \nu = 0.0, FM=1.0$	113
Figure 4.32: Pressure Distribution, $\chi = 30, \nu = 0.2, FM=0.89$	113
Figure 4.33: Pressure Distribution, $\chi = 30, \nu = 0.4, FM=0.72$	114
Figure 4.34: Pressure Distribution, $\chi = 30, \nu = 0.6, FM=0.56$	114
Figure 4.35: Pressure Distribution, $\chi = 30, \nu = 0.8, FM=0.44$	115
Figure 4.36: Pressure Distribution, $\chi = 30, \nu = 1.0, FM=0.36$	115
Figure 4.37: Induced Velocity Distribution, $\chi = 30, \nu = 0.0, FM=1.0$	116
Figure 4.38: Induced Velocity Distribution, $\chi = 30, \nu = 0.2, FM=0.89$	116
Figure 4.39: Induced Velocity Distribution, $\chi = 30, \nu = 0.4, FM=0.72$	117
Figure 4.40: Induced Velocity Distribution, $\chi = 30, \nu = 0.6, FM=0.56$	117
Figure 4.41: Induced Velocity Distribution, $\chi = 30, \nu = 0.8, FM=0.44$	118
Figure 4.42: Induced Velocity Distribution, $\chi = 30, \nu = 1.0, FM=0.36$	118
Figure 4.43: Pressure Distribution, $\chi = 60, \nu = 0.0, FM=1.0$	119
Figure 4.44: Pressure Distribution, $\chi = 60, \nu = 0.2, FM=0.94$	119
Figure 4.45: Pressure Distribution, $\chi = 60, \nu = 0.4, FM=0.84$	120
Figure 4.46: Pressure Distribution, $\chi = 60, \nu = 0.6, FM=0.72$	120
Figure 4.47: Pressure Distribution, $\chi = 60, \nu = 0.8, FM=0.62$	121
Figure 4.48: Pressure Distribution, $\chi = 60, \nu = 1.0, FM=0.54$	121
Figure 4.49: Induced Velocity Distribution, $\chi = 60, \nu = 0.0, FM=1.0$	122
Figure 4.50: Induced Velocity Distribution, $\chi = 60, \nu = 0.2, FM=0.94$	122
Figure 4.51: Induced Velocity Distribution, $\chi = 60, \nu = 0.4, FM=0.84$	123
Figure 4.52: Induced Velocity Distribution, $\chi = 60, \nu = 0.6, FM=0.72$	123
Figure 4.53: Induced Velocity Distribution, $\chi = 60, \nu = 0.8, FM=0.62$	124
Figure 4.54: Induced Velocity Distribution, $\chi = 60, \nu = 1.0, FM=0.54$	124
Figure 4.55: Pressure Distribution, $\chi = 90$, all values of ν , $FM=1.0$	125
Figure 4.56: Induced Velocity Distribution, $\chi = 90$, all values of ν , $FM=1.0$	125
Figure 4.57: XY-plane View of Pressure Distribution, $\chi = 60$, various ν	126
Figure 4.58: XZ-plane View of Pressure Distribution, $\chi = 60$, various ν	127
Figure 4.59: YZ-plane View of Pressure Distribution, $\chi = 60$, various ν	128
Figure 4.60: XY-plane View of Induced Velocity Distribution, $\chi = 60$, various ν	129
Figure 4.61: XZ-plane View of Induced Velocity Distribution, $\chi = 60$, various ν	130
Figure 4.62: YZ-plane View of Induced Velocity Distribution, $\chi = 60$, various ν	131
Figure 4.63: Figure of merit variation with thrust coefficient in hover.....	142
Figure 4.64: Figure of merit variation with thrust coefficient for a NACA 0012.....	143
Figure 4.64: Optimum figure of merit change with drag-to-lift ratio effect.....	144
Figure A.1: Ellipsoidal Coordinate System, xz -plane view	150
Figure A.2: Ellipsoidal Coordinate System Contour, $\eta = 0.4$, all ν , all $\bar{\psi}$	151
Figure A.3: Ellipsoidal Contour, $\nu = 0.4$ for $\bar{x} \leq 0$, $\nu = -0.4$ for $\bar{x} \geq 0$, all η , all $\bar{\psi}$	152
Figure E.1: Figure of Merit for Different Number of Harmonics	161
Figure E.2: Close-up of Figure of Merit versus the Number of Harmonics.....	162
Figure F.1: $\nu \cos\varphi$ Distribution to be fitted by Legendre-function representation.....	164
Figure F.2: Legendre-function Representation of $\nu \cos\varphi$	165
Figure F.3: views for: a) Formula and b) Influence Legendre-function	168
Figure F.4: $\cos(\varphi)$ fit for $\mu=0.5196, \lambda=0.3, \psi=10$ and 190°	169
Figure F.5: $\cos(\varphi)$ fit for $\mu=0.5196, \lambda=0.3, \psi=60$ and 240°	169
Figure F.6: $\cos(\varphi)$ fit for $\mu=0.5196, \lambda=0.3, \psi=120$ and 300°	170
Figure F.7: Top view of Rotor. Advancing side is for $0 < \psi < 180^\circ$	171

Nomenclature

a_n^m, b_n^m	velocity components, prime potentials, m/sec
\hat{a}, \hat{b}	velocity components, derived potentials, m/sec
$[A_{nj}^m]$	transformation matrix, special case of the matrix \tilde{L}
$[B_{nj}^m]$	ideal inverse transformation matrix
C_n^m, D_n^m	Fourier expansion coefficients for the pressure
C_p	power coefficient
C_{PI}	induced power coefficient
C_T	thrust coefficient
$[D^e], [D^s]$	velocity coupling matrices
$[E_{nj}^{m0}]$	expansion transformation matrix
f^m	blending factor
H	rotor inplane force
H_n^m	factorial combination
i	imaginary number
$\hat{i}, \hat{j}, \hat{k}$	unit vectors
$[I]$	identity matrix

j, n	polynomial number
k	Prandtl's tip loss correction factor
K_n^m	kinetic energy matrix, mass diagonal
L_q	blade loading
$[\tilde{L}^c], [\tilde{L}^s]$	basis transforms, cosine and sine parts for the L -matrix
$[\bar{\bar{L}}]$	\tilde{L} -matrix with the elements where $m = 0$ are multiplied by two
m, r	harmonic number
$[M^c], [M^s]$	mass matrices, Morillo-Peters model
N	largest value of n
P_I	induced power
P_s	shaft power
P_n^m	associated Legendre function of the first kind
\bar{P}_n^m	normalized associated Legendre function of the first kind
$P(\zeta)$	pressure distribution, N/m ²
$p(x, y, z, t)$	pressure in flow field, N/m ²
\tilde{p}	perturbation pressure, N/m ²
p_0	atmospheric pressure, N/m ²
ΔP	rotor disk pressure
Q	power or number of blades
Q_n^m	associated Legendre function of the second kind
\bar{Q}_n^m	normalized associated Legendre function of the second kind

\bar{r}	non-dimensional radial position
R	rotor radius
t	time
\bar{t}	$= \Omega t$
T	thrust
u	horizontal component of induced velocity
$u(t)$	unit step function
U	inplane flow
v	vertical component of induced velocity
\vec{v}	velocity vector
v_z	z-component of velocity, m/sec
v_ξ	ξ -component of velocity, m/sec
\bar{v}	steady velocity component, m/sec
V	flow normal to the disk
V_∞	free-stream velocity
V_T	total velocity, m/sec
w	induced flow
W	inflow
x	distance on the blade from the center of the rotor
X	$= \tan \chi / 2 $
x, y, z	cartesian components
Z_{max}	outer bound of wake
α_n^m, β_n^m	induced flow expansion coefficients

γ	prime velocity blend, m/sec
$\hat{\gamma}$	derived velocity blend, m/sec
Γ_{jn}^m	matrix elements
δ_{mn}	dirac delta function
$\Delta \dot{m}$	mass per unit area, kg/(m ² sec ²)
Δp	pressure drop, N/ m ²
ζ_n^m, σ_n^m	derived potential factors
η	climb rate = $v/\Omega R$
$\bar{\eta}$	ellipsoidal coordinate system component
θ	pitch angle
κ	swirl parameter = 2.2
λ	inflow ratio = $\frac{V_\infty + \bar{V}}{\Omega R}$; total inflow = $\eta + v$
Λ	Lagrange's multiplier
μ	advance ratio = $u/\Omega R$
ν	ellipsoidal coordinate or $\sqrt{1-r^2}$
\bar{V}	normalized inflow = $w/\Omega R$
ξ	streamwise variable
$\hat{\xi}$	unit vector in streamwise direction
ρ	density of air, kg/m ³
τ_n^{mc}, τ_n^{ms}	pressure coefficients for Fourier series expansion
φ	angle between the lift and the thrust

ϕ_n^m	radial expansion shape function
Φ	pressure
Φ_n^{mc}, Φ_n^{ms}	pressure potentials
χ	skew angle
ψ	angular position from rotor aft
$\bar{\psi}$	ellipsoidal coordinate
Ψ	prime velocity potentials
$\hat{\Psi}$	derived velocity potentials
ω	reduced frequency $\omega = \Omega R/V$
Ω	frequency of oscillating pressure or mass source, rad/sec
Ω	angular velocity
$(\)_o$	terms with $m+n$ odd
$(\)_e$	terms with $m+n$ even
$(\)^\bullet$	d/dt
$(\)_{lower}$	on lower surface of disk
$(\)_{upper}$	on upper surface of disk
$0^+, 0^-$	$0 + \varepsilon, 0 - \varepsilon$
$\vec{\nabla}$	$\frac{\partial}{\partial x} \hat{i} + \frac{\partial}{\partial y} \hat{j} + \frac{\partial}{\partial \tilde{x}} \hat{k}$
$ a ^2$	Euclidean norm, $\sum a_n^2$

Chapter 1

Introduction

The rotor of a helicopter can be modeled in different ways. For actuator-disk theories, there is a lift or thrust vector perpendicular to the plane of the rotor, pointing in the direction of lift. In more advanced theories, the lift is taken perpendicular to the vortex sheet that trails each blade. Simple physics state that the reaction to this thrust is an induced velocity in the opposite direction. The induced velocity has a kinetic energy that must be provided by the rotor. This energy produces the induced power loss of a rotor. The study of induced power on a helicopter rotor has been developed from a variety of perspectives along the years. Induced power can never be eliminated, but it can be minimized. An optimum propeller has minimum induced power.

The study of induced power on a helicopter can be divided in two main flight regimes: axial flow and skewed flow. The first regime corresponds to the case for which the flow coming into the rotor is perpendicular to the rotor plane. A sketch of the flow and rotor can be seen in Figure 1.2. For axial flow the skew angle, χ , is zero. This happens when the helicopter is in hover or ascending vertically through the air. When the helicopter flies

forward the flow coming into the rotor is no longer perpendicular; and thus the skew angle is non-zero and a skewed flow analysis is required.

For minimum induced power purposes, hover and forward flight are the both important cases to consider. If the induced power can be reduced in hover the helicopter would need less power in order to lift from the ground, resulting in additional power that could be used to lift more payload or increase the range of the helicopter. Reducing the induced power in forward flight contributes considerably to an increase in cruise speed and a further increase in range.

For both axial and skewed flows, we can model the rotor in one of two ways: as an actuator disk, or including a tilt on the lift. An actuator disk is a way to model the rotor as a circular region of zero thickness that can withstand changes in pressure across it. The main assumption with an actuator disk is that the lift vector is perpendicular to the disk. A real rotor has some tilt on the lift vector, so the rotor can also be modeled to account for this condition. If the lift is tilted, the wake velocity must be divided into two components (normal and tangential to the disk) because the tilt creates a swirl velocity. Some changes to existing theories need to be made to account for the tilt.

Finally, the number of blades considered in the study will contribute to changes in the behavior. Theories must be developed for an infinite number of blades (rotor as a disk) and for a finite number of blades (more realistic). It is of importance to include varying numbers

of blades to be able to show and understand how varying the number of blades affects the induced power.

Table 1.1 shows the division of the main cases that will be studied. Basically we have axial or skewed flow, depending on if the rotor is flying through air vertically or on forward flight motion. The rotor in each case can be modeled either as an actuator disk with perpendicular lift vector or a tilt on the vector can be included. Lastly, we can consider a finite or an infinite number of blades.

Previous theories predict the optimum inflow for each of the cases in axial flow. These theories will serve as references to determine the accuracy of the present model and better understand the changes in induced power for the different cases described previously. Once the model is verified, results can be developed for skewed flow (or forward flight) for different configurations with the security that the approach can be applied for such conditions.

Table 1.1: Cases studied using finite state methods

FLOW	ACTUATOR DISK		TILTED LIFT	
	Infinite Q	Finite Q	Infinite Q	Finite Q
AXIAL	Momentum Theory	Prandtl Solution	Betz Distribution	Goldstein Distribution
SKEWED	Momentum Theory	Finite-state	Finite-state	Finite-state (theory only)

Several alternative approaches can be used to model the downwash in the plane of a rotor. Techniques such as CFD and free-wake models can be applied successfully for

different applications but do not provide best results for real-time simulations due to the complexity of the computations. On the other hand, finite-state models provide good results for preliminary design and can be used in real-time simulations. Over the past 25 years, finite-state inflow equations have been developed to describe the flow. The inflow is expanded in terms of shape functions, resulting in a matrix set of ordinary differential equations that describe the flow. (See Refs. [1]-[9]). The development of these models has now culminated with the most general form of the equations, with previous versions being special cases of the general one.

Although the rotor blade may be moving at transonic speeds near the tip, the rotor wake is generally determined by incompressible potential flow theory. The solution of the incompressible potential flow equations (and of their derivative, the vorticity transport equations) has generally been deemed sufficient to define the wake geometry and induced flow of rotors. Thus, most models are based on these equations, including finite-state models. However, previous finite-state applications do not compute the flow below the plane of the rotor disk.

One purpose of this dissertation is to outline the features of a general set of inflow equations, including their derivation and special cases that will give all three components of velocity everywhere in the flow field including within the wake. Thus, this dissertation can form the basis for any version of the model for anyone interested in using it. The present dissertation also provides insights into the limitations and accuracy both of the most general

case and of the special cases. The general model will then be reduced to some of the special cases and applied to obtain the induced power for an optimum propeller.

1.1 Previous Work

Many attempts have been made with the purpose of modeling and understanding the behavior of a helicopter induced flow in order to reduce the negative impact on the performance of the rotor. Previous research approaches vary in complexity, but basically differ from each other depending on the characteristics of the induced flow distribution assumed for the creation of the theories. Previously developed research will be reviewed chronologically, dividing it in what is known as classical work and more recent developments.

1.1.1 Classical Work on Optimally Efficient Propellers

In 1929, Glauert [15] defined the minimum induced power required for an actuator disk to create thrust by simple work-energy principles. This simple Glauert momentum theory can be used to compute the minimum possible induced power for a given flight condition. In addition, he included the geometry of the flow in the blade coordinate that can be used to obtain a relationship between induced power and induced velocity.

Originally, momentum theory [16], [17] was developed to describe a mathematical model of an ideal propeller or helicopter rotor. It utilizes the basic fluid mechanics conservation laws to predict the behavior of the flowfield of a rotor, modeled as an infinitely thin disk. The simplest version of the rotor as a disk assumes a constant velocity. Therefore, the induced velocity field is considered to be uniform. The theory provides a relationship between power, the radius of the rotor and the induced velocity. This theoretical model can be applied for optimum induced power considerations for the case of axial flow for an actuator disk with an infinite number of blades. The results provide only an approximation, and do not produce results that can be used to design the rotor blades, since the use of a disk considers no loss of thrust at the blade tips, and the vortices and losses of each blade are therefore not accounted for. Due to the limitations of the uniform momentum theory, a different approach to the same problem was proposed and is known as blade-element, momentum theory.

Blade-element theory [16], [17] assumes that each element of the rotor is independent of the other elements in terms of lift and induced flow. The total thrust and the torque of the rotor are obtained by integration of loads along the span. Because the blade tip does not depend on its location, a correction factor must be introduced. Betz and Prandtl [18] used combined momentum and blade-element theory to obtain an approximation to include the effect of tip losses. Tip losses are thrust losses due to the fact that the edge of vortex sheet has special edge effects. Prandtl included a correction to account for a finite number of blades, thus enabling the development of results for an actuator disk in axial flow and a finite number of blades.

The optimum induced flow distribution for an actuator disk with an infinite number of blades is uniform flow. However, when the lift vector is taken as perpendicular to the vortex sheets (rather than perpendicular to the disk), the ideal power is no longer obtained by uniform flow. Betz determined that the minimum power is obtained when the induced flow at the individual blades is such that the vortex sheets remain along helical paths. For an infinite number of blades, it follows that the pressure field must follow this same shape.

The effect of a finite number of blades incurs an additional loss in wake energy due to the individual vortex sheets from each blade. In 1929, Goldstein [19] worked out the exact effect for optimized rotors. Prandtl developed a correction factor that agrees very well with Goldstein's exact solution for moderate climb rates.

1.1.2 Classical Work on Inflow Theories

In 1981, Pitt and Peters [1] developed a set of differential equations to obtain the dynamic inflow derivatives for a helicopter rotor with an unsteady loading and induced flow distribution. The theory relates rotor loads and the transient response of the rotor induced flow field. The dynamic inflow theory was developed to obtain induced inflow solutions that are more realistic than those of momentum theory and which provide an expression of the induced velocity distribution for a helicopter rotor. The Pitt-Peters model uses three terms to describe the inflow distribution. The model is in use in a wide variety of companies and institutions that use it for stability and handling quality applications. There are however

some limitations to the theory, as it gives only a very low-order approximation to the induced flow field of a helicopter rotor.

He and Peters [4], [5], [6] further developed the theory to obtain a generalized dynamic wake model that included higher-order terms. The unsteady induced-flow theory can be applied in stability, vibration, control and aeroelastic studies. The theory is based on an acceleration potential for an actuator disk. The Pitt-Peters model included only the zeroeth and first harmonics with one radial shape function for each harmonic. The He theory expands this to include a higher number of harmonics and of radial shape functions for each harmonic. The pressure and the induced flow are expressed in a polynomial distribution (proportional to Legendre functions) radially and in terms of a Fourier series azimuthally. By the use of higher harmonics, the flow can be studied in detail for other applications instead of being limited to obtaining the average flow in only for thrust, pitch moment and roll moment, which was the case with the Pitt-Peters model. However, there are some limitations to the use of the generalized dynamic wake model proposed by He and Peters. One of the limitations is that the model does not account for tilt on the lift vector. It is an actuator disk theory. Also, the flow in the He model is not defined in all three directions or everywhere in the rotor flow field, therefore more work needed to be done to be able to analyze situations where the flow has to be defined everywhere and the use of all components is needed.

Morillo and Peters [7] redefined a new dynamic inflow model to overcome the limitations of the Peters-He model. The equations that define the flow are re-derived from first

principles to compute the whole flow field with all of the components for the volume above the rotor disk. The model uses continuity and momentum equations (partial differential equations) in three dimensions around the actuator disk to model the flow. The conservation equations are then transformed to a set of ordinary differential equations in state-space form by the application of Galerkin method. The set of ordinary differential equations gives a relation between the velocity coefficients and the pressure coefficients (similar to the one for the Peters-He model) but includes an expansion in the influence coefficient and damping matrices that allowed for the three components of velocity (axial, radial and azimuthal) to be determined everywhere on the upper hemisphere of the disk. Because of the fact that the method has the same matrix structure than the one for the Pitt-Peters and Peters-He models, the addition of the improved features would be easily applied to codes that already utilize these previous versions of the dynamic wake model. However, this theory is not able to define the velocity field below the plane of the rotor disk. See Figure 3.2.

Makinen and Peters [10], [11] expanded the Peters-He as well as the Morillo-Peters model to account for lift tilt by the introduction of a swirl correction. Different swirl corrections were analyzed and used to perform comparisons with the results provided by Goldstein. Makinen was able to obtain accurate results for a finite number of blades by the addition of the extra kinetic energy. The comparison of the velocity field and the circulation around the propeller blades was good over most of the blade span. He's model provides the necessary fidelity to be able to obtain the induced power for a helicopter rotor modeled as an actuator

disk, and the addition provided by Makinen allows to extend the theory for the tilted lift case of a rotor with a finite number of blades.

Different inflow theories have been developed, Rosen [24] proposed an approximate actuator disk model of a rotor in hover or axial flow based on potential flow equations. The model is derived from the same fundamental equations as the ones used in the Refs. [1] and [4] model, and in fact his theory shows the solution for the Pitt-Peters model as a special case. The assumptions made enable the model to include wake distortion effects in addition to the original dynamic-inflow model, but as the models shown in references [1] through [8], the solution is only applicable to actuator disk cases.

1.1.3 Motivation of Optimization Work

Harris [20] examined a large set of data for rotor power coefficient versus advance ratio. Figure 1.1 shows the thrust for a helicopter in forward flight. If the profile and parasite power are subtracted from the total helicopter power (the two higher-ordinate curves), one is left with the net induced power of a helicopter. These results show that, for moderate advance ratios, the difference between the measured rotor induced power and the theoretical prediction for minimum induced power proposed by Glauert are considerably large. This discrepancy implies that lifting rotors in forward flight have efficiencies far lower than the optimum efficiencies predicted by theory.

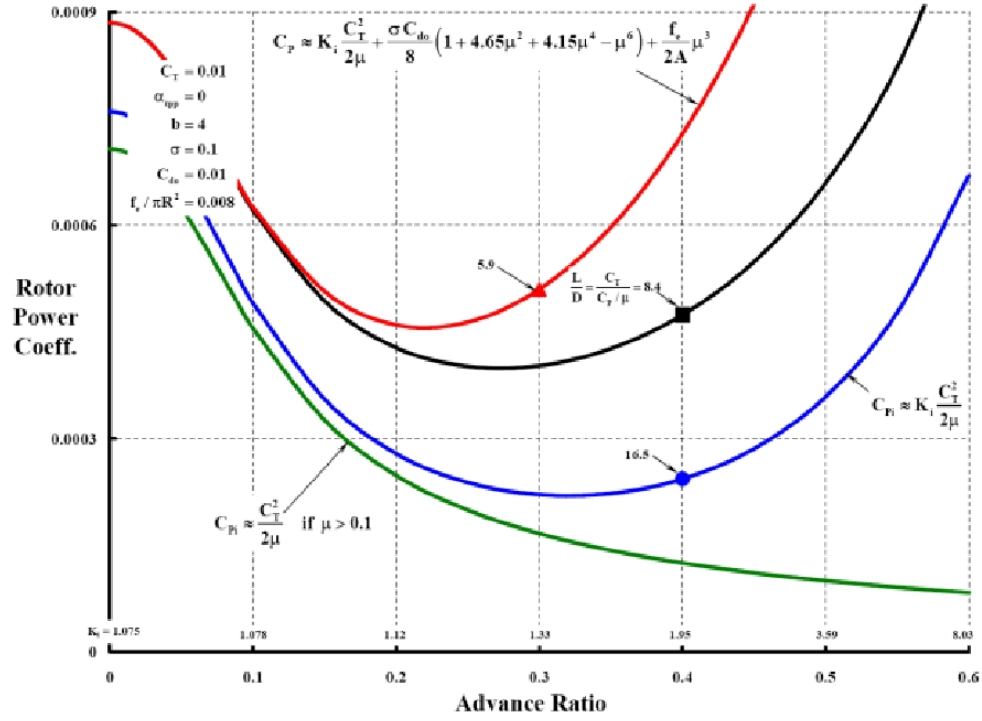


Figure 1.1: Harris' power coefficient with advance ratio plot for a helicopter.

Following Harris' results, Ormiston [21], [22] performed extensive runs with RCAS (Rotorcraft Comprehensive Analysis System) to try to determine why the actual results were differing from the ideal results. In these studies, the profile drag of the airfoil was assumed to be zero so that the induced power could be separated out. The results of those studies similarly showed a large difference between ideal induced power and the actual induced power of rotorcraft, the actual being several times larger than ideal.

In the hopes of expanding on the understanding of optimum rotors, other research efforts have used other methods to determine why there is a considerable difference between the theoretical predicted minimum induced power and the real results obtained from different sources. The use of computer codes such as EHPIC/HERO (Evaluation

Helicopter Performance using Influence Coefficients/ Helicopter Rotor Optimization), which provides optimization techniques for the design of rotor blades, or the software CHARM (Comprehensive Hierarchical Aeromechanics Rotorcraft Model) [23] —that models aerodynamics and dynamic of rotorcraft in general flight conditions— have been applied to obtain induced power for a variety of flight conditions. All results show the same apparent shortfall.

1.2 Optimization Problem Statement

Work-Energy principles indicate that the induced power P_i generated for a lifting rotor (i.e., the power that does not perform useful work) can be found by computing the shaft power and then subtracting the work done on the vehicle

$$P_i = P_s - TV - HU \quad (2.1)$$

where T is the thrust perpendicular to the disk, V is the rotor velocity in the T direction, H is the rotor force in the inplane direction, and U is the rotor velocity in the H direction (See Figure 1.2). By necessity, the magnitude of this power must equal the power that is expended into the kinetic energy of the induced flow. It follows that simple, Glauert momentum theory can be used to compute the minimum possible induced power for a given flight condition.

Several potential sources of decreased efficiency can be identified in terms of the physics of an actual rotor as compared to an ideal actuator disk. First, an ideal disk produces thrust perpendicular to the disk whereas a true rotor produces a tilted thrust vector that results in swirl velocity. Therefore, there is lost energy. Second, an ideal rotor has an infinite number of blades whereas a true rotor has a finite number. The fact that there are vortex sheets coming off the individual blades implies an upwash outside of the slipstream that further translates into lost energy. Third, an ideal disk can generate an arbitrary lift distribution over the span and azimuth. An actual blade, on the other hand, can only produce lift under the constraints of both allowable blade pitch changes and of the limits on airfoil lift coefficients at high angles of attack. One goal of the present research effort is to determine which of these contribute to the drastic increase in induced power and, consequently, what changes in rotor hardware (if any) might address the issue.

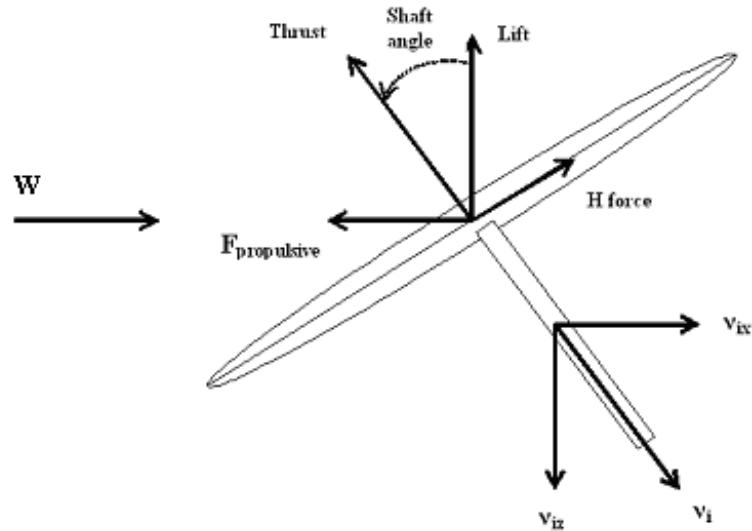


Figure 1.2: Basic illustrative problem for a rotor [22].

1.3 Present Approach

Finite-state inflow models have been suggested as a theoretical basis whereby to study the reasons for this efficiency deficit. In this dissertation, a finite-state inflow model is utilized to formulate the optimum circulation and inflow distribution for rotors in axial flow. The results show that a formal optimization with finite-state models can be done in closed form and that such an optimization recovers the classical uniform-flow condition (for an actuator disk with an infinite number of blades), the Prandtl solution (for an actuator disk with a finite number of blades), the Betz distribution (for a lifting rotor with an infinite number of blades) and the Goldstein solution (for a lifting rotor with a finite number of blades). Thus, it should be possible to use finite-state models to investigate optimum rotor performance in forward flight.

In classical momentum theory, the optimum performance of an actuator disk is well known to be a uniform pressure distribution with a resulting uniform inflow. However, propellers and rotors are not actuator disks. In particular, the lift vector for rotors is perpendicular to the vortex sheets, not to the disk. As a consequence, the optimum distribution for pressure and inflow for a true rotor is the Betz distribution rather than uniform. Furthermore, real rotors have a finite number of blades which further modifies the optimum distribution to be that of Prandtl for an actuator disk and that of Goldstein for a rotor with a finite number of blades.

Interestingly, finite-state inflow models offer a natural framework in which to study optimum inflow distributions because – in these models – both inflow and thrust are expanded in a series of orthogonal functions that make the optimization problem a closed-form, classic case of minimizing a quadratic cost function with linear constraint. In addition, recent improvements to dynamic wake models allow for both the tilt of the thrust vector and the resultant swirl velocity. This allows finite-state methodologies to be rigorous in the context of optimization of induced power.

In this dissertation, we show how a closed-form optimization of induced power with finite-state models reproduces the momentum result for an actuator disk, the Prandtl result for a disk with a finite number of blades, the Betz result for an ideal rotor, and the Goldstein result for a rotor with finite number of blades. This success gives reason to believe that the methodology can be used in the future for applications to optimization in forward flight.

One goal of this research is to derive the theoretical background to obtain results for an optimum propeller. The model will provide the necessary solutions to be used in real applications by the addition of the resulting expressions to the general code already in use for many applications. Results are shown to validate the theory and show the induced power for the cases where theory was never previously developed. The optimization provides a general solution of the pressure coefficients for a general rotor blade configuration. However, it can be applied for specific cases (specific blades or configurations) with changes to the constraints and parameters of the optimization.

Chapter 2

Complete Inflow Theory Formulation

Finite-state inflow theories have been used in order to define the wake geometry and the induced flow of rotors. The Pitt-Peters model and the higher order Peters-He model represent the downwash in the plane of the rotor being expanded in terms of a set of radial and azimuthal functions that describe the flow. The inflow is therefore described by a finite set of state equations that are driven by the loading on the rotor blades.

Up to this point, previous developments have been able to achieve the full description of the wake in all ranges of flight regime – for all skew angles including axial and edgewise conditions –, for all three components of the flow – axial, radial and azimuthal –, and in all regions around an actuator disk except for the lower hemisphere. Figure 2.1 shows the different areas around the actuator disk, where regions B and C lay on the lower hemisphere. The purpose of this chapter is to provide a set of ordinary differential equations in matrix form that describe the flow for all ranges, including all three components, and for all regions. This formulation will give the most general form of the equations, with previous versions being special cases of the general one. It is thus, a complete, nonlinear induced flow theory for rotors in incompressible flow.

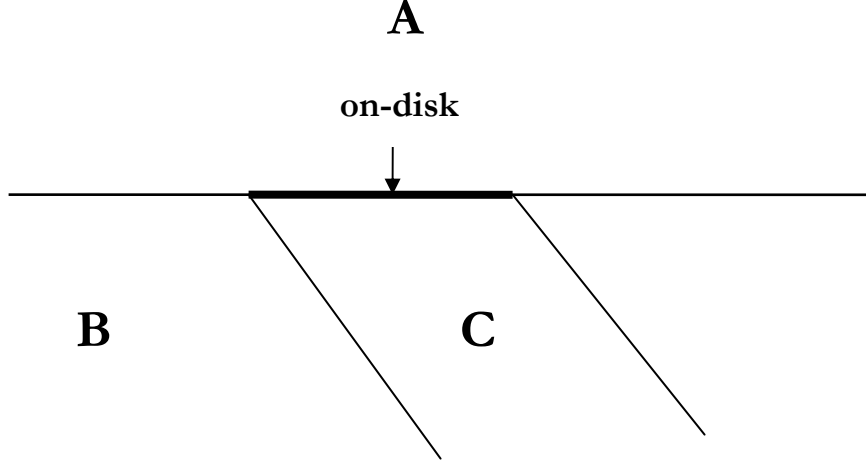


Figure 2.1: Regions on, off and around an Actuator Disk

2.1 Potential Flow Equations

Conservation of mass and momentum (partial differential equations) in three dimensions around an actuator disk can be reduced to the nonlinear, potential flow equations for incompressible flow, Ref. [25].

$$\vec{\nabla} \cdot \vec{V} = 0 \quad (2.1)$$

$$\frac{\partial \vec{V}}{\partial t} + (\vec{V} \cdot \vec{\nabla}) \vec{V} = -\frac{\vec{\nabla} p}{\rho} \quad (2.2)$$

In past studies, these have been treated in various nondimensional schemes. Here, for clarity, we keep everything dimensional.

In the following derivation, we will first linearize about a steady free-stream velocity. Later, we will come back and consider how some limited nonlinearities can be introduced into the equations. The coordinate system in Figure 2.2 shows the rotor disk with x in the nominally forward direction, y into the paper (the advancing side of the rotor), and z positive down.

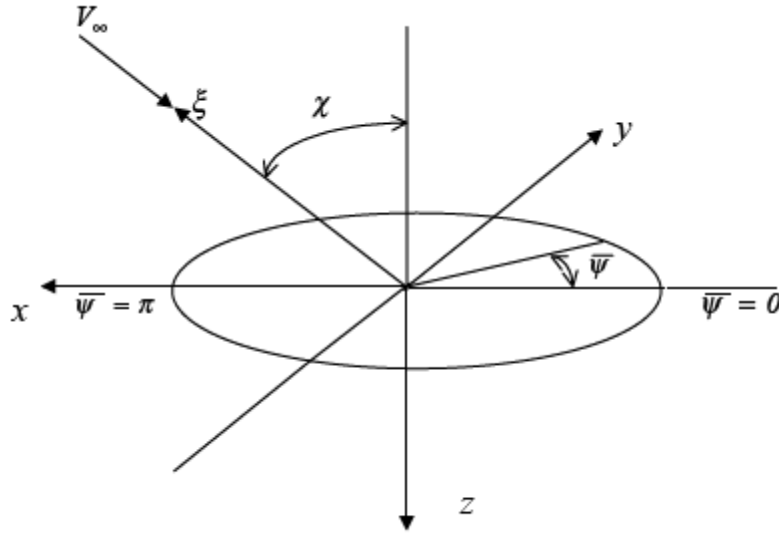


Figure 2.2: Coordinate system

The steady free-stream is considered to be of magnitude V_∞ and directed opposite to a unit vector ξ that is skewed with respect to the negative- z axis by an angle χ , positive towards the x axis. Thus, we have for the free-stream velocity,

$$\vec{V} = -V_\infty \xi + \vec{v} \quad (2.3)$$

$$\hat{\xi} = \sin(\chi)\hat{i} - \cos(\chi)\hat{j} \quad (2.4)$$

where $\hat{i}, \hat{j}, \hat{k}$ are unit vectors in the x, y , and z directions, respectively. When these definitions are put into the momentum equations and linearized, the resultant equations become:

$$\vec{\nabla} \cdot \vec{v} = 0 \quad (2.5)$$

$$\frac{\partial \vec{v}}{\partial t} - V_\infty \frac{\partial \vec{v}}{\partial \xi} = -\frac{\vec{\nabla} p}{\rho} \quad (2.6)$$

The boundary condition is that all components of v must be zero far upstream.

2.2 Pressure Potentials

The next step in the derivation is to expand the pressure of the linearized equations in terms of potential functions. Discontinuities in pressure (or in its derivatives) can only occur on the disk. Therefore, we utilize the solution to Laplace's equations in ellipsoidal coordinates, defined on Appendix B, to represent the pressures in the flow field. This then allows the introduction of time-varying pressure drops or mass sources at arbitrary locations on the rotor disk. The solutions that we include are those that die out at infinity. They are;

$$\Phi_n^{mc}(v, \eta, \psi) = \bar{P}_n^m(v) \bar{Q}_n^m(i\eta) \cos m\psi \quad (2.7)$$

$$\Phi_n^{ms}(v, \eta, \psi) = \bar{P}_n^m(v) \bar{Q}_n^m(i\eta) \sin m\psi \quad (2.8)$$

where v, η , and ψ are the ellipsoidal coordinates defined in Appendix A and m takes the values $\{0, 1, 2, 3, 4, \dots\}$ and n takes on the values $\{m, m+1, m+2, m+3, \dots\}$.

It is interesting to see how these potential functions behave across the $z=0$ plane (where v jumps from positive to negative). In the plane of the rotor disk but off of the rotor disk, we have $v=0$. Therefore, the functions with $m+n$ odd (which are odd functions in v) are zero on that plane; and the functions with $m+n$ even (which are even functions in v) have a zero normal derivative on that plane. On the upper surface of the disk, we have $0 < v < 1$; and, on the lower surface, we have $-1 < v < 0$. Thus, v jumps across the disk. Therefore, the $m+n$ odd potentials have a jump across the disk (simulating a pressure jump); and $m+n$ even functions have a jump in normal derivative (simulating a mass source).

The pressure may now be expanded in terms of these potentials.

$$\frac{P}{\rho} = - \sum_{m=0}^{\infty} \sum_{n=m}^{\infty} \left(\tau_n^{mc} \Phi_n^{mc} + \tau_n^{ms} \Phi_n^{ms} \right) \quad (2.9)$$

where the Φ 's are nondimensional so that τ will have the units of m^2/sec^2 . Note that, for $m+n$ odd, the pressure will be discontinuous across the disk since $P_n^m(v)$ is odd in that case. Similarly, for $m+n$ even, the normal gradient of pressure will have a discontinuity across the disk. Thus, $m+n$ odd corresponds to lift on the disk, and $m+n$ even corresponds to a mass source on the disk. It follows that the following relationships connect the τ 's to either the pressure drop or the injected mass on the plane of the disk:

$$\Delta P = P_{\text{lower}} - P_{\text{upper}} = 2\rho \sum_{m=0}^{\infty} \sum_{n=m+1, m+3, \dots}^{\infty} \left(\tau_n^{mc} \Phi_n^{mc} + \tau_n^{ms} \Phi_n^{ms} \right)_{\eta=0} \quad (2.10)$$

$$\Delta \dot{m} = \rho \Delta v = \frac{(P_{\text{lower}} + P_{\text{upper}})}{V_{\infty}} = -2 \left(\frac{\rho}{V_{\infty}} \right) \sum_{m=0}^{\infty} \sum_{n=m+2, m+4, \dots}^{\infty} \left(\tau_n^{mc} \Phi_n^{mc} + \tau_n^{ms} \Phi_n^{ms} \right)_{\eta=0} \quad (2.11)$$

where ΔP is the net pressure in the upward direction across the disk (negative z), and $\Delta \dot{m}$ is the net mass per unit area being injected into the flow field per unit time at the disk

(implying a positive z velocity below the disk and negative z velocity above the disk. Note that only $m+n$ odd will contribute to ΔP , and only $m+n$ even will contribute to $\Delta \dot{m}$. Since the potential functions are a complete set of orthogonal functions on the disk for either $m+n$ odd or $m+n$ even, knowledge of the pressure drop and mass injection at the disk at any point in time completely determines the τ 's at that instant in time.

2.3 Velocity Potentials

The first velocity potentials that we define will be called the prime potentials, Ψ . These are defined as the integrals along a streamline of the pressure potentials,

$$\Psi_n^m = \int_{\xi}^{\infty} \frac{\Phi_n^m}{R} d\xi \quad (2.12)$$

where the rotor radius R is added to keep the velocity potentials nondimensional. The above relationship holds both for the cosine terms (m_c) and for the sine terms (m_s). The flow velocities are then represented by an expansion summation in the gradient of these velocity potentials.

$$\vec{v} = R \sum_{m=0}^{\infty} \sum_{n=m}^{\infty} \left(a_n^m \vec{\nabla} \Psi_n^{m_c} + b_n^m \vec{\nabla} \Psi_n^{m_s} \right) \quad (2.13)$$

Note that, since the Ψ are nondimensional, since the R is added for scaling; and, since the Laplacean operator has units of one over length, the a_n^m and b_n^m will have units of velocity, m/sec.

It is straightforward to show that these expansion gradients, $\nabla\Psi$, are exactly the velocity due to each individual pressure potential Φ in the static case.

$$V_\infty \frac{\partial \bar{v}}{\partial \xi} = \frac{\vec{\nabla} P}{\rho} \quad (2.14)$$

Substitute Equation (2.9) and (2.13) into Equation (2.6). This leads to:

$$V_\infty \sum_{m=0}^{\infty} \sum_{n=m}^{\infty} \left(a_n^m \vec{\nabla} \Phi_n^{mc} + b_n^m \vec{\nabla} \Phi_n^{ms} \right) = \int_{\xi}^{\infty} \vec{\nabla} \sum_{m=0}^{\infty} \sum_{n=m+1, m+3, \dots}^{\infty} \left(\tau_n^{mc} \Phi_n^{mc} + \tau_n^{ms} \Phi_n^{ms} \right) d\xi \quad (2.15)$$

Then, based in the definition in Equation (2.12),

$$a_n^m = \frac{\tau_n^{mc}}{V_\infty}; \quad b_n^m = \frac{\tau_n^{ms}}{V_\infty} \quad (2.16)$$

Thus, this particular choice of velocity potential will give exact results at zero frequency even for truncated matrices.

The above definition of velocity potentials involves three areas of the flow field that will be important to identify. First, there is the area above the plane of the rotor disk ($\xi > 0, z < 0, 0 < \nu < f$). This is the upper hemisphere where one need only be concerned with positive values of ν . A second area is the flow within the wake (i.e., the flow below the plane of the rotor disk along streamlines that pass through the rotor disk, region C in Figure 2.1). This area defines a skewed cylinder that encompasses the rotor wake. When one follows such a streamline into the wake, ν is discontinuous across the rotor disk resulting in discontinuities either in the potential functions or in their derivatives. This invalidates the assumptions of Equations (2.12-2.13) since the Laplacean operator cannot be brought out from under the integral sign. Strictly speaking, the flow is not potential flow within the wake, giving issues

in finding the induced flow there. The third area of the flow to be defined is the flow below the plane of the rotor—but along streamlines that do not intersect the rotor disk. The velocity potentials are valid in that area, which is a region governed by potential flow (i.e., region B in Figure 2.1).

Unfortunately, there is presently no known, closed-form expression for these velocity potentials in Equation (2.12) at arbitrary wake skew angles. Thus, in the above formulation, some preprocessing must be done to compute the gradients of Ψ at points in the flow field for which the velocity is desired. In order to overcome this limitation, another set of velocity potentials is defined, the derived potentials, $\hat{\psi}$. They reduce to the prime potentials Ψ for the special case in which $\chi=0$. In order to find these functions, one must find potential functions such that

$$R \frac{d\hat{\Psi}_n^m}{dz} = -R \frac{d\hat{\Psi}_n^m}{d\xi} = \Phi_n^m \quad (2.17)$$

Reference [6] was able to find these functions in the following form:

$$\hat{\Psi}_n^m = \sigma_n^m \Phi_{n+1}^m + \varsigma_n^m \Phi_{n-1}^m \quad (2.18)$$

where

$$\begin{aligned} \sigma_n^m &= \frac{1}{K_n^m \sqrt{(2n+1)(2n+3)[(n+1)^2 - m^2]}} \\ \varsigma_n^m &= \frac{1}{K_n^m \sqrt{(4n^2-1)(n^2 - m^2)}} \quad n \neq m \end{aligned} \quad (2.19)$$

and

$$K_n^m = \left(\frac{\pi}{2}\right)^{(-1)^{n+m}} H_n^m \quad (2.20)$$

$$H_n^m = \frac{(n+m+1)!!(n-m-1)!!}{(n+m)!!(n-m)!!}$$

which are valid for the upper-half plane ($z < 0$) with the exception of the case $m=n$. For that case, ζ is infinite and $Q(i\eta)$ and $P(\nu)$ are undefined for the subscript less than the superscript ($n < m$).

Reference [9] completed the formulation for these special cases so that now all of these derived potential functions are known for all superscripts and subscripts. For the case $m=n$ but not equal to zero, the derived potentials become:

$$\hat{\Psi}_n^{mc} = \left[\sigma_n^m \bar{P}_{m+1}^m(\nu) \bar{Q}_{m+1}^m(i\eta) + \varsigma_n^m \bar{P}_{m-1}^m(\nu) \bar{Q}_{m-1}^m(i\eta) \right] \cos m\psi \quad (2.21)$$

$$\hat{\Psi}_n^{ms} = \left[\sigma_n^m \bar{P}_{m+1}^m(\nu) \bar{Q}_{m+1}^m(i\eta) + \varsigma_n^m \bar{P}_{m-1}^m(\nu) \bar{Q}_{m-1}^m(i\eta) \right] \sin m\psi \quad (2.22)$$

where \bar{P}_{m-1}^m and \bar{Q}_{m-1}^m are defined as

$$\bar{P}_{m-1}^m(\nu) = \frac{2}{\pi} \frac{\sqrt{(2m)!!}}{\sqrt{(2m+1)!!}} \frac{(1-\nu^2)^{m/2}}{(1+\nu)^m} \sum_{n=0}^{m-1} \frac{(m-1)! 2^{m-1-n} (-1)^n}{n!(m-1-n)!(n+m)} (1-\nu)^n \quad (2.23)$$

$$\bar{Q}_{m-1}^m(i\eta) = \frac{1}{(1+\eta^2)^{m/2}} \quad (2.24)$$

For the special case $m=n=0$, the velocity potential is:

$$\hat{\Psi}_0^0 = \frac{2}{\pi} \nu \left[1 - \eta \tan^{-1} \left(\frac{1}{\eta} \right) \right] - \frac{2}{\pi} \ln|1+\nu| - \frac{1}{\pi} \ln|1+\eta^2| + \frac{2}{\pi} \ln|Z_{\max}| \quad \nu > 0 \quad (2.25)$$

where Z_{max} is a large number representing the radius to which the ξ integral is taken. In reality, the integral is infinite when taken to infinity. However, it is only the gradients of the potential functions that are required—not the potential functions themselves—and one can always add a constant to a potential function. Therefore, the above definition is tractable for practical solutions. For the derived velocity potentials below the plane, one can consider that the velocity potentials with $m+n$ odd must be symmetric with respect to $z=0$; while functions with $m+n$ even must be asymmetric to that plane, Equation (2.18). That defines the potentials in the lower hemisphere outside of the wake, region B. As with the prime potentials, potentials within the wake will require special attention and will be considered later in this chapter.

Since the velocity potentials all satisfy Laplace's equation, it follows that the velocities, themselves, will satisfy continuity, Equation (2.1). This leaves only the momentum equation as the governing equation for the velocity expansion coefficients. Therefore, the problem of obtaining a finite-state wake model is reduced to the problem of representing the momentum equations in finite-state form.

2.4 Galerkin Approach

The next step in the derivation is to use the Galerkin approach (described on Appendix C) to transform the momentum equation into a set of ordinary differential equations for the expansion coefficients. To this end, the pressure expansions, Equation (2.9), and the prime

velocity potential expansions, Equation (2.13) are substituted into Equation (2.6). The test functions are taken to be the gradient of the pressure potentials. These test functions are dotted with the momentum equation and integrated over the upper hemisphere (above the plane of the rotor disk) to obtain equations of motion. (This avoids the problems mentioned earlier about discontinuities across the rotor disk and in the wake.) It should also be noted that, since the upper hemisphere is chosen, there are no velocity boundary conditions across vortex sheets, due to the fact that discontinuities only occur in the wake, which is below the plane of the disk. Thus, either the prime potentials or the derived potentials are appropriate for a Galerkin approach. As a result of integrating over the upper hemisphere, however, the velocity solution will only be valid in the upper hemisphere. Later, the velocity field below the rotor plane will be discussed.

After the proper expansions are substituted into the momentum equation, the divergence theorem can be used to transform the Galerkin equations into a set of ordinary differential equations for the components of the velocity potential. The cosine and sine functions completely separate into two uncoupled sets. For the cosine elements, the Galerkin procedure gives:

$$R \begin{bmatrix} [\tilde{L}^c]_{o,o} & [\tilde{L}^c]_{o,e} \\ [\tilde{L}^c]_{e,o} & [\tilde{L}^c]_{e,e} \end{bmatrix} \begin{Bmatrix} \left\{ \begin{matrix} \bullet \\ a_n^m \end{matrix} \right\}_o \\ \left\{ \begin{matrix} \bullet \\ a_n^m \end{matrix} \right\}_e \end{Bmatrix} + V_\infty \begin{bmatrix} [D^c]_{o,o} & [D^c]_{o,e} \\ [D^c]_{e,o} & [D^c]_{e,e} \end{bmatrix} \begin{Bmatrix} \left\{ a_n^m \right\}_o \\ \left\{ a_n^m \right\}_e \end{Bmatrix} = \begin{bmatrix} [D^c]_{o,o} & [D^c]_{o,e} \\ [D^c]_{e,o} & [D^c]_{e,e} \end{bmatrix} \begin{Bmatrix} \left\{ \tau_n^m \right\}_o \\ \left\{ \tau_n^m \right\}_e \end{Bmatrix} \quad (2.26)$$

where the matrices are expressed in terms of integrals on the plane of the rotor.

$$[\tilde{L}^e] = \left[\iint_s \frac{\partial \Phi_j^r}{\partial \tilde{\alpha}} \left(\int_0^\infty \Phi_n^{mc} d\xi \right) ds \right] = \left[\iint_s \Phi_j^r \frac{\partial}{\partial \tilde{\alpha}} \left(\int_0^\infty \Phi_n^{mc} d\xi \right) ds \right] \quad (2.27)$$

$$[D^e] = \left[\iint_s \frac{\partial \Phi_j^r}{\partial \tilde{\alpha}} \Phi_n^{mc} ds \right] = \left[\iint_s \Phi_j^r \frac{\partial \Phi_n^{mc}}{\partial \tilde{\alpha}} ds \right] \quad (2.28)$$

A similar set can be written for the sine components. Note that the equations have been partitioned into subscripts “*o*” for terms with $m+n$ odd and “*e*” for terms with $m+n$ even. For cosine terms, $m=0,1,2,3 \dots$ and for sine terms, $m=1,2,3\dots$. In either case, $n=m, m+2, m+4$ or $m+1, m=3, m+5$ depending on whether the subscript of the partition is “*e*” or “*o*.”

The alternative forms in Equations (2.27-2.28) (along with identities for the Legendre functions) allow the matrices to be reduced to integrals on the rotor disk which can be expressed in closed form. Thus, the $[D]$ matrix can be expressed as below for either cosine or sine;

$$D_{jn}^m = \frac{1}{K_n^m} \delta_{jn} \delta_{nm} \quad (2.29)$$

$$j+r = \text{odd}; \quad n+m = \text{odd}$$

$$j+r = \text{even}; \quad n+m = \text{even}$$

$$D_{jn}^m = \frac{2\delta_{nm}}{\pi \sqrt{H_n^m H_j^m}} \frac{\sqrt{(2j+1)(2n+1)}}{(j+n+1)(j-n)} (-1)^{\frac{j+3n-1}{2}} \quad (2.30)$$

$$j+r = \text{odd}; \quad n+m = \text{even}$$

$$j+r = \text{even}; \quad n+m = \text{odd}$$

and the $[\tilde{L}]$ matrix can be expressed as:

$$\left[\tilde{L}_{jn}^{0m} \right]^c = X^m \Gamma_{jn}^{0m} \quad (2.31)$$

$$\left[\tilde{L}_{jn}^{rm} \right]^c = \left[X^{|m-r|} + (-1)^l X^{|m-r|} \right] \Gamma_{jn}^{rm} \quad (2.32)$$

$$\left[\tilde{L}_{jn}^{rm} \right]^s = \left[X^{|m-r|} - (-1)^l X^{|m-r|} \right] \Gamma_{jn}^{rm} \quad (2.33)$$

where

$$X = \tan(\chi/2), \quad l = \min(r, m) \quad (2.34)$$

$$\begin{aligned} \Gamma_{jn}^{rm} &= \frac{\text{sign}(r-m)}{\sqrt{K_n^m K_j^r} \sqrt{(2n+1)(2j+1)}} \delta_{j,n\pm 1} \\ r+m &= \text{odd}; j+r = \text{odd}; n+m = \text{odd} \\ r+m &= \text{odd}; j+r = \text{even}; n+m = \text{even} \end{aligned} \quad (2.35)$$

$$\begin{aligned} \Gamma_{jn}^{rm} &= \frac{(-1)^{\frac{n+j-2r}{2}} (2) \sqrt{(2n+1)(2j+1)}}{\sqrt{H_n^m H_j^r} (n+j)(n+j+2) \left[(n-j)^2 - 1 \right]} \\ r+m &= \text{even}; j+r = \text{odd}; n+m = \text{odd} \end{aligned} \quad (2.36)$$

$$\begin{aligned} \Gamma_{jn}^{rm} &= \frac{(-1)^{\frac{n+j-2r+2}{2}} (8) \sqrt{(2n+1)(2j+1)}}{\pi^2 \sqrt{H_n^m H_j^r} (n+j)(n+j+2) \left[(n-j)^2 - 1 \right]} \\ r+m &= \text{even}; j+r = \text{even}; n+m = \text{even} \end{aligned} \quad (2.37)$$

$$\begin{aligned} \Gamma_{jn}^{rm} &= \frac{(-1)^{\frac{3n+j+2m-2r}{2}} (4) \text{sign}(r-m) \sqrt{(2n+1)(2j+1)}}{\pi \sqrt{H_n^m H_j^r} (n+j)(n+j+2) \left[(n-j)^2 - 1 \right]} \\ r+m &= \text{odd}; j+r = \text{odd}; n+m = \text{even} \\ r+m &= \text{odd}; j+r = \text{even}; n+m = \text{odd} \end{aligned} \quad (2.38)$$

$$\begin{aligned} \Gamma_{jn}^{rm} &= \frac{1}{\sqrt{H_n^m H_j^r} \sqrt{(2n+1)(2j+1)}} \delta_{j,n\pm 1} \\ r+m &= \text{even}; j+r = \text{odd}; n+m = \text{even} \\ r+m &= \text{even}; j+r = \text{even}; n+m = \text{odd} \end{aligned} \quad (2.39)$$

It should be noted that, because of the logarithmic term in the $m=n=0$ element, the integral for Γ is formally infinite for the case $m = r = n = j = 0$. However, following the lead of Ref. [4], we express the infinity as a finite series that only approaches infinity as the number of terms in the expansion approaches infinity, but that is finite for the case of a truncated approximation. This allows a solution with a finite number of terms that provides formal convergence to the exact answer,

$$\Gamma_{00}^{00} = \left(\frac{4}{\pi^2} \sum_{n=1}^N \frac{1}{n} \right) + \frac{1}{2} \quad (2.40)$$

where N is the largest subscript appearing in the equations.

Thus, the above equations give a closed-form representation of the dynamic equations for the velocity potential expansions in terms of prime potentials. Therefore, Equation (2.26) and its sine counterpart are a complete set of equations for rotor induced flow.

2.5 Equations in Terms of Derived Potentials

The next step is to make a change of variable from a series in terms of the prime potentials, Equation (2.12), to a series in terms of derived potentials, Equation (2.18). The change of variable is effected through a Galerkin procedure that relates the two sets of basis functions over the upper hemisphere. In particular, the total velocity potential is written in the two bases as below.

$$\left\{a_n^m\right\}^T \left[\Psi_n^{mc}\right] = \left\{\hat{a}_n^m\right\}^T \left\{\sigma_n^m \Phi_{n+1}^m + \varsigma_n^m \Phi_{n-1}^m\right\} \quad (2.41)$$

Then, the equations are dotted with the gradient of each potential function and integrated over the upper hemisphere, as with the momentum equations. The result is a transform between the two bases.

$$\left\{a_n^m\right\} = \left[\tilde{L}^c\right]^{-1} \left[M^c\right] \left\{\hat{a}_n^m\right\} \quad (2.42)$$

where

$$\left[M^c\right] = \left[\tilde{L}^c\right]_{\chi=0} = \left[\iint_s \frac{\partial \Phi_j^c}{d\tilde{\chi}} \Psi_n^{mc} ds\right] \quad (2.43)$$

A similar transform exists between b and \hat{b} that involves $\left[L^s\right]$ and $\left[M^s\right]$. Note that, in axial flow, the transformation is identity since the two potential functions $\left[M^c\right]$ and $\left[\tilde{L}\right]$ are identical in that case.

With the appropriate change of variable, the equation of motion in terms of the new variables is:

$$R\left[M^c\right] \left\{\dot{\hat{a}}_n^m\right\} + V_\infty \left[D^c\right] \left[\tilde{L}^c\right]^{-1} \left[M^c\right] \left\{\hat{a}_n^m\right\} = \left[D^c\right] \left\{\tau_n^{mc}\right\} \quad (2.44)$$

The version in Equation (2.44) allows a closed-form expression for all components of the velocity field in the entire upper hemisphere.

Interestingly, when the terms with $m+n$ even are truncated from Equation (2.44)—and when one limits oneself only to the normal component of flow at the disk—one recovers one of the two alternated forms of the He model of Ref. 4, namely the form with the $\tilde{\chi}$ -

velocities expanded in the $P_n'''(\nu)$. The other form of the He equations—the one with velocity expanded in terms of $(1/\nu)P_n'''(\nu)$ —is easily recovered by a change of variable. Similarly, the Pitt model of Ref. 1 is recoverable from the second form of the He model when it is truncated to only three states. Thus, the general form of Equation (2.44) explicitly includes all previous models.

Although the derived potentials have the advantage of being in closed form everywhere in the flow field, convergence with the derived potentials is slower at the lower frequencies than is convergence with the prime potentials, Ref. [4]. On the other hand, the convergence of velocities with the prime potentials is slower at the higher frequencies than is convergence with derived potentials. For this cause, it seems reasonable to formulate results in terms of a blending of the two types of potentials, as described below.

Once the equations are solved (in either basis), Equation (2.42) shows how the resultant states can be transformed into either basis for use in obtaining the flow field. We now define $\{\gamma\}$ and $\{\hat{\gamma}\}$ as the blending vectors for the Ψ and $\hat{\Psi}$ bases.

$$\vec{v} = \left\{ \vec{\nabla} \Psi \right\}^T \{\gamma\} + \left\{ \vec{\nabla} \hat{\Psi} \right\}^T \{\hat{\gamma}\} \quad (2.45)$$

where the total inflow must always add up to the original solution,

$$\{\gamma\} + [L^c]^{-1} [M^c] \{\hat{\gamma}\} = \{a\} \quad (2.46)$$

$$[M^c]^{-1} [L^c] \{\gamma\} + \{\hat{\gamma}\} = [M^c]^{-1} [L^c] \{a\} = \{\hat{a}\} \quad (2.47)$$

and where Equation (2.42) has been used for the transform. The blending of the two bases is based on the relative amount of unsteady flow in the dynamic response. Thus, for low-frequency motion, it is desired to have primarily the Ψ basis; whereas for high-frequency components, it is desired to have more of the $\hat{\Psi}$ basis. It follows that a logical manner to accomplish this blending is to base the relative proportion of Ψ and $\hat{\Psi}$ on the relative magnitude of the acceleration and velocity terms in the dynamic equations.

To this end, the acceleration component of flow field is defined as follows:

$$\{u\} \equiv \frac{-R}{V_\infty} [D^e]^{-1} [L^e] \left\{ \dot{a} \right\} = \{a\} - \frac{1}{V_\infty} \{\tau^e\} \quad (2.48)$$

Although the above is only written for the cosine component, one can easily extend this definition to include a vector of both sine and cosine terms.

Under this definition, the magnitude of the blended vectors can be rationally defined as:

$$\{\gamma\} = \frac{|a|^2}{|a|^2 + |u|^2} \{a\} \quad (2.49)$$

$$\{\hat{\gamma}\} = \frac{|u|^2}{|a|^2 + |u|^2} [M^e]^{-1} [L^e] \{a\} \quad (2.50)$$

One can see that, when the frequency goes to zero, acceleration term $u=0$; and the vector $\{\gamma\} = \{a\}$ while the vector $\{\hat{\gamma}\} = 0$ giving a solution in terms of prime potentials. On the other hand, at high frequencies, for which $|a|$ is small, the above formulation gives $\{\gamma\} = 0$ making the velocity expressed entirely in terms of $\{\hat{\gamma}\}$ which implies a velocity field in terms of derived potentials. For free vibrations —in which $\tau = 0$ — $\{u\}$ and $\{a\}$ are equal such

that the velocity field consequently is equally split between prime potentials and derived potentials.

An implicit assumption in the above is that the entire flow field is at a single frequency. In order to accommodate cases with mixed frequencies (such as a steady lift upon which is superimposed a 4/rev blade-passage input), we can make a simple modification to Equations (2.49-2.50). In particular, we can treat the blending factors (on the left of each equation) as diagonal matrices such that each diagonal term (and each component of flow) can have its own blending based on its own component of acceleration. For example, each harmonic partition (i.e., superscript, m) could have a factor based on the Euclidean length of that particular m -partition:

$$f^m = \frac{\{a^m\}^T \{a^m\}}{\left[\{a^m\}^T \{a^m\} + \{u^m\}^T \{u^m\} \right]} \quad (2.51)$$

This allows the zero-harmonic flow to be partitioned differently from (for example) the four-harmonic flow.

2.6 Effect of Lift Tilt

Makinen (Ref. 10) showed that the inflow model can indeed include the effect of tilt on the lift provided that a correction is applied for the swirl kinetic energy. Thus, the added energy is added to the mass matrix; and the resultant induced flow is assumed parallel to the tilted lift vectors.

To be precise, for the He model the apparent mass matrix $[K_n^m]$ (diagonal), must be replaced to include the effect of the wake swirl. There are different swirl corrections that can be applied, but from Ref. 10 the following correction gives the best results in axial flow.

$$[{}^{He}K_n^m] \text{ is substituted by: } \left[\sqrt{K_n^m} \right] \left[[I] + m \left(\frac{\kappa \lambda}{Q} \right)^2 \left[[I] - [A_{nj}^m]^2 \right]^{-m} \right] \left[\sqrt{K_n^m} \right] \quad (2.52)$$

where $\kappa = 2.2$, Q is the number of blades, λ is the total inflow, and $[A_{jn}^m]$ is the transformation matrix. It should be noted that for an actuator disk (no lift tilt), κ is set to zero.

To generalize Makinen's result to forward flight, λ is replaced by the average tangent of the wake skew angle.

$$\lambda^2 \rightarrow \frac{\lambda^2}{1 + \frac{3}{2} \mu^2} \quad (2.53)$$

Thus, the generalized form for the He model mass matrix for any harmonic m is given by

$$[{}^{He}K_n^m] \text{ is substituted by: } \left[\sqrt{K_n^m} \right] \left[[I] + m \frac{\kappa^2 \lambda^2}{Q^2 \left(1 + \frac{3}{2} \mu^2 \right)} \left[[I] - [A_{nj}^m]^2 \right]^{-m} \right] \left[\sqrt{K_n^m} \right] \quad (2.54)$$

This result can also be generalized to the complete model (in Ref. 7) for either the prime or derived potentials. For the derived potentials, the modified mass matrix is found by replacing the upper left partition of the matrix $[D]$ by the inverse of Eq. (2.54).

2.7 Velocity in Lower Hemisphere

The development on previous sections is a Galerkin method that gives convergence on velocity in the upper hemisphere only. The next issue is how to extend that convergence to the lower hemisphere. To begin that development, it is useful to consider the case of axial flow, for which closed-form solutions can be found for the z -component of velocity. For purposes here, it is sufficient to write the closed-form solution to Equation (2.6) in axial flow for a step response in pressure on either side of the disk. The pressure consequently becomes:

$$P(z, t) = P(z)u(t) \quad (2.58)$$

The resultant, closed-form solution for the z -component of velocity is given by:

$$\begin{aligned} \text{outside wake:} \quad & \rho V_\infty v_z(z, t) = P(z - V_\infty t) - P(z) \\ \text{inside wake:} \quad & \rho V_\infty v_z(z, t) = 2P(0^+) + P(z - V_\infty t) - P(z) \end{aligned} \quad (2.59)$$

where the region inside of the wake is defined by $\bar{r} < 1$ and $0 < z < V_\infty t$. Note that the above solution satisfies the momentum equation, the initial conditions, and the velocity jump across the disk.

$$\rho V_\infty [v_z(0^+) - v_z(0^-)] = P(0^+) + P(0^-) \quad (2.60)$$

The first term $P(z)$ is the particular solution to the applied pressure field, and the second term $P(z - V_\infty t)$ is the homogeneous solution that satisfies the initial conditions. One can think of the first term as the velocity due to the pressure drop at the disk and the second term as the velocity due to the shed vorticity (like a start-up vortex) that is being convected downstream. This solution satisfies the differential equation and initial conditions, but it

does not satisfy the continuity condition across the disk (or across the start-up region). Thus, in the wake, the extra term $2P(0^+)$ —the pressure on the downstream side of the disk—must be added to enforce this condition. Thus, the flow inside of the wake is no longer a potential flow. Interestingly, for pressure drops across the disk, since $P(z)$ is discontinuous across the disk, this extra term must be added to enforce continuity. For mass sources at the disk, for which pressure is continuous, the identical term must be added to enforce the velocity drop due to the extra flow, Equation (2.60). Thus, the same added term holds for all pressure inputs —lift or mass sources.

For example, for a step input in pressure drop (and after a sufficient amount of time), comparison of the “outside wake” and “inside wake” solutions shows that the velocity is continuous cross the disk and is given from the relationship $\rho V_\infty v = -P(0^-) = +P(0^+)$. This velocity then expands downstream to $2P(0^+)$ as the pressure drops, a well-known property of rotor wakes due to the Bernoulli equation. Further downstream, as one approaches the start-up system ($z = V_\infty t$), the velocity diminishes back down to $P(0^+)$; and then (outside of the wake) it further diminishes down to zero in the far field. It is the added term in the “inside wake” solution that allows for this correct description. This concept is easily extended to the general case through the use of a convolution integral involving the step response. Thus, for a general pressure input $P(z, t)$, the difference between the “outside wake” and “inside wake” z -velocity fields is:

$$\rho V_\infty v_z \Big|_{inside} = \rho V_\infty v_z \Big|_{outside} + 2P(0^+, t - z/V_\infty) \quad (2.61)$$

One can see that the added term is proportional to the downstream pressure that was on the disk at a past time (delayed by how long it took the wake to travel from the rotor to that particular z location).

From the above development, one can formulate an approximation to the velocity field below the plane of the rotor. For points outside of the wake, Equation (2.59) shows that the velocity is basically the analytic continuation of the velocity field above the disk. Thus, one can simply continue the potential functions into the lower hemisphere and find that velocity field there. Admittedly, the velocity expansion in the lower plane will converge more slowly than in the upper hemisphere with the convergence deteriorating as one approaches the downstream end of the wake. However, the velocity is decaying in that region so that errors are minimized. For velocities within the wake, one can take the extended lower hemisphere solution and add the term in Equation (2.61) in order to obtain an approximation for within the wake. One again, it is emphasized that this is only an approximation in that it neglects the shed “end wakes” for each oscillation. For example, for a time-varying, square-wave pressure, the above procedure will give the correct square-wave behavior in the wake only at low frequency. However, as frequency increases, and as the shape of the velocity wave begins to warp with respect to a square wave, the above procedure will be slow to converge on that warping.

To put the above in more concrete terms, for a rotor with lift concentrated at a finite number of concentrated blades, the inflow between the vortex sheets should be modeled

fairly accurately by the above; but the discontinuity at the vortex sheets will be slow to converge. Although this is not a perfect solution, it seems to be a practical solution.

Furthermore, the above approach is probably the best that can be done with closed-form velocity potentials and a Galerkin method. For skewed flow, the velocity below the plane of the disk is treated in entirely the same way with the accompanying approximations. Of course, in the limit as wake skew angle approaches 90° , the methodology breaks down as the wake goes to zero thickness and does not die out (even in the upper hemisphere). However, it should be pointed out that, even for that case, the flow on the disk still converges. It is only off-disk flow that cannot converge for 90° skew angle, Refs. [4-8]. It should be noted, however, that this approach **does** give the exact result for the flow at all wake skew angles (even 90°) for the case of steady flow in the wake. Thus, it is perfectly suited to issues of wake interactions with lifting surfaces.

In essence, the above development shows that one would require more states to model the flow in the wake than one would need to model the flow outside of the wake. This conclusion follows from the fact that, in a state-space approach, a pure time delay must be treated by extra states; and the above development involves a time delay in the wake. Therefore, for future work in this area, attention would need to be given to the incorporation of additional vortex states within the wake.

2.8 Nonlinearities

The above development is for flows that are linearized about V_∞ . Although this assumption is quite good in cruise conditions, it breaks down in the limit of a helicopter in hover. At the hover condition, V_∞ goes to 0; and the equations become singular. From the very inception of dynamic wake models, this was recognized. Fortunately, there is a fairly simple way to make the equations nonlinear in such a way that they agree exactly with momentum theory for the hover condition and then transition to the linearized case of Ref. [1]. To begin this development, it is useful to replace the V_∞ term with the total average flow at the rotor.

$$V_T = \sqrt{V_\infty^2 \sin^2 \chi + \left(V_\infty \cos \chi + \bar{v}_\zeta\right)^2} \quad (2.62)$$

However, this definition is not sufficient to create a model that will exactly linearize to the correct equation. For the correct linearization, one must consider the perturbation of the complete nonlinear equations which involves perturbation of the parameter defined as the mass-flow parameter, V .

$$V = \frac{d}{d\bar{v}_\zeta} \left(\bar{v}_\zeta V_T \right) = \frac{V_\infty^2 \sin^2 \chi + \left(V_\infty \cos \chi + \bar{v}_\zeta\right) \left(V_\infty \cos \chi + 2\bar{v}_\zeta\right)}{V_T} \quad (2.63)$$

The mass flow parameter allows the creation of a set of nonlinear equations that will agree with momentum theory in hover and also linearize to the correct equations derived above. In particular, one defines a diagonal, $[V]$ matrix,

$$[V] = \begin{bmatrix} V_T & & & \\ & V & & \\ & & V & \\ & & & V \\ & & & & \dots \end{bmatrix} \quad (2.64)$$

and then modifies Equation (2.26) or Equation (2.44) by replacing the scalar V_∞ with the insertion of the $[V]$ matrix just to the right of the $[D]$ matrix on the left-hand side of the equations.

$$R[\tilde{L}]\left\{\begin{smallmatrix} \bullet \\ a \end{smallmatrix}\right\} + [D][V]\{a\} = [D]\{\tau\} \quad (2.65)$$

$$R[M]\left\{\begin{smallmatrix} \bullet \\ \hat{a} \end{smallmatrix}\right\} + [D][V][L]^{-1}[M]\{\hat{a}\} = [D]\{\tau\} \quad (2.66)$$

The above equations are nonlinear about the elliptical pressure distribution τ_1^0 and thus must use only the average inflow due to that lift in determining the \bar{v} to go into the V_T and V parameters.

$$\bar{v} = \frac{2}{\sqrt{3}} \begin{Bmatrix} 1 \\ 0 \\ 0 \\ \dots \end{Bmatrix}^T [L]^{-1}[M]\{\hat{a}\} \quad (2.61)$$

The result is that the equations linearize to the equivalent of the original linear equations but with V_∞ of those equations replaced by V at all instances. This then reduces to the Pitt model of Ref. [1] when only three states are taken.

As a bi-product, one can see that (due to continuity) the nonlinear version implies a contracting of the rotor wake downstream as the induced velocity increases. This can readily be handled by redefining the “wake” region has having a smaller radius than the rotor. In particular, if one computes the average velocity at any circular cross-section of the wake (the

cut made parallel to the \tilde{x} -plane) and then calls that average velocity $\bar{v}(\xi)$, then we can write the equivalent radius as:

$$\left(\frac{R_{eq}}{R}\right)^2 = \frac{\bar{v}(0) + V_\infty}{\bar{v}(\xi) + V_\infty} \quad (2.62)$$

where ξ will be negative in the wake. This will ensure continuity. The flow outside of this new wake definition will remain the out-of-wake solution

The above is a nonlinear model for velocity that follows Refs. [1-4] in how the nonlinearities due to hover are treated in the velocity field. However, none of those references discusses how the nonlinear pressure field differs from the linearized one. The difference is clearly seen for the lifting case in hover for which the linear theory predicts equal and opposite pressures on either side of the disc —giving a total pressure increase of $2P(0^+) = -2P(0^-)$. Momentum theory, on the other hand, shows that the positive pressure below the disk is $3/4$ of the total pressure rise while the negative pressure above the disk is $1/4$ of the total. The reconciliation of this anomaly is easily found by substitution of the nonlinear velocity field into Bernoulli's equation. With this procedure, the nonlinear pressure in the flow field can be written in terms of the linearized pressures (written in terms of τ) as follows.

$$\text{Outside of wake:} \quad \frac{P}{\rho} = \frac{P_0}{\rho} - \frac{1}{2} \vec{v} \cdot \vec{v} - v_\xi V_\infty \quad (2.69)$$

$$\text{Inside of wake:} \quad \frac{P}{\rho} = \frac{P_0}{\rho_0} + \frac{2P(0^+)}{\rho} - \frac{1}{2} \vec{v} \cdot \vec{v} - v_\xi V_\infty \quad (2.70)$$

where P_0 is the total atmospheric pressure in the far field, V_∞ is the free-stream velocity, $P(0^+)$ is the pressure (above atmospheric) applied below the disk (whether from lift differential or mass sources at rotor), v is the nonlinear induced velocity from the nonlinear inflow theory described above, and v_ξ is the component of v along the negative ξ direction (the free-stream direction of V_∞). For the perturbation (i.e., linearized) model, it follows that:

$$\text{Outside of wake:} \quad \frac{\tilde{P}}{\rho} = -\vec{v} \cdot \vec{v} - v_\xi V_\infty \quad (2.71)$$

$$\text{Inside of wake:} \quad \frac{\tilde{P}}{\rho} = \frac{2P(0^+)}{\rho} - \vec{v} \cdot \vec{v} - v_\xi V_\infty \quad (2.72)$$

where \tilde{P} is the perturbation pressure, v is the perturbation induced velocity, and v_ξ is the perturbation velocity in the free-stream direction, and \bar{v} is the steady induced flow about which the equations are being perturbed. This, then, completes a non-linear model and a perturbation nonlinear model of the inflow theory.

2.9 Results from previous models

Many results from this unified approach are available (Refs. 1-14) including comparisons with experimental data and with other theories. The results present velocity components in the plane of the rotor disk for the linear equations with simple harmonic pressure or mass-source inputs. In all results, ten odd functions and ten even functions are used in the Galerkin computations. For the case of frequency response, there is an exact numerical

solution based on a convolution integral along streamlines from far upstream to the point at which induced flow is desired. Thus, the comparisons to follow are validation that the potential functions and the Galerkin-based equations are correct.

A complete dynamic wake model has been derived from a Galerkin procedure applied to the potential flow equations. The resultant velocity potentials give converged solutions both above the disk, on the disk, below the disk and in the wake. Previous inflow models such as momentum theory, Pitt model, and the He model are contained as special cases.

Chapter 3

Development of the Solution Approach

In an attempt to understand how the tilt, the number of blades and the geometry of the blades in a real rotor affect the induced power the present research will expand He's generalized dynamic wake model to study minimum induced power for a rotor under a variety of conditions. The scope of such a study is so broad that the use of large, comprehensive codes is prohibitive for these purposes. On the other hand, finite-state wake models are ideally suited for such task. These models expand both the pressure field and the velocity field in orthogonal expansion functions. Therefore, the computation of induced power (the dot product of thrust and induced flow) simplifies nicely into a quadratic cost function that allows classical optimization to be used for the minimum power under a variety of constraints. Thus, it is anticipated that such an approach can yield insight into this issue. As a preliminary step in such an endeavor, this present dissertation looks at the induced power of a non-ideal lifting rotor in axial flow to verify that dynamic wake models can indeed compute the proper induced power.

Since theory and experiment agree with simple momentum approaches for power in axial flow, such conditions provide the ideal test bed to verify that this optimization approach is

viable. The remaining of the research efforts will then concentrate on results for induced power in forward flight, using the formulation already derived and included on this dissertation.

3.1 Induced Power Derivation from He-Peters

He [4] developed an unsteady induced-flow theory to be used in stability, vibration, control, and aeroelastic studies. The theory is based on an acceleration potential for an actuator disk. The induced flow, w , is expressed in a polynomial distribution (proportional to Legendre functions) radially and in terms of a Fourier series azimuthally. The way the induced flow is set up allows for all harmonics and describes the induced flow for any radial position.

The theory provides the pressures on the rotor disk as a Fourier expansion. As more harmonics are added, that pressure converges to the lift concentrations on the blade and to zero lift off the blade. One of the issues to be addressed in this present work is whether or not such an approach can give adequate convergence to induced power. The form of this pressure expansion is as follows:

$$\Phi(\nu, \bar{\eta}, \bar{\psi}, \bar{t}) = \rho \Omega^2 R^2 \sum_{m=0}^{\infty} \sum_{n=m+1, m+3, \dots}^{\infty} P_n'''(\nu) Q_n'''(i\bar{\eta}) \left[C_n'''(\bar{t}) \cos(m\bar{\psi}) + D_n''' \sin(m\bar{\psi}) \right] \quad (3.1)$$

The pressure at the rotor disk is obtained by the difference between the pressure above and the pressure below the disk.

$$\Delta P(\bar{r}, \psi, t) = \rho \Omega^2 R^2 \sum_{m=0}^{\infty} \sum_{n=m+1, m+3, \dots}^{\infty} \bar{P}_n^m(\nu) \left[\tau_n^{mc}(\bar{t}) \cos(m\psi) + \tau_n^{ms}(\bar{t}) \sin(m\psi) \right] \quad (3.2)$$

The power, \mathcal{Q} , can be expressed as:

$$\mathcal{Q} = \iint_A \Delta P(w + \nu) \kappa dx d\psi \quad (3.3)$$

The Peters-He model also sets out the velocity field normal to the rotor disk in terms of the same Legendre Functions and variables, as given below.

$$w(\bar{r}, \psi, \bar{t}) = \Omega R \sum_{m=0}^{\infty} \sum_{n=m+1, m+3, \dots}^{\infty} \phi_n^m(\bar{r}) \left[\alpha_n^m(\bar{t}) \cos(m\psi) + \beta_n^m(\bar{t}) \sin(m\psi) \right] \quad (3.4)$$

$$\phi_n^m(\bar{r}) \equiv \frac{1}{\nu} \bar{P}_n^m(\nu) \quad (3.5)$$

where $\bar{t} = \Omega t$, and $\phi_n^m(\bar{r})$ are a complete set of functions that arise from the solution to

Laplace's equation in ellipsoidal coordinates.

The form of the functions is:

$$\phi_n^m(\bar{r}) = \sqrt{(2n+1)H_n^m} \sum_{q=m, m+2, \dots}^{\infty} \bar{r}^q \frac{(-1)^{(q+m)/2} (n+1)!!}{(q-m)!! (q+m)!! (n-q-1)!!} \quad (3.6)$$

$$\text{where } H_n^m = \frac{(n+m-1)!!(n-m-1)!!}{(n+m)!!(n-m)!!}$$

substitution of the induced flow and the pressure at the disk yields:

$$\mathcal{Q} = \rho \Omega^3 R^5 \sum_{m,n} \int_0^{2\pi} \int_0^1 \left[\lambda + \sum_{r,j} \frac{1}{\nu} \bar{P}_j^r(\nu) \left(\alpha_j^r \cos(r\psi) + \beta_j^r \sin(r\psi) \right) \right] \left[\bar{P}_n^m(\nu) \left(\tau_n^{mc} \cos(m\psi) + \tau_n^{ms} \sin(m\psi) \right) \right] \nu d\nu d\psi \quad (3.7)$$

$$\begin{aligned}
Q = 2\pi\rho\Omega^3 R^5 \int_0^1 \sum_n \left[\lambda + \sum_j \phi_j^0 \alpha_j^0 \right] \bar{P}_n^0 \tau_n^{0c} \nu d\nu \\
+ \pi\rho\Omega^3 R^5 \int_0^1 \sum_{m,n} \sum_j \left\{ \left[\phi_j^m \alpha_j^m \right] \bar{P}_n^m \tau_n^{mc} + \left[\phi_j^m \beta_j^m \right] \bar{P}_n^m \tau_n^{ms} \right\} \nu d\nu
\end{aligned} \tag{3.8}$$

The functions P_n^m are Legendre Functions of the first kind, and ν is related to the radial position be $r = \sqrt{1-\nu^2}$.

The equations that relate the pressure coefficients in the pressure expansion $(\tau_n^{mc}, \tau_n^{ms})$ to the velocity coefficients (α_j^r, β_j^r) are derived from the momentum equation of potential flow.

$$\left[K_n^m \right] \{\dot{\alpha}_n^m\} + V \left[\tilde{L}^c \right]^{-1} \{\alpha_n^m\} = \frac{1}{2} \{\tau_n^{mc}\} \tag{3.9}$$

$$\left[K_n^m \right] \{\dot{\beta}_n^m\} + V \left[\tilde{L}^s \right]^{-1} \{\beta_n^m\} = \frac{1}{2} \{\tau_n^{ms}\} \tag{3.10}$$

where $(\dot{}) = \frac{d}{dt}$, $V = \frac{\mu^2 + (\lambda + \nu)\lambda}{\sqrt{\mu^2 + \lambda^2}}$, λ is the total inflow, μ is the advance ratio, V is the

flow parameter, and K_n^m is diagonal; $K_n^m = \frac{2}{\pi} H_n^m$. The $[\tilde{L}]$ cosine and sine matrices are

given in closed form in terms of the wake skew angle, χ .

$$\Gamma_{jn}^{mr} = \frac{(-1)^{\frac{n+j-2r}{2}}}{\sqrt{H_n^m H_j^r}} \frac{2\sqrt{(2n+1)(2j+1)}}{(j+n)(j+n+2)[(j-n)^2-1]} \quad \text{for } r+m \text{ even}$$

$$\Gamma_{jn}^{mr} = \frac{\pi}{2\sqrt{H_n^m H_j^r}} \frac{\text{sign}(r-m)}{\sqrt{(2n+1)(2j+1)}} \quad \text{for } r+m \text{ odd, } j=n\pm 1$$

$$\Gamma_{jn}^{mr} = 0 \quad \text{for } r + m \text{ odd, } j \neq n \pm 1 \quad (3.11)$$

$$\begin{aligned} \left[\tilde{L}_{jn}^{0m} \right]^c &= X^m \Gamma_{jn}^{0m} \\ \left[\tilde{L}_{jn}^{rm} \right]^c &= \left[X^{|m-r|} + (-1)^l X^{|m-r|} \right] \Gamma_{jn}^{rm} \\ \left[\tilde{L}_{jn}^{rm} \right]^s &= \left[X^{|m-r|} - (-1)^l X^{|m-r|} \right] \Gamma_{jn}^{rm} \end{aligned} \quad (3.12)$$

where $l = \min(r, m)$, $X = \tan|\chi/2|$. The forcing functions, τ_n^m , are given in terms of the blade loading, L_q . These are related to the pressure and the optimization of the induced power will yield an optimal pressure distribution for a given thrust coefficient.

$$\begin{aligned} \tau_n^{0c} &= \frac{1}{2\pi} \sum_{q=1}^Q \left[\int_0^1 \frac{L_q}{\rho \Omega^2 R^3} \phi_n^0(\bar{r}) d\bar{r} \right] \\ \tau_n^{mc} &= \frac{1}{\pi} \sum_{q=1}^Q \left[\int_0^1 \frac{L_q}{\rho \Omega^2 R^3} \phi_n^m(\bar{r}) d\bar{r} \right] \cos(m\psi_q) \\ \tau_n^{ms} &= \frac{1}{\pi} \sum_{q=1}^Q \left[\int_0^1 \frac{L_q}{\rho \Omega^2 R^3} \phi_n^m(\bar{r}) d\bar{r} \right] \sin(m\psi_q) \end{aligned} \quad (3.13)$$

For the Peters-He model in its actuator-disk form, we have a skewed wake as shown in Figure 3.1 below.

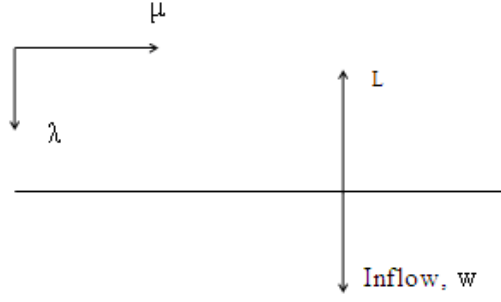


Figure 3.1: Normalized velocity components.

The power \mathcal{Q} can be found from Equation (3.3) to be:

$$\mathcal{Q} = \iint_A \Delta P (w + v) x dx d\psi$$

Notice that the power does not depend on the velocity component u . The pressure at the disk (as shown in Equation (3.2)) is:

$$\Delta P(\bar{r}, \psi, t) = \rho \Omega^2 R^2 \sum_{m=0}^{\infty} \sum_{n=m+1, m+3, \dots}^{\infty} \bar{P}_n^m(\nu) \left[\tau_n^{mc}(\bar{t}) \cos(m\psi) + \tau_n^{ms}(\bar{t}) \sin(m\psi) \right]$$

The advance ratio is a non-dimensional parameter used for a rotor in forward flight that is the ratio of the axial component of the incoming velocity and the rotational velocity of the rotor, shown in Equation (3.14) and sketched in Figure 3.1. Some other significant parameters are defined for convenience.

$$\text{Advance ratio } \mu = \frac{U}{\Omega R} \quad (3.14)$$

$$\text{Climb rate } \lambda = \frac{V}{\Omega R} \quad (3.15)$$

$$\text{Non-dimensional radial position } \bar{r} = \frac{r}{R} \quad (3.16)$$

$$\text{Non-dimensional inflow } \bar{v} = \frac{v}{\Omega R} \quad (3.17)$$

Note that $rdr = -v dv$, and λ and μ are constant.

The inflow is given by Equation (3.4). Introducing the definitions for pressure change, v from the climb rate, and the induced velocity we obtain the expression for the power where the climb rate, λ , is a constant. The normalized Legendre function is $\bar{P}_1^0 = \sqrt{3}v$ by definition. Introduction of it into the expression for the power yields Equation (3.18). By the use of the simple relationship between power and power coefficient, we obtain the following,

$$\begin{aligned} \mathcal{Q} = & 2\pi\rho\Omega^3 R^5 \int_0^1 \sum_n \left[\lambda + \sum_j \frac{1}{v} \bar{P}_j^0 \alpha_j^0 \right] \bar{P}_n^0 \tau_n^{0c} v dv \\ & + \pi\rho\Omega^3 R^5 \int_0^1 \sum_{m,n} \sum_j \left\{ \left[\frac{1}{v} \bar{P}_j^m \alpha_j^m \right] \bar{P}_n^m \tau_n^{mc} + \left[\frac{1}{v} \bar{P}_j^m \beta_j^m \right] \bar{P}_n^m \tau_n^{ms} \right\} v dv \end{aligned} \quad (3.18)$$

$$C_P = \frac{\mathcal{Q}}{\pi\rho\Omega^3 R^5} = 2 \left(\frac{\lambda}{\sqrt{3}} + \alpha_1^0 \right) \tau_1^{0c} + 2 \sum_{n=3,5,\dots} \alpha_n^0 \tau_n^{0c} + \sum_{m=1,2,3,\dots} \sum_{j=m+1,m+3,\dots} \left[\alpha_j^m \tau_j^{mc} + \beta_j^m \tau_j^{ms} \right] \quad (3.19)$$

and

$$C_T = \frac{1}{\pi} \int_0^{2\pi} \int_0^1 \cos \varphi \sum_{m,n} \bar{P}_n^m(v) \left[\tau_n^{mc} \cos(m\psi) + \tau_n^{ms} \sin(m\psi) \right] v dv d\psi \quad (3.20)$$

A simple check using $m = 0$ only, and $n = 1$ only, provides the common expression that shows the Peters-He model agrees with the induced power from Momentum Theory. The lift and pressure coefficients for this special case are shown in Equations (3.21) through (3.23).

$$\alpha_1^0 = \frac{1}{\sqrt{3}} \bar{v} \quad (3.21)$$

$$\tau_1^{0\epsilon} = \frac{\sqrt{3}}{2} C_T \quad (3.22)$$

$$C_P = \frac{2}{\sqrt{3}} (\lambda + \bar{v}) \frac{\sqrt{3}}{2} C_T = C_T (\lambda + \bar{v}) \quad (3.23)$$

Equations (3.19) and (3.20) provide the framework for a classical, quadratic optimization of power subject to constant thrust.

3.2 Induced Power Theorem

A Rotor Induced-Power Theorem is used to verify the approach of this work. Let a rotor, Figure 3.2, be moving along an arbitrary, straight path through still air with a velocity W . Let χ be the angle between the flight path and a vertical to the rotor.

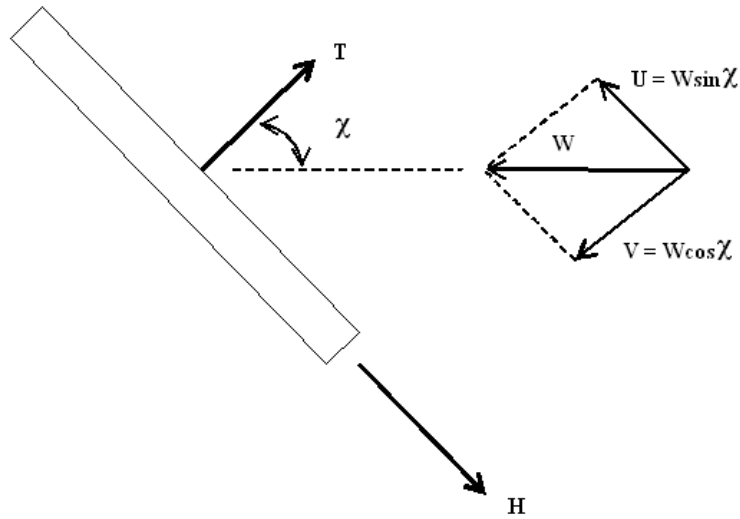


Figure 3.2: Inflow velocity components for a moving rotor.

It follows that the inplane component of air velocity as seen by the rotor is $U = W \sin \chi$ and the normal component is $V = W \cos \chi$.

Let the rotor loading perpendicular to rotor plane be called T and the rotor load in plane be called H , each with a positive sense in the direction of the flight path (i.e., opposite to V and U). Let the blades in the rotor disk be rotating counter-clockwise at angular velocity Ω , when looking down on the rotor, and let ψ be the azimuth angle of a blade as measured from aft, $\psi = \Omega t$. Let a generic point on the blade be a radial distance x from the center of rotation as shown on Figure 3.3.

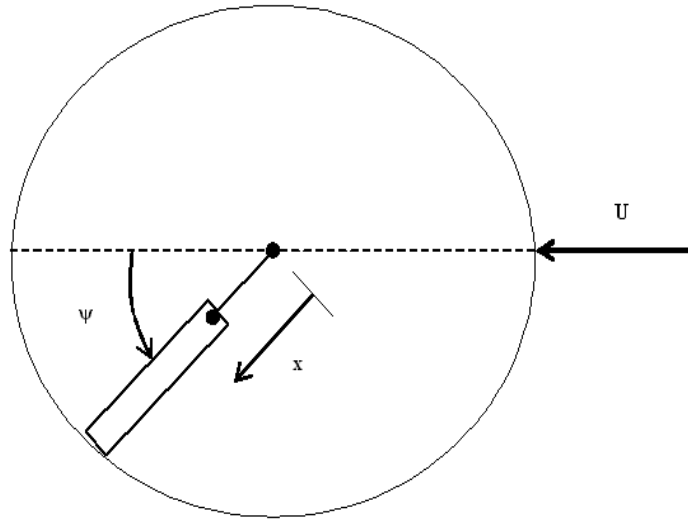


Figure 3.3: Rotor blade generic position and rotating angle.

Let φ be the inflow angle as seen in the local blade system, Figures 3.3 and 3.4. In that system, let dL be the incremental local lift per unit length (perpendicular to the total inflow),

let dD be the incremental local induced drag per unit length, and let dT be the incremental thrust. Let w be the induced flow, opposite to L , Figure 3.4.

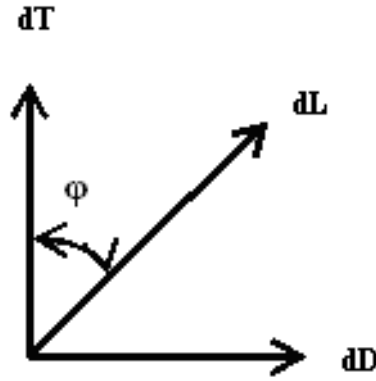


Figure 3.4: Geometry of the forces on the blade.

$$dT = dL \cos \varphi \quad (3.24)$$

$$dD = dL \sin \varphi \quad (3.25)$$

$$dH = -dD \sin \psi \quad (3.26)$$

Figure 3.5, taken from the work of Glauert [15], shows the geometry of the flow in the blade coordinate system. The relative flow due to rotor motion alone is $\Omega x + U \sin(\psi)$ in the rotor plane and V perpendicular to that plane. The induced flow w must be parallel to the lift, so it is added vectorally at the angle φ as shown. The resultant total inflow (due to rotor motion and due to induced flow) must be perpendicular to the local incremental lift, due to circulation considerations. Therefore, w can be considered perpendicular to the total flow vector. The resultant relationship gives rise to the geometry in the figure and to the following identities:

$$\tan \varphi = \frac{w \cos \varphi + V}{\Omega x - w \sin \varphi + U \sin \psi} = \frac{V + \frac{w}{\cos \varphi}}{\Omega x + U \sin \psi} \quad (3.27)$$

$$\sin \varphi = \tan \varphi \cos \varphi = \frac{V \cos \varphi + w}{\Omega x + U \sin \psi} \quad (3.28)$$

The above can be used to transform the induced power equations.

$$P_I = P_s - TV - HU \quad (2.1)$$

$$P_I = L\Omega x \sin \varphi - L \cos \varphi V + L \sin \varphi \sin \psi U \quad (3.29)$$

$$P_I = L(\Omega x + U \sin \psi) \sin \varphi - LV \cos \varphi \quad (3.30)$$

(where the differentials are omitted for clarity).

But $\sin \varphi = \frac{V \cos \varphi + w}{\Omega x + U \sin \psi}$. Therefore

$$P_I = LV \cos \varphi + Lw - LV \cos \varphi = Lw \quad (3.31)$$

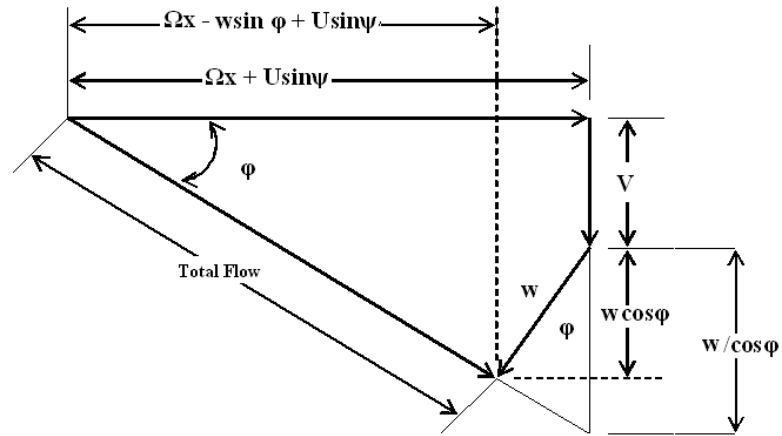


Figure 3.5: Geometry of the flow.

The induced power is, then:

$$\boxed{P_I = Lw} \quad (\text{work done by } L \text{ on } w) \quad (3.32)$$

Thus, the incremental induced power can be found from the integral of the dot product of the local lift and local induced flow, which is the work done on the flow field. The above theorem is, strictly-speaking, exactly true only for axial flow because of the assumption that local lift is parallel to local induced flow. On the other hand, that assumption is less and less important as one transitions away from hover. Furthermore, it is exactly true that the work done on the flow field will equal the induced power. Therefore, Equation (3.32) seems a valid approach to computing the induced power from a dynamic wake model.

3.3 General Optimization

A general classical quadratic optimization problem is stated as follows:

Minimize $\{x\}^T [A] \{x\}$ subject to $\{c\}^T \{x\} = q$ (given). Use of Lagrange's multiplier to include the constraint leads to the cost function:

$$J = \frac{1}{2} \{x\}^T [A] \{x\} - \Lambda \{c\}^T \{x\} \quad (3.33)$$

where Λ is the Lagrange multiplier. Optimizing, we obtain that for the change of the functional to be zero

$$\delta J = \{\delta x\}^T \left[\frac{1}{2} [A + A^T] \{x\} - \Lambda \{c\} \right] = 0 \quad (3.34)$$

$$\{x\} = \left[\frac{1}{2} ([A] + [A]^T) \right]^{-1} \{c\} \Lambda \quad (3.35)$$

Notice that the matrix to be inverted is the symmetric part of $[A]$.

The Lagrange multiplier must be chosen such that:

$$\Lambda = \frac{q}{2\{c\}^T \left[[A] + [A]^T \right]^{-1} \{c\}} \quad (3.36)$$

The above derivation provides a general guide for classical quadratic optimizations, such as the one that is performed for the present research. The Lagrange multiplier will be chosen as specified by equation (3.36) for our special case of an optimum rotor.

3.4 General Figure of Merit Definition

Figure of merit is a measure of rotor efficiency. It is defined as the ratio of minimum or ideal power required to hover to the actual power required. It compares actual rotor performance with the performance of an ideal rotor.

$$F.M. = \frac{\text{minimum possible power required to hover}}{\text{actual power required to hover}}$$

Note that the ideal figure of merit, or the figure of merit for an ideal rotor, should equal unity. The closer the figure of merit is to unity for a given rotor, the more efficient the rotor is.

In this thesis, we extend this definition of the figure of merit to climb and to forward flight by the definition

$$F.M. = \frac{\text{minimum induced power at any flight condition}}{\text{actual induced power at that flight condition}}$$

Chapter 4

Results

The classical results for the cases of axial flow, plus the case of an actuator disk with an infinite number of blades in skewed flow are given in this section. The finite-state method used in this research needs to be verified. For the purpose of verification, solutions are obtained from classical assumptions and procedures to be compared to the results obtained by the current approach.

4.1 Classical Theories: Axial and Skewed Flows

4.1.1 Momentum Theory

Momentum theory utilizes the basic fluid mechanics conservation laws (Ref. 25) to predict the behavior of a rotor, modeled as an actuator disk. Conservation of mass, momentum and energy equations yield results for optimum induced velocity and pressure distributions for an actuator disk in hover or climbing and a given thrust [16].

Consider an actuator disk of area A , with a thrust, T , moving vertically with a velocity V as shown in Figure 4.1. Consider a well defined slipstream that goes from an area of A_1 , far upstream, to an area A_2 far downstream of the actuator disk. Across the disk, the velocity increases to $(V + v)$ due to the change in pressure at the location of the disk. Downstream, the velocity is the addition of the incoming and induced velocities, $(V + w)$. Applying conservation of momentum, we obtain that the power is:

$$P = \int \Delta p (V + v) dA \quad (4.1)$$

where Δp is the pressure difference across the rotor.

Applying Bernoulli's equation upstream and downstream of the actuator disk along streamlines, the expression for the pressure difference across the rotor is:

$$\Delta p = \frac{1}{2} \rho (2Vw + w^2) \quad (4.2)$$

where ρ is the density.

Therefore the power, P becomes:

$$P = \int \frac{1}{2} \rho (2Vw + w^2) (V + v) dA_2 \quad (4.3)$$

Applying conservation equations, we obtain the thrust to be:

$$T = \int \rho (V + w) w dA_2 \quad (4.4)$$

The objective is to obtain the minimum power distribution (equation (4.3)) for a given thrust (Equation (4.4)). Basically, this is an optimization problem for a functional, P , subject to a constraint, T . We would like to obtain the induced velocity distribution $w(r)$ that minimizes the power. Euler's equation below can be used to find the distribution $w(r)$.

$$\frac{\partial}{\partial r} \left(\frac{1}{2} \rho (2Vw + w^2) (V + v) + \lambda (\rho (V + w) w) \right) - \frac{d}{dt} \left[\frac{\partial}{\partial r'} \left(\frac{1}{2} \rho (2Vw + w^2) (V + v) + \lambda (\rho (V + w) w) \right) \right] = 0 \quad (4.5)$$

where λ here is the Lagrange multiplier.

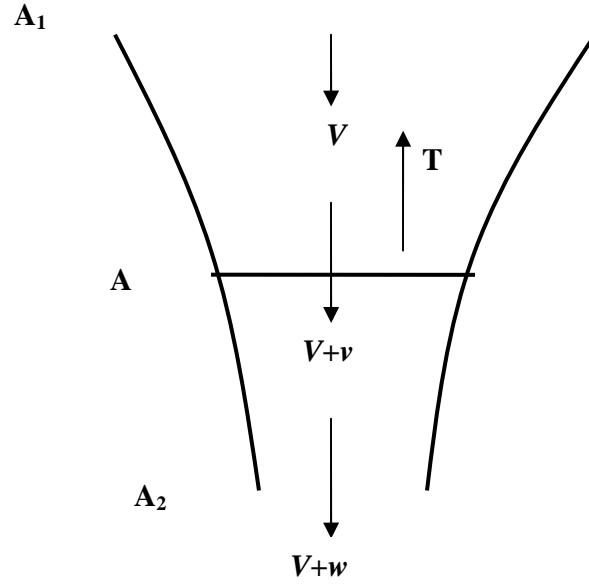


Figure 4.1: Flow model for an actuator disk in axial flow.

Since the expressions are independent of r , it follows that the solution for the minimization problem is that w be constant. The optimum induced velocity distribution is therefore a constant or uniform distribution. If this value is introduced into Equation (4.2), the

resulting pressure distribution that produces minimum induced power is found to be a constant or uniform distribution also.

From momentum theory for uniform induced flow the thrust and power coefficients are defined as:

$$C_T = 2(\eta + \nu)\nu \quad (4.6)$$

$$C_p = 2(\eta + \nu)^2 \nu = (\eta + \nu)C_T \quad (4.7)$$

In Equations (4.6) and (4.7), we normalize the velocities and power on C_T as follows

$$\bar{\nu} = \frac{\nu}{\sqrt{C_T/2}}, \quad \bar{\eta} = \frac{\eta}{\sqrt{C_T/2}}, \quad \bar{C}_p = \frac{\sqrt{2}C_p}{C_T^{3/2}} \quad (4.8)$$

Since Equations (4.6) and (4.7) are the equations for uniform (which is minimum power), we can solve for the minimum possible \bar{C}_p (total power) and $\bar{C}_p - \bar{\eta}$ (induced power)

$$\bar{C}_p = \frac{\bar{\eta}}{2} + \sqrt{1 + \left(\frac{\bar{\eta}}{2}\right)^2} \quad (4.9)$$

$$\bar{C}_{PI} = \bar{C}_p - \bar{\eta} = \frac{-\bar{\eta}}{2} + \sqrt{1 + \left(\frac{\bar{\eta}}{2}\right)^2} \quad (4.10)$$

It is helpful to rewrite Equation (4.10) by multiplying numerator and denominator

by $\frac{\bar{\eta}}{2} + \sqrt{1 + \left(\frac{\bar{\eta}}{2}\right)^2}$. This gives an alternate form of the minimum induced power

$$\bar{C}_{PI} = \left[\frac{\bar{\eta}}{2} + \sqrt{1 + \left(\frac{\bar{\eta}}{2}\right)^2} \right]^{-1} \quad (4.11)$$

For axial flow ($\bar{\eta} = 0$), the minimum \bar{C}_{PI} is 1.0. This is why the figure of merit in hover can be defined as $[\bar{C}_{P \text{ actual}}]^{-1}$. Note that in climb, the minimum induced power is less than unity and approaches $1/\bar{\eta}$ for $\bar{\eta} \gg 1$. Thus, the figure of merit in axial flow is $\bar{C}_{PI}/\bar{C}_{P \text{ actual}}$ when \bar{C}_{PI} is from Equation (4.11).

Comparison of momentum theory results with finite state methods can be performed by the use of optimum pressure and induced velocity profiles. Therefore, the plot for this minimum induced power will not be shown. However, it is important to see the expression for it as it provides a baseline against which to measure efficiency, and we can obtain valuable information such as the tendency of the efficiency with respect to the climb, the shape of the curve, etc..

A similar approach is followed to obtain the optimum induced velocity profile and the optimum pressure distribution for skewed flow. As in hover, the induced power or power loss can be analyzed from the induced velocity. The difference is that, while in forward flight, the edgewise velocity component of the incoming flow has to be accounted for in the calculations. The induced velocity is assumed to be a constant in hover.

Momentum theory shows that the optimum pressure distribution for an actuator disk with an infinite number of blades in skewed flow is a constant, whereas the inflow velocity distribution is no longer a constant.

4.1.2 Prandtl's Approximation

In 1919, Betz and Prandtl [18] combined momentum and blade-element theory to obtain a correction factor, k that must be added to the absolute performance calculations for a rotor to account for tip losses. The tip losses occur due to the reduction in the thrust near the blade tips when a system with a finite number of blades is considered.

The effect of a finite number of blades is to give a further loss in wake energy due to the individual vortex sheets from each blade. Goldstein worked out the exact effect for optimized rotors. Prandtl's approximate correction factor, [16], [17], [18], agrees very well with Goldstein for moderate climb rates. Because of this tip loss, for a given thrust, there is more induced flow than predicted by momentum theory. Using these principles an approximation to the theoretical figure of merit for an actuator disk or a lifting rotor for a finite number of blades can be obtained using Prandtl formulation. The Prandtl k factor is applied as follows.

$$dL = (2\pi r dr) \rho (V + v) (2v) k$$

where

$$k = \frac{2}{\pi} \cos^{-1} \left[\exp \left(\frac{-Q(1-r)}{2\lambda} \right) \right] \quad (4.12)$$

From the above expression it is seen that near the root ($r \rightarrow 0$) the correction factor is close to the unity, and it decreases as the radial position moves along the blade towards the tip. This formula will be used in the results to follow.

Prandtl's result can be used to obtain an approximate expression for the figure of merit for the case of an actuator disk (lift perpendicular to the rotor), in axial flow and for the case of finite number of blades as follows.

$$F.M._{\text{Prandtl}} = 2 \int_0^1 k r dr \quad (4.13)$$

Later in this thesis, we will utilize Eq. (4.13) and compare with other case.

4.1.3 Betz Distribution

When the lift vector is tilted perpendicular to the vortex sheets, the ideal power is no longer attainable. Thus, uniform flow is no longer the optimum condition. Betz [18] determined that the minimum power is obtained when the induced flow at the individual blades is such that the vortex sheet remains along a helical path. Thus, the optimum inflow distribution is proportional to $\cos\varphi$, Figure 3.5. For an infinite number of blades, it follows that the pressure field must follow this same shape. Thus, let the optimum pressure at the rotor be:

$$\Delta P = \frac{\Lambda V}{2} \cos \varphi = \frac{\Lambda V}{2} \frac{r}{\sqrt{r^2 + \lambda^2}} \quad (4.14)$$

where Λ is a Lagrange multiplier. Then the induced velocity, w is:

$$w = \frac{1}{2V} \Delta P = \frac{\Lambda}{4} \frac{r}{\sqrt{r^2 + \lambda^2}} \quad (4.15)$$

The thrust coefficient is :

$$C_T = 2 \int_0^1 \Delta P \cos \varphi r dr = \Lambda V \int_0^1 \cot \varphi r dr = \Lambda V \int_0^1 \frac{r^3}{r^2 + \lambda^2} dr \quad (4.16)$$

Division of both sides by C_T , introduction of the normalized values $\bar{\Lambda} = \frac{\Lambda}{\sqrt{C_T/2}}$ and

$\bar{V} = \frac{V}{\sqrt{C_T/2}}$, and with $y \equiv r/\lambda$ we obtain an expression that can be integrated to obtain a

close form expression for the figure of merit of the Betz distribution.

$$1 = \frac{\bar{\Lambda}\bar{V}}{2} \lambda^2 \int_0^{1/\lambda} \frac{y^3}{1+y^2} dy \quad (4.17)$$

Integration on Equation (4.17) gives the value of the normalized Lagrange multiplier to be:

$$\bar{\Lambda} = \frac{4}{\bar{V}} \frac{1}{1 - \lambda^2 \ln\left(1 + \frac{1}{\lambda^2}\right)} \quad (4.18)$$

To obtain the induced power coefficient, we must consider the power.

$$C_P = 2 \int_0^1 \Delta P_{wr} dr = \frac{\Lambda^2 V}{4} \int_0^1 \frac{r^3}{r^2 + \lambda^2} dr \quad (4.19)$$

Then, the normalized power coefficient is:

$\bar{C}_{P_i} = \frac{C_P}{2(C_T/2)^{3/2}}$, which provides the final expression for the normalized induced power.

$$\bar{C}_{P_i} = \frac{\bar{\Lambda}}{4} = \frac{1}{\bar{V}} \frac{1}{1 - \lambda^2 \ln\left(1 + \frac{1}{\lambda^2}\right)} \quad (4.20)$$

For axial flow, $\bar{V} = \bar{\lambda} = \bar{\eta} + \bar{v} = \frac{\bar{\eta}}{2} + \sqrt{\frac{\bar{\eta}^2}{4} + 1} = \frac{1}{\bar{C}_{P_i}}$.

The result of this closed-form solution yields the expression for the ideal figure of merit for a lifting rotor with an infinite number of blades. Rearranging the previous equations, one obtains:

$$F.M._{Betz} = 1 - \lambda^2 \ln \left(1 + \frac{1}{\lambda^2} \right) \quad (4.21)$$

It is interesting that Betz never provided a solution for the figure of merit of his distribution, but provided all the necessary theoretical background to obtain this closed-form expression for the efficiency.

One can combine the Betz distribution with the Prandtl tip-loss correction to obtain an approximate figure of merit for tilted lift and tip losses.

$$F.M._{Prandtl} = 2 \int_0^1 k \cos^2 \phi r dr \quad (4.22)$$

This expression must be determined numerically.

4.1.4 Goldstein's Distribution

Prandtl gives an approximate solution for the effect of blade number on the Betz optimum distribution. The accuracy of this approximation is better as the number of blades increases and as the ratio of the tip speed to the advancing velocity becomes larger (inverse of the advance ratio). Goldstein solved for the exact optimum circulation distribution using Betz's velocity distribution for an optimally efficient propeller. He was able to obtain the exact solution, and that in fact it was very close to the approximate solution provided by Prandtl.

Figure 4.2 shows the results of the two methods for two and four-bladed propellers. It gives the circulation distributions for different velocity-normalized radial positions obtained by Prandtl and Goldstein. Prandtl's solution is the dotted line and Goldstein's is the solid curve. The circulation is higher for a larger number of blades.

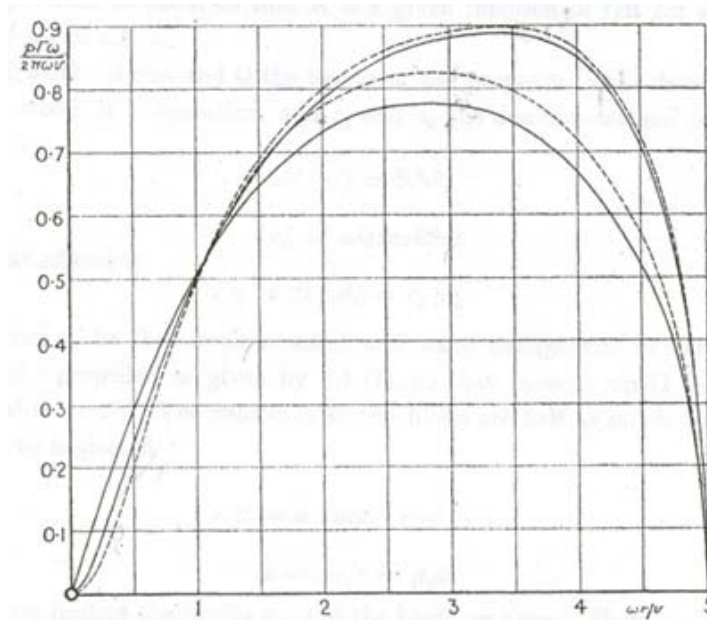


Figure 4.2: Prandtl and Goldstein circulation distributions for a 2 and a 4-bladed propeller. Tip-speed ratio of 5.

4.2 Finite-State Methods: Axial Flow

Results obtained using finite-state methods cannot be shown without the use of previously introduced concepts and techniques applied to the case of a lightly-loaded rotor that is the subject of this research. First of all, the general optimization must be applied to obtain the pressure coefficients that provide an optimum efficient propeller. Some general

concepts have been introduced, but especially important is to find an expression for the figure of merit (or efficiency) that we can apply to all of the cases in axial flow. This general expression will change according to the assumptions for each of the four cases studied in axial flow (actuator disk and tilted lift with a finite or an infinite number of blades).

The results will demonstrate agreement with classical theories so the finite-state methodology can be verified. For this reason, each of the four cases discussed in the previous sections will be studied independently and compared. The finite-state model will be compared to: 1) optimum pressure and inflow distributions given by momentum theory (for an actuator disk with an infinite number of blades), 2) figure of merit and induced power coefficients given by Betz's distribution (for tilted lift and an infinite number of blades), 3) figure of merit and induced power coefficient results given by Prandtl's approximation (for an actuator disk with a finite number of blades), and 4) circulation distribution given by the Prandtl approximation to Goldstein (for the case of tilted lift with a finite number of blades).

4.2.1 Optimization

Given the general quadratic optimization on Section 3.3 we may now apply this approach to the case for minimum induced power that we are presently discussing. For an actuator disk, with infinite number of blades that is lightly loaded, we will minimize C_p for a given C_T .

$$C_p = \sum_{n=1,3,5,\dots} 2\alpha_n^0 \tau_n^{0c} + \sum_{m=1,2,\dots} \sum_{n=m+1,m+3,\dots} \alpha_n^m \tau_n^{mc} = \left\{ \begin{matrix} 2\alpha_n^0 \\ \alpha_n^m \end{matrix} \right\}^T \{\tau\} \quad (4.23)$$

subject to a given C_T .

$$C_T = 2 \left\{ \tau_n^m \right\}^T \left\{ C_n^m \right\} \quad (4.24)$$

Physically, the coefficients C_n^m are a Legendre-function representation of $\nu \cos \varphi$ which is the loss of thrust due to the tilt of the lift vector. The proof that they are in fact a fit is further discussed on Appendix F. They are defined as:

$$C_n^0 = \frac{1}{2\pi} \int_0^{2\pi} \int_0^1 \cos \varphi \bar{P}_n^0(\nu) \nu d\nu d\psi \quad (4.25)$$

$$C_n^{mc} = \frac{1}{\pi} \int_0^{2\pi} \int_0^1 \cos \varphi \bar{P}_n^m(\nu) \nu d\nu \cos(m\psi) d\psi \quad (4.26)$$

$$C_n^{ms} = \frac{1}{\pi} \int_0^{2\pi} \int_0^1 \cos \varphi \bar{P}_n^m(\nu) \nu d\nu \sin(m\psi) d\psi \quad (4.27)$$

where

$$\cos \varphi = \frac{r + \mu \sin \psi}{\sqrt{(r + \mu \sin \psi)^2 + \lambda^2}} \quad (4.28)$$

for a lightly-loaded rotor.

Then, the relationship between the coefficients and the function $\cos \varphi$ (cosine of the tilt angle) becomes:

$$\nu \cos \varphi = \sum_n C_n^0 \bar{P}_n^0(\nu) + \sum_{m,n} \bar{P}_n^m(\nu) \left[C_n^{mc} \cos(m\psi) + C_n^{ms} \sin(m\psi) \right] \quad (4.29)$$

Notice that, for axial flow, the advance ratio (μ) is zero. For an ideal actuator disk, the non-dimensional climb rate (λ) is arbitrarily small, whereas for tilted lift it will have a finite value.

From He's inflow Equations (3.9) and (3.10) for an infinite number of blades, this is a steady system. Furthermore, all the coefficients associated with the sine component are zero, that is, β_n^m and τ_n^{ms} are zero. Rearranging the equation with this in mind, it can be solved in matrix form for the induced velocity coefficients, as expressed by:

$$V [\tilde{L}^c]^{-1} \{\alpha_n^m\} = \frac{1}{2} \{\tau_n^{mc}\} \quad (4.30)$$

$$\{\alpha_n^m\} = \frac{1}{2V} [\tilde{L}_{nj}^{mr}] \{\tau_j^r\} \quad (4.31)$$

$$\begin{Bmatrix} 2\alpha_n^0 \\ \alpha_n^m \end{Bmatrix} = \frac{1}{2V} [\bar{\bar{L}}_{nj}^{mr}] \{\tau_j^r\} \quad (4.32)$$

$$C_P = \frac{1}{2V} \{\tau_j^r\}^T [\bar{\bar{L}}_{nj}^{mr}] \{\tau_j^r\} \quad (4.33)$$

Let the matrix \tilde{L} with the $m = 0$ row partition multiplied by two will be called $\bar{\bar{L}}$. Then, the minimum induced power problem can be formulated as the optimization of a functional J , shown below, subject to the constraint expressed by equation (4.24). The optimization is carried out in to yield the optimum value for the pressure coefficients.

$$J = \frac{1}{2} \frac{1}{V} \{\tau_n^m\}^T [\bar{\bar{L}}_{nj}^{mr}] \{\tau_j^r\} - \frac{1}{2} \Lambda C_T \quad (4.34)$$

subject to the condition

$$2\{\tau_n^m\}^T \{C_n^m\} = C_T \quad (4.35)$$

This leads to

$$\delta \left[\frac{1}{2} \frac{1}{V} \{\tau_n^m\}^T \left[\bar{\bar{L}}_{nj}^{mr} \right] \{\tau_j^r\} - \Lambda \{\tau_n^m\}^T \{C_n^m\} \right] = 0 \quad (4.36)$$

$$\frac{1}{2} \frac{1}{V} \{\delta \tau_n^m\}^T \left[\bar{\bar{L}}_{nj}^{mr} \right] \{\tau_j^r\} + \frac{1}{2} \frac{1}{V} \{\tau_n^m\}^T \left[\bar{\bar{L}}_{nj}^{mr} \right] \{\delta \tau_j^r\} - \Lambda \{\delta \tau_n^m\}^T \{C_n^m\} = 0 \quad (4.37)$$

$$\frac{1}{V} \left[\frac{1}{2} \left[\bar{\bar{L}}_{nj}^{rm} \right] + \frac{1}{2} \left[\bar{\bar{L}}_{nj}^{rm} \right]^T \right] \{\tau_n^m\} = \{C_n^m\} \Lambda \quad (4.38)$$

$$\{\tau_n^m\}_{optimal} = V \left[\frac{1}{2} \left[\bar{\bar{L}}_{nj}^{rm} \right] + \frac{1}{2} \left[\bar{\bar{L}}_{nj}^{rm} \right]^T \right]^{-1} \{C_n^m\} \Lambda = V \left[\bar{\bar{L}}_s \right]^{-1} \{C_n^m\} \Lambda \quad (4.39)$$

where Λ is chosen to match the desired C_T in Equation (4.35).

Equation (4.39) is the solution for this optimization problem, which will yield the minimum induced power for a lightly loaded actuator disk with infinite number of blades.

In these equations Λ is the Lagrange multiplier, that is chosen to give: $\tau_1^0 = (\sqrt{3}/2) C_T$.

4.2.2 Figure of Merit

The general solution for the pressure coefficients given in Section 4.2.1 can be applied to different cases. It is the purpose of this section to show results for axial flow, but these coefficients can be also used to obtain pressure, circulation and inflow velocity for a variety

of flows, including edgewise flow ($\chi = 90^\circ$). For axial flow, $\chi = 0^\circ$, the elements in $\bar{\bar{L}}$ are zero except when $r = m$.

For an infinite number of blades, the equations of motion reduce to

$$V[\tilde{L}]^{-1}\{\alpha_n^m\} = \frac{1}{2}\{\tau_n^m\} \quad (4.40)$$

The pressure and induced velocity coefficients can then be obtained and introduced into the equation for the power and thrust coefficients.

$$\{\tau_n^m\} = 2V[\tilde{L}]^{-1}\{\alpha_n^m\} \quad (4.41)$$

$$\{\alpha_n^m\} = \frac{1}{2V}[\tilde{L}]\{\tau_n^m\} \quad (4.42)$$

The power coefficient becomes

$$C_P = \begin{Bmatrix} 2\alpha_n^0 \\ \alpha_n^m \end{Bmatrix}^T \{\tau_n^m\} = \{\tau_n^m\}^T \begin{Bmatrix} 2\alpha_n^0 \\ \alpha_n^m \end{Bmatrix} \quad (4.43)$$

For this optimization, we find the power subject to a thrust constrained, expressed in Equation (4.44).

$$C_T = 2\{\tau_n^m\}^T \{C_n^m\} \quad (4.44)$$

Introducing the induced velocity coefficients in Equation (4.45) into the equation for the power (Equation (4.43)) provides the power to minimize.

$$\begin{Bmatrix} 2\alpha_n^0 \\ \alpha_n^m \end{Bmatrix} = \frac{1}{2V}[\bar{\bar{L}}]\{\tau_n^m\} \quad (4.45)$$

$$C_P = \frac{1}{2V} \{\tau_n^m\}^T \left[\bar{\bar{L}} \right] \{\tau_n^m\} = \frac{1}{2V} \{\tau_n^m\}^T \left[\bar{\bar{L}}_s \right] \{\tau_n^m\} \quad (4.46)$$

For minimum power, without the tilt on the lift, the optimum pressure and influence coefficients are $C_1^0 = 1/\sqrt{3}$ and $\tau_1^0 = (\sqrt{3}/2)C_T$.

The functional for the optimization becomes

$$J = \frac{1}{2V} \{\tau_n^m\}^T \left[\bar{\bar{L}}_s \right] \{\tau_n^m\} - \Lambda \{\tau_n^m\}^T \{C_n^m\} \quad (4.47)$$

Performing the optimization ($dJ = 0$) the distribution that provides optimum power is

$$\{\tau_n^m\} = V \left[\bar{\bar{L}}_s \right]^{-1} \{C_n^m\} \Lambda \quad (4.48)$$

For the case of no tilt, $\tau_1^0 = (\sqrt{3}/2)C_T = V \left[\bar{\bar{L}}_s \right]_{11}^{-1} (1/\sqrt{3}) \Lambda$. The first value of the influence coefficient matrix obtained using the closed-form expressions in Appendix D is

$$\left[\bar{\bar{L}}_s \right]_{11} = 3/2 \text{ and } \left[\bar{\bar{L}}_s \right]_{11}^{-1} = 2/3.$$

The power coefficient and the Lagrange multiplier are

$$C_T = 2V \{C_n^m\}^T \left[\bar{\bar{L}}_s \right]^{-1} \{C_n^m\} \Lambda \quad (4.49)$$

$$\Lambda = \frac{C_T/2V}{\{C_n^m\}^T \left[\bar{\bar{L}}_s \right]^{-1} \{C_n^m\}} \quad (4.50)$$

Introducing Eqs. (4.49) and (4.50) into the equation for the power coefficient yields the optimum power coefficient in Equation (4.51).

$$C_p = \frac{1}{2V} \Lambda^2 V^2 \{C_n^m\}^T [\bar{\bar{L}}_s]^{-1} [\bar{\bar{L}}_s] [\bar{\bar{L}}_s]^{-1} \{C_n^m\} = \frac{V^2 \left(\frac{C_T}{2V}\right)^2}{\left[\{C_n^m\}^T [\bar{\bar{L}}_s]^{-1} \{C_n^m\}\right]^2} \frac{\{C_n^m\}^T [\bar{\bar{L}}_s]^{-1} \{C_n^m\}}{\left[\{C_n^m\}^T [\bar{\bar{L}}_s]^{-1} \{C_n^m\}\right]^2} \quad (4.51)$$

Multiplying, the final form of the optimum power coefficient is

$$C_p = \frac{C_T^2}{8V} \left[\{C_n^m\}^T [\bar{\bar{L}}_s]^{-1} \{C_n^m\} \right]^{-1} \quad (4.52)$$

Applying the same concepts to the case of axial flow with no tilt on the lift, where

$\{C_n^m\} = \{1/\sqrt{3} \quad 0 \quad 0 \quad \dots\}^T$ the minimum power coefficient is obtained.

$$C_{p \min} = \frac{C_T^2}{8V} \left[\frac{1}{\sqrt{3}} [\bar{\bar{L}}_s]_{11}^{-1} \frac{1}{\sqrt{3}} \right]^{-1} = \frac{C_T^2}{2V} \quad (4.53)$$

Introducing these power coefficients into the definition of figure of merit demonstrates the steps taken to come to the final expression used throughout this dissertation.

$$FM = \frac{C_{p \min}}{C_p} = 4 \{C_n^m\}^T [\bar{\bar{L}}_s]^{-1} \{C_n^m\} \quad (4.54)$$

4.2.3 Infinite Number of Blades

For the case of an actuator disk, Equation (4.28) reduces to the unity ($\lambda = 0$) and the coefficients in equations (4.25) through (4.27) reduce to:

$$C_1^0 = \int_0^1 \sqrt{3} v^2 dv = \frac{1}{\sqrt{3}}$$

and all the others become:

$$C_n^m = 0$$

Therefore, the vector $\{C_n^m\}$ is the vector $\{1/\sqrt{3} \ 0 \ 0 \ \dots \ 0\}^T$ with as many elements as the number of terms that correspond to the harmonics studied in the problem

Momentum theory predicts that the minimum induced power for an actuator disk in axial flow will be achieved by constant pressure and constant inflow distributions. Results using the finite-state method show agreement with these predictions. Figures 4.3 and 4.4 show the constant profile for the pressure and the inflow respectively with a reduced amount of terms in the Fourier series. According to blade-element theory, the lift distribution corresponding to this pressure and velocity should be linear. Finite-state methods agree with the predicted results, as it is shown in Figure 4.5.

Figures 4.6 through 4.17 show the pressure and induced velocity distributions for all azimuthal locations on the rotor for increasing values of climb and a thrust coefficient of 1.0. The pressure and induced velocity for axial flow and the case for no tilt ($\nu=0$) are constant for all angles around the rotor, as predicted from classical theories. For this case only (of no climb) the rotor is in hover, therefore the assumption that it is lightly-loaded no longer holds. Both pressure and velocity are directly related, therefore it is predicted that they behave similarly for increasing values of the tilt. It is seen that an adverse inflow region appears at the center of the rotor and that this region augments with increasing tilt. As the

pressure and inflow drop the figure of merit decreases (i.e., the efficiency). This decreased efficiency will be studied more in detail when discussing the forward flight results.

One way to make sure that the theory in fact provides results that were expected, apart from the fact that for the simplest case both pressure and inflow are constant, is to see how the curvature of the distributions at the center of the rotor behaves. As the depressed region at the root increases, previous theories predict that the pressure and inflow should increase, close to the root, as $\mu/\sqrt{1+\mu^2}$. Plots for any individual azimuthal location and a given tilt show that these results follow the predicted shape (See Refs. [19] and [10]).

Of importance is to notice, in all of these figures, that the air is coming into the rotor at an angle. The rotor advancing side is where $r\cos\psi = -1$. Therefore the aft, where $\psi = 0$ corresponds with $r\cos\psi = 1$. There is a symmetry for axial flow, but this symmetry will no longer hold for skewed flow and therefore the direction to which the rotor is advancing will become important.

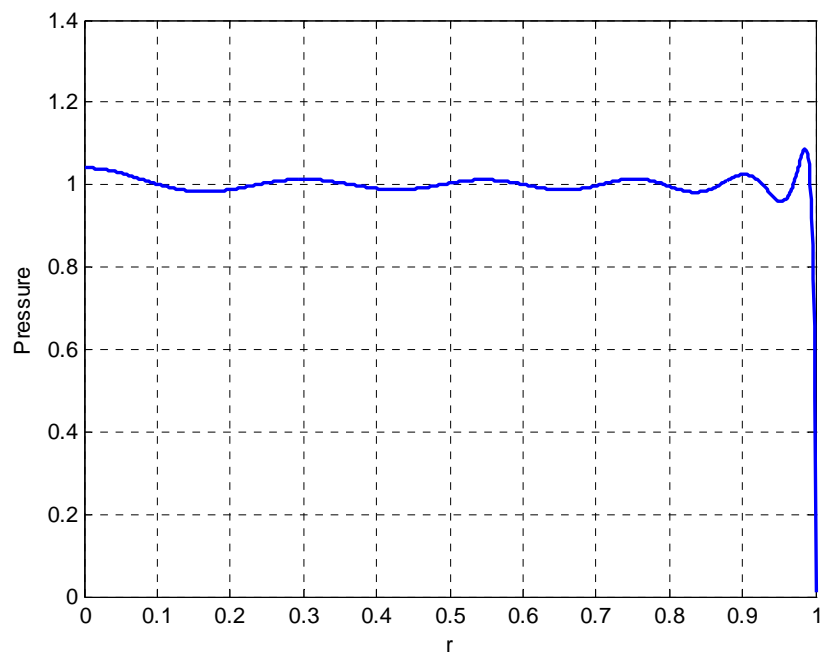


Figure 4.3: Pressure profile that provides minimum induced power for an actuator disk in axial flow with an infinite number of blades.

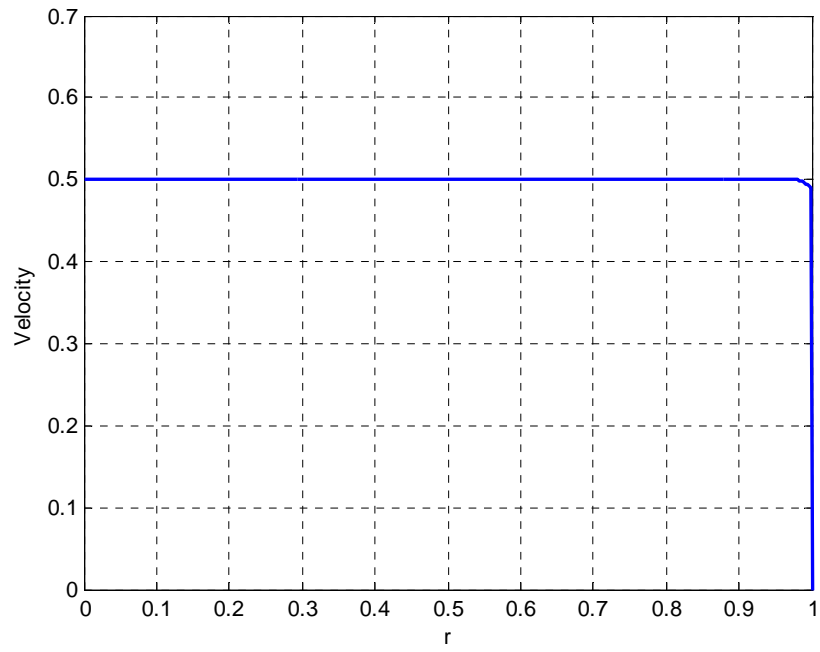


Figure 4.4: Velocity profile that provides minimum induced power for an actuator disk in axial flow with an infinite number of blades.

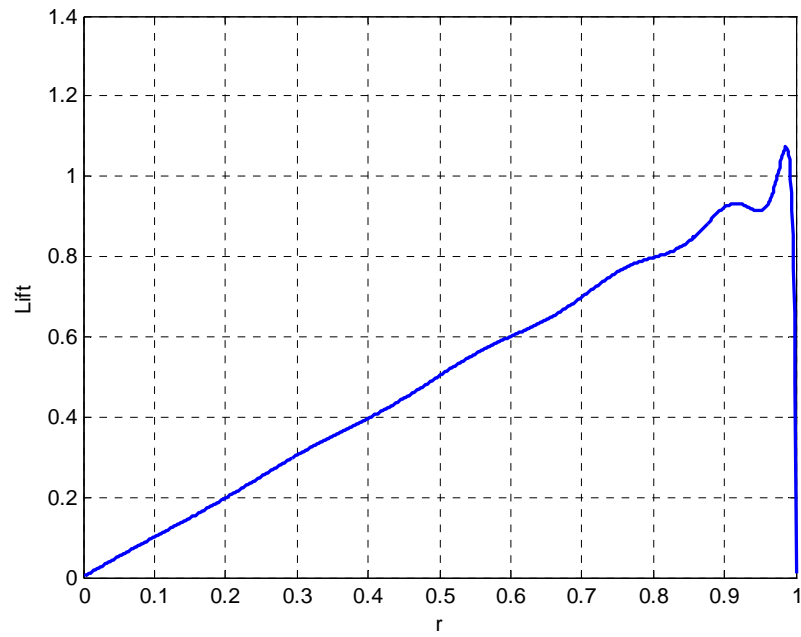


Figure 4.5: Lift distribution for optimum flow for an actuator disk with an infinite number of blades.

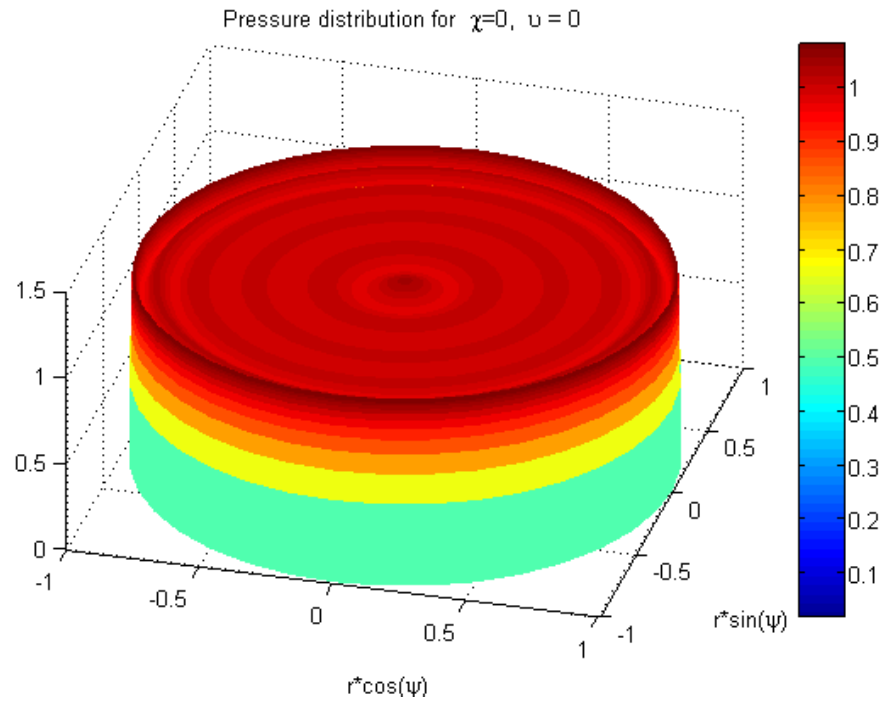


Figure 4.6: Pressure Distribution, $\chi = 0, \nu = 0.0$, FM=1.0.

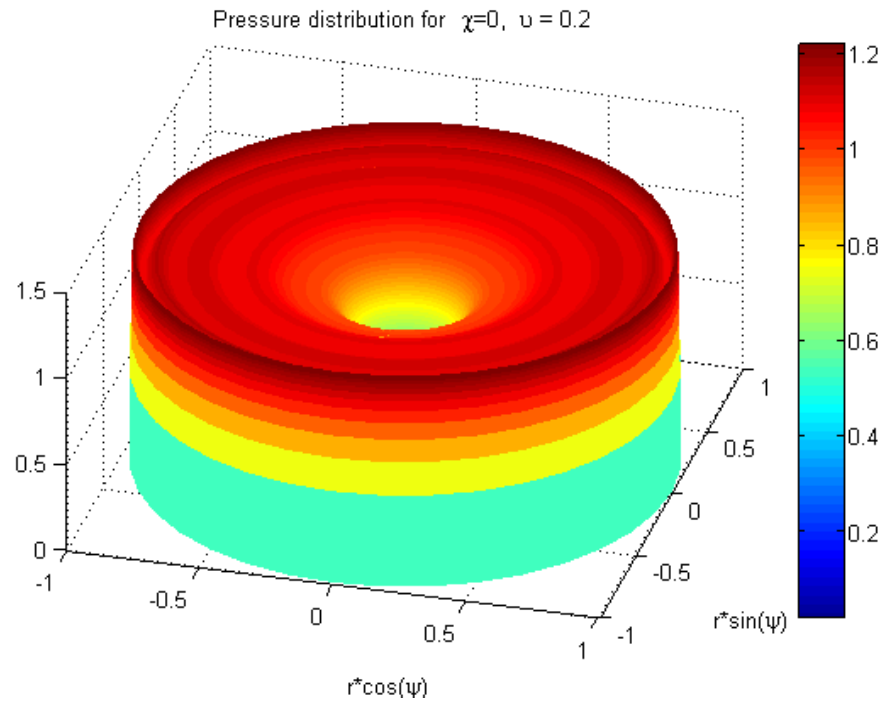


Figure 4.7: Pressure Distribution, $\chi = 0, \nu = 0.2$, FM=0.87.

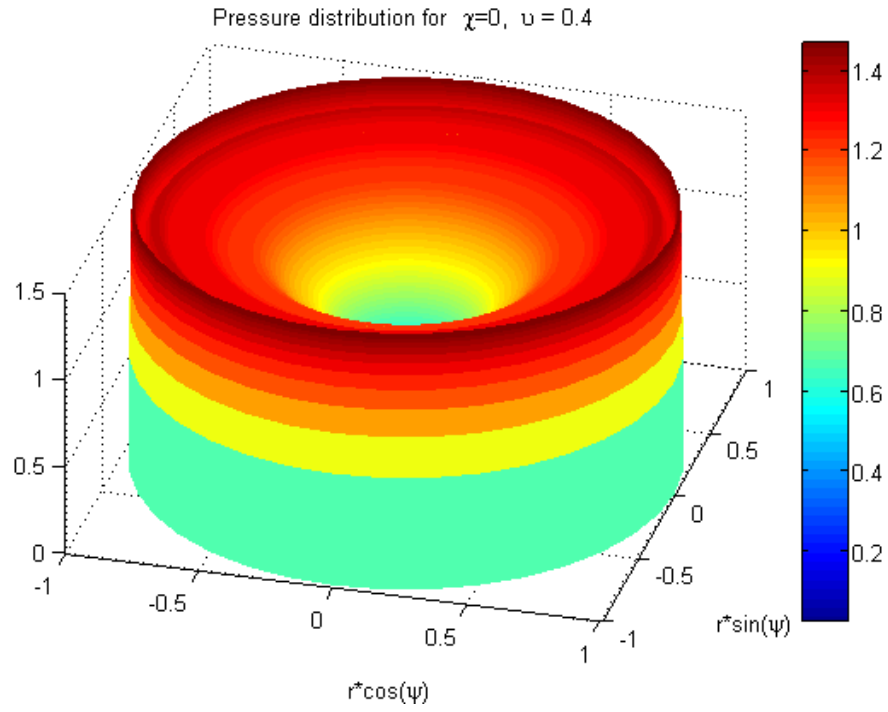


Figure 4.8: Pressure Distribution, $\chi = 0$, $\nu = 0.4$, FM=0.69.

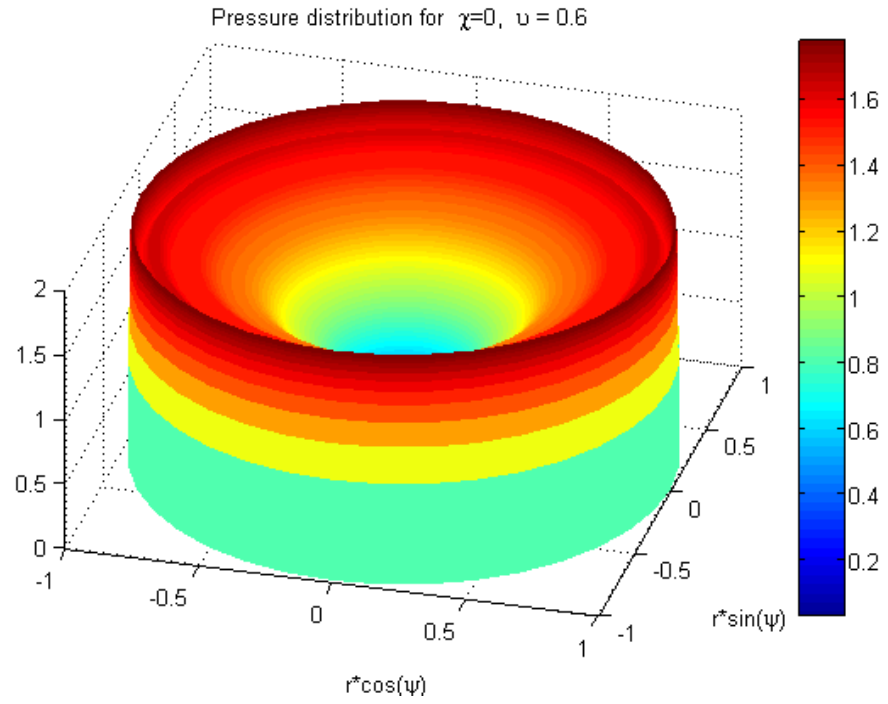


Figure 4.9: Pressure Distribution, $\chi = 0$, $\nu = 0.6$, FM=0.52.

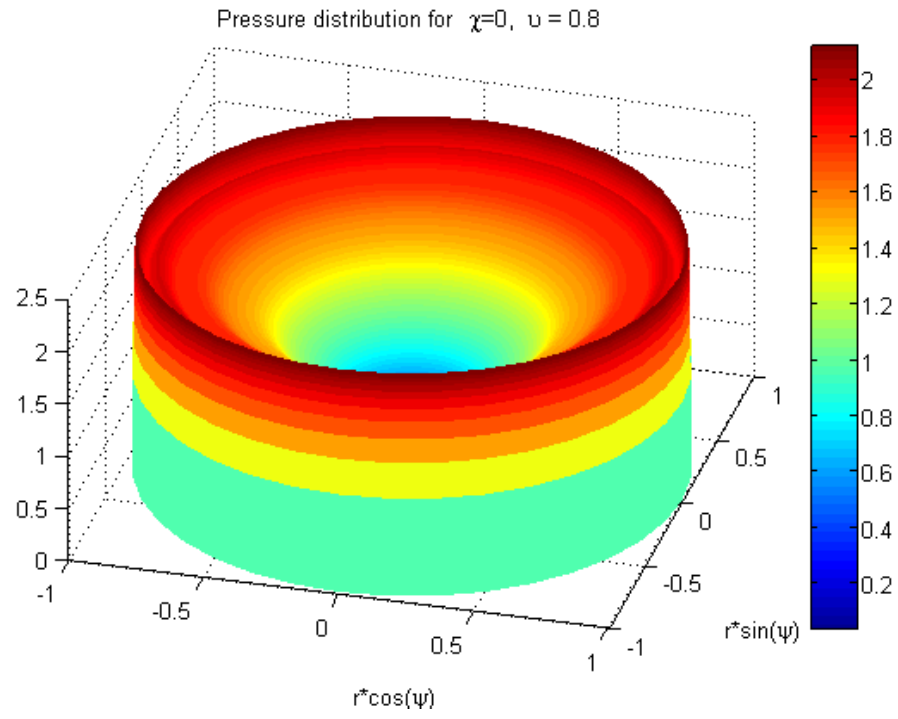


Figure 4.10: Pressure Distribution, $\chi = 0$, $\nu = 0.8$, FM=0.40.

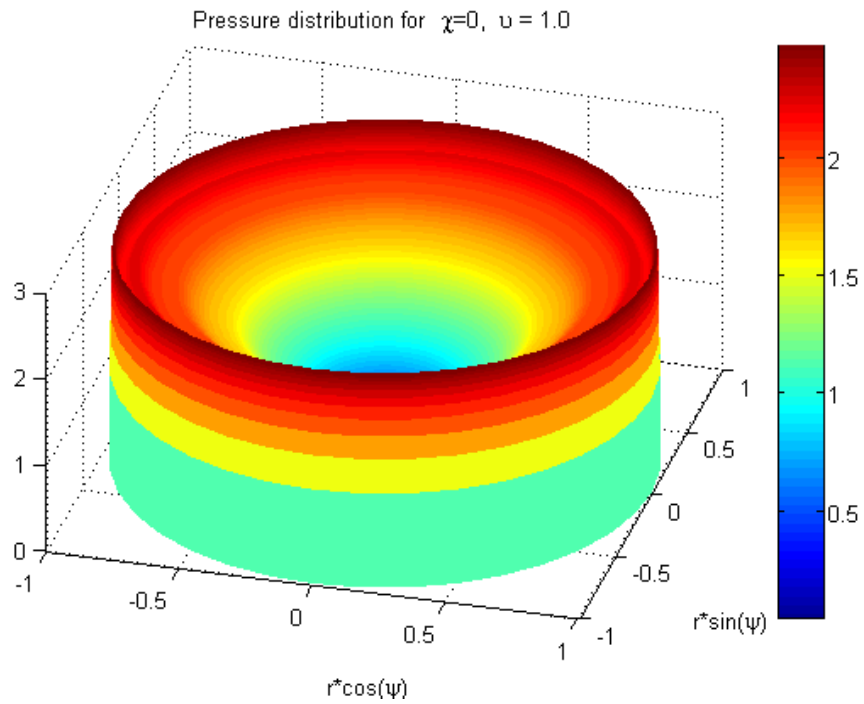


Figure 4.11: Pressure Distribution, $\chi = 0$, $\nu = 1.0$, FM=0.31.

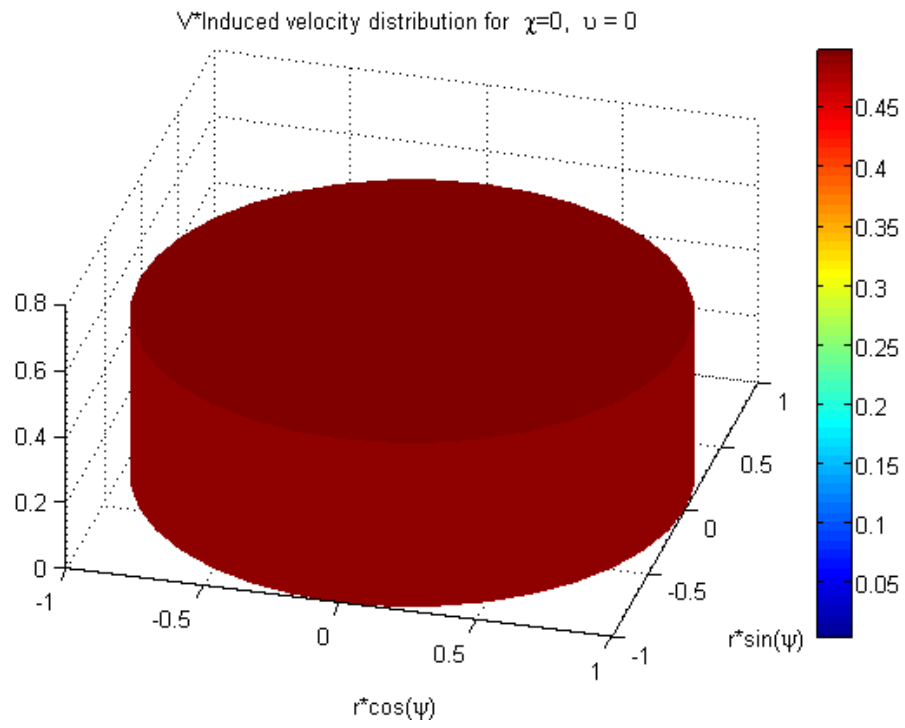


Figure 4.12: Induced Velocity Distribution, $\chi = 0$, $\nu = 0.0$, FM=1.0.

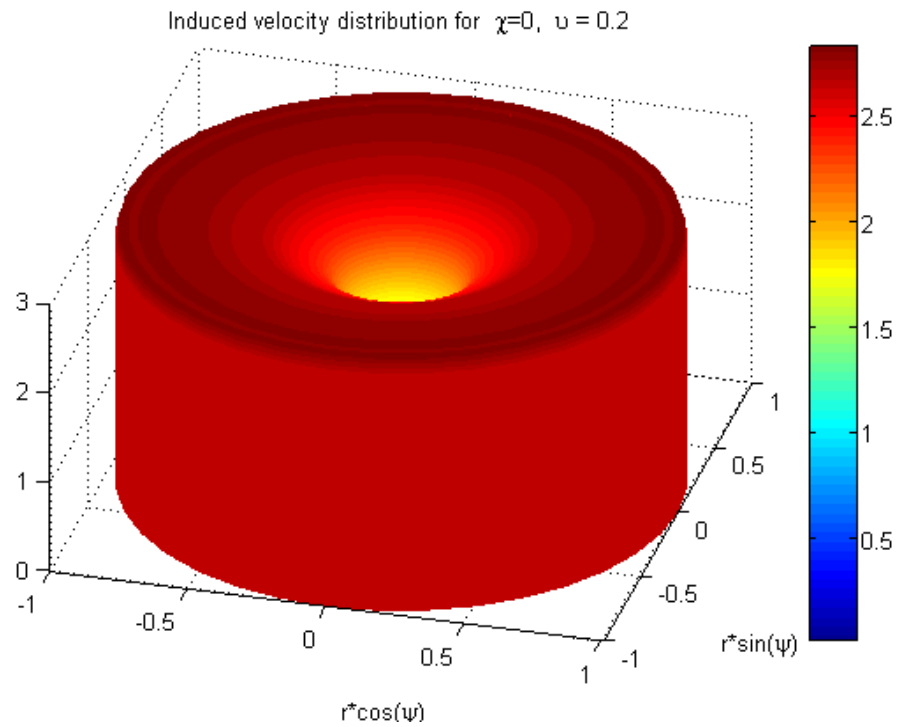


Figure 4.13: Induced Velocity Distribution, $\chi = 0$, $\nu = 0.2$, FM=0.81.

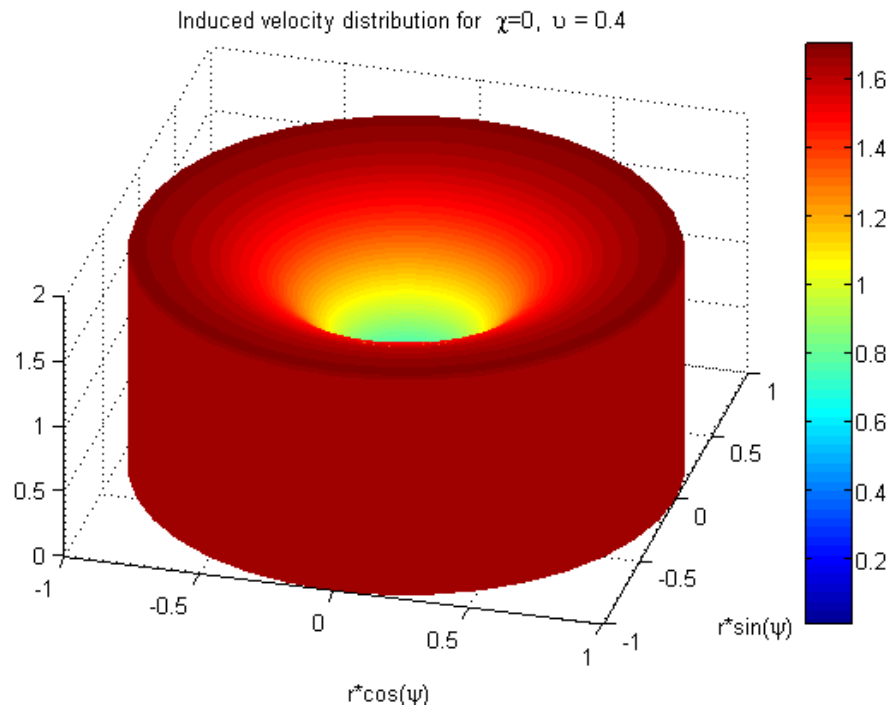


Figure 4.14: Induced Velocity Distribution, $\chi = 0$, $\nu = 0.4$, FM=0.69.

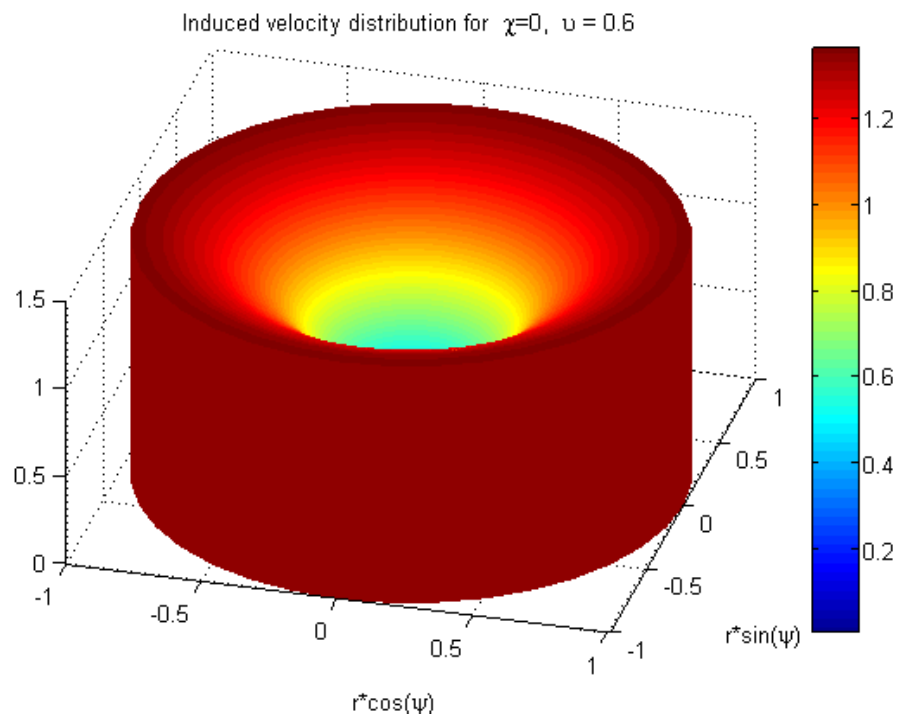


Figure 4.15: Induced Velocity Distribution, $\chi = 0$, $\nu = 0.6$, FM=0.52.

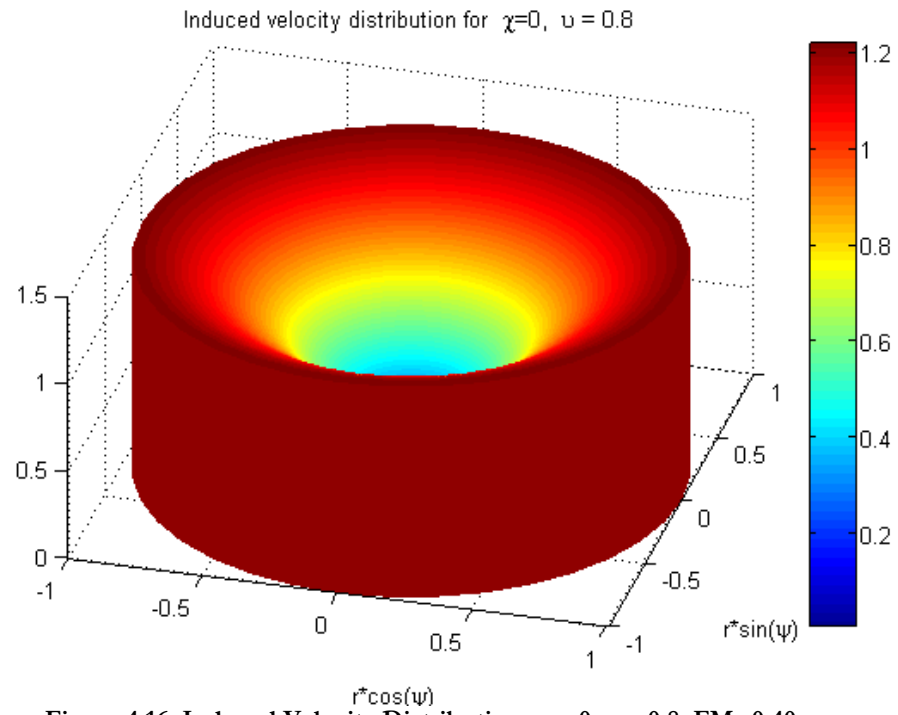


Figure 4.16: Induced Velocity Distribution, $\chi = 0$, $\nu = 0.8$, FM=0.40.

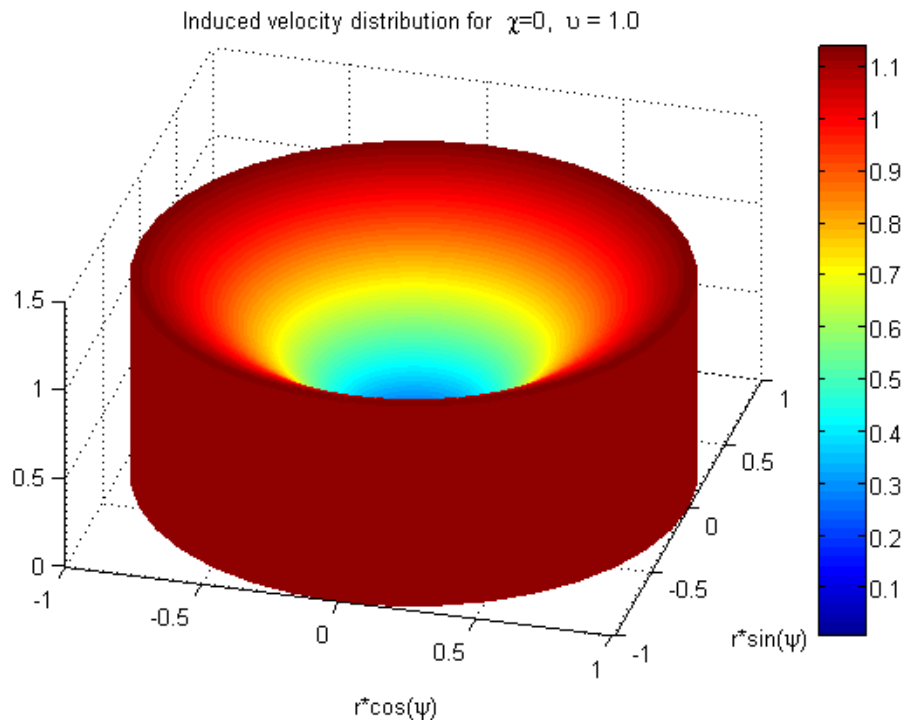


Figure 4.17: Induced Velocity Distribution, $\chi = 0$, $\nu = 1.0$, FM=0.31.

Since the above shows that a formal optimization with the dynamic wake model gives the Glauert result for minimum power, it seems that it would be useful to consider some closed-form results under the Glauert hypothesis. From momentum theory one can show that

$$C_T = 2(\eta + \nu)\nu \quad (4.55)$$

$$C_p = 2(\eta + \nu)^2 \nu = (\eta + \nu)C_T \quad (4.56)$$

Because we optimize for a given C_T , it is very convenient to normalize all velocities on induced flow in hover. Thus, $\bar{\eta} = \eta / \sqrt{C_T / 2}$, $\bar{\nu} = \nu / \sqrt{C_T / 2}$, $\bar{\lambda} = \bar{\eta} + \bar{\nu}$. It follows that the proper normalization of induced power is

$$\bar{C}_p = \frac{\sqrt{2}C_p}{C_T^{3/2}} \quad (4.57)$$

The result is a normalized set of inflow equations. The thrust equation becomes:

$$1 = (\bar{\eta} + \bar{\nu})\bar{\nu} \quad (4.58)$$

which can be solved for normalized or flow due to a normalized climb rate. That value can then be used to determine the normalized induced power for an ideal actuator-disk rotor.

$$\bar{C}_{p_i} = \bar{C}_p - \bar{\eta} = \left[\frac{\bar{\eta}}{2} + \left(\frac{\bar{\eta}^2}{4} + 1 \right)^{1/2} \right]^{-1} \quad (4.59)$$

The ideal induced power ranges from a normalized value of unity in hover ($\bar{\eta} = 0$) and then decreases with climb rate as $1/\bar{\eta}$. This is the Glauert result. We will use this ideal value to compare minimum power settings for various rotors. We will define a generalized figure of merit which is the ideal power, equation (4.33), divided by the actual induced power.

The question remains if the use of finite-state methods will suffice to obtain the Betz distribution for a lifting rotor with an infinite number of blades. To verify this, the figure of merit is found by finite-state methods using the formulation described in the optimization section. These coefficients represent the general solution. To customize them to the present special case, some modifications were performed. Since the present cases are for axial flow, the matrix $\left[\bar{\bar{L}}\right]$ — defined by equation (3.12) — simplifies to a diagonal in terms of Γ_{jn}^{mmm} . It should be noted that these matrices are identical to $\left[A_{jn}^m\right]$ in Ref. 4. The closed form expression for the matrix can be seen in Appendix D. For an infinite number of blades in axial flow, $C_n^m = 0$ except when $m = 0$ so that only A_{jn}^0 enters the optimization. C_n^0 comes from the following integral over the wake skew angle,

$$C_n^0 = \frac{1}{2\pi} \int_0^{2\pi} \int_0^1 \cos \varphi \bar{P}_n^0(v) v dv d\psi$$

where $\cos \varphi = \frac{r}{\sqrt{r^2 + \lambda^2}}$ and $rdr = -v dv$. With these influence coefficients the thrust and power coefficients become:

$$C_T = 2 \sum_{n=1,3,5,\dots} C_n \tau_n^{0c} \quad (4.60)$$

$$C_P = \eta C_T + \sum_{n=1,3,5,\dots} 2\alpha_n^0 \tau_n^{0c} \quad (4.61)$$

For this optimization, again the power coefficient is minimized for constant thrust, and the functional J becomes:

$$J = \eta C_T + \sum_{n=1,3,5,\dots} \frac{1}{2V} \left\{ \tau_n^{0c} \right\}^T \left[A_{nj}^0 \right] \left\{ \tau_j^{0c} \right\} - \Lambda \sum_{n=1,3,5,\dots} C_n \tau_n^{0c} \quad (4.62)$$

where Λ is the Lagrange multiplier. Performing the optimization ($\delta J = 0$), the optimal pressure coefficients for this particular case are:

$$\{\tau_j^0\}_{optimal} = [A_{nj}^0]^{-1} \{C_n\} \Lambda V \quad (4.63)$$

Introducing the above changes to the general optimization formulation, the figure of merit using finite-state methods is:

$$F.M._{finite-state} = 2 \{C_n\}^T [A_{nj}^0]^{-1} \{C_n\} \quad (4.64)$$

Figure 4.18 shows the comparison for the figure of merit from the finite-state method as compared to the Betz formula. It is seen that the finite-state method agrees satisfactorily with Betz result. The difference between them can be reduced by addition of more terms to $[A_{nj}^0]$ and $\{C_n\}$. However, the present approximation, which uses twenty terms is thought to be close enough so that the dynamic inflow model is verified.

What is most important about Figure 4.18 is the large drop in figure of merit with climb rate, even for an optimized rotor. The drop is due purely to the effects of tilted lift and swirl velocity. It may well be that the deficiency in rotor efficiency in forward flight is due to a similar phenomenon.

Figure 4.19 gives figure of merit as a function of climb rate η rather than λ . Since λ is determined by the total flow through the rotor, the Figure of Merit thus becomes a function both of climb rate η and thrust coefficient C_T . For larger climb rate, the effect of C_T is diminished.

Figure 4.20 presents the induced power coefficient as a function of climb rate for a range of C_T values

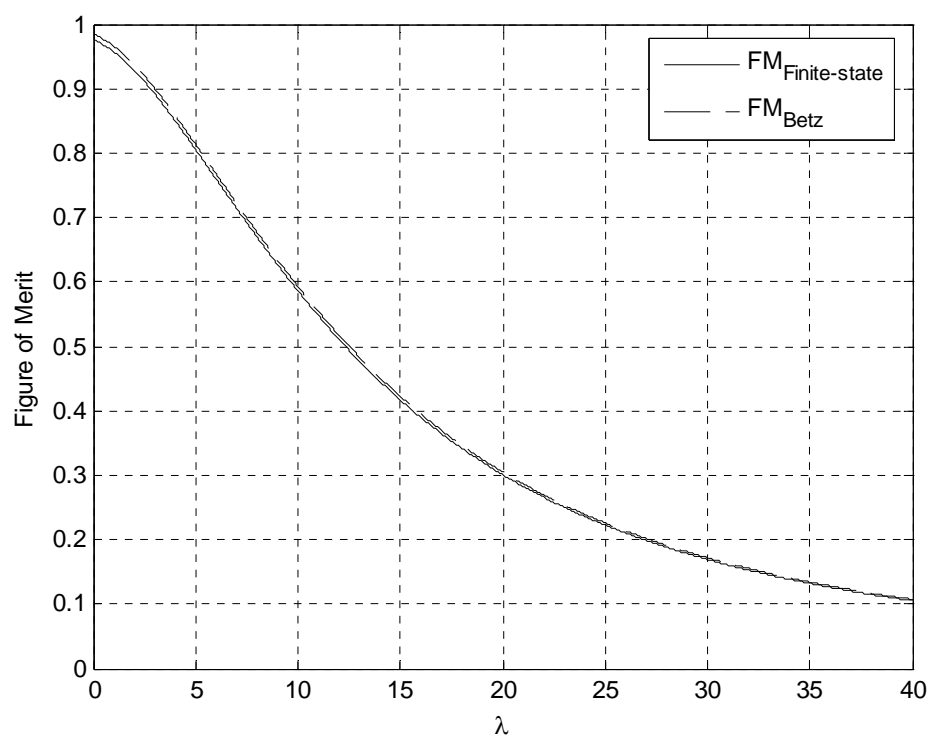


Figure 4.18: Figure of merit comparison of the finite-state optimization to Betz distribution.

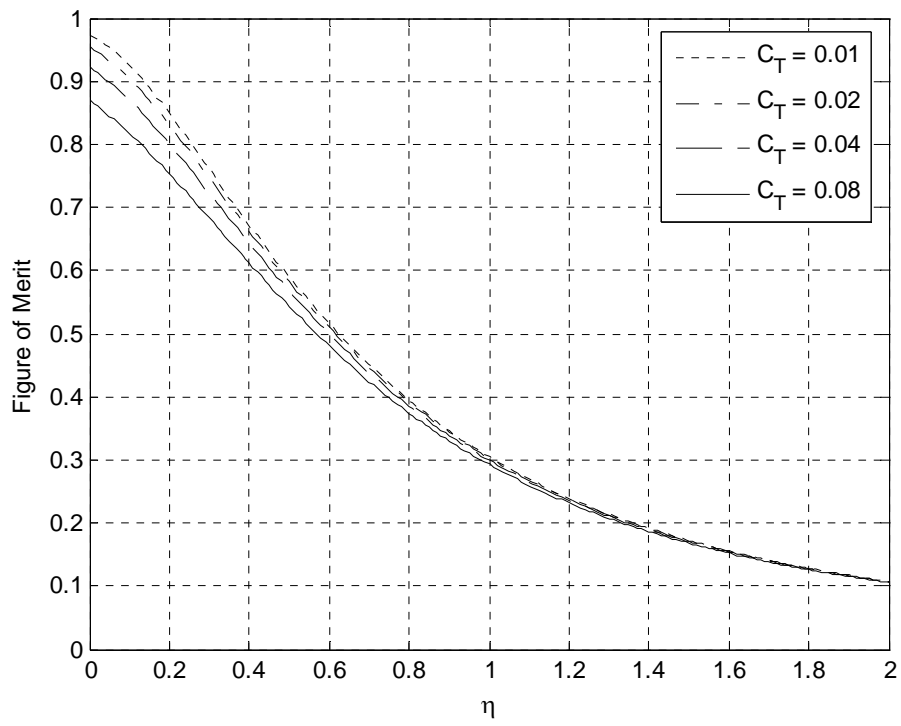


Figure 4.19: Figure of merit versus climb rate for different thrust coefficients (infinite number of blades).

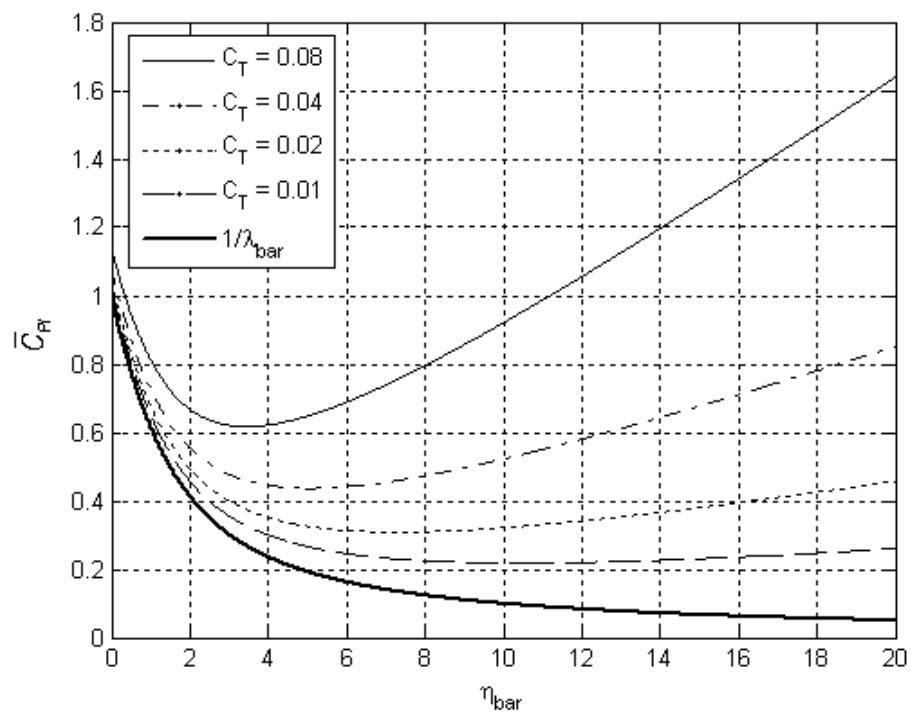


Figure 4.20: Induced power coefficient (helicopter convention) versus climb rate (infinite number of blades)

An important characteristic seen in Figure 4.20 is a “bucket” in the induced power for each thrust coefficient at a given climb rate. This is due to the fact that ideal power decreases with η whereas the figure of merit also decreases with η . Thus, there is an optimum climb rate. The lowest curve is for $C_T = 0$ and is equal to $1/\lambda_{\text{bar}}$. This ideal minimum power monotonically decreases with $\bar{\eta}$, so the “bucket” is not present, and the induced power coefficient does not increase for high climb rates.

4.2.4 Finite Number of Blades

Because the Prandtl correction as applied to the Betz distribution agrees so closely with Goldstein, that it makes sense to do some calculations with the Prandtl factor to determine the magnitude of the effect of number of blades on figure of merit. Thus, equation (4.12) can be used for the figure of merit computations.

Figure 4.21 shows the effect of tip loss (as determined from Prandtl’s k -factor) on figure of merit. The top curve, for the case $\varphi = 0$, is the effect for an actuator disk with a finite number of blades for a four-bladed, lightly loaded rotor. The middle two, coincident curves are the figure of merit for a rotor with tilted lift but infinite number of blades. The lowest curve is for tilted lift and finite number of blades (i.e., the Goldstein solution). One can see that blade number is also an important factor in the loss of ideal induced power.

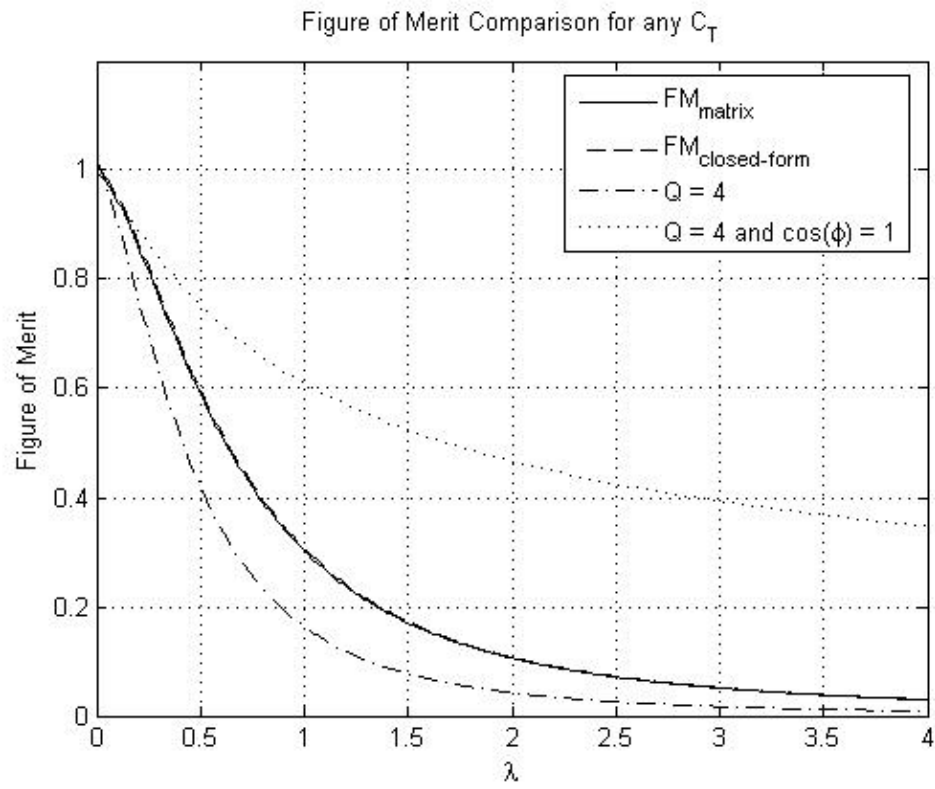


Figure 4.21: Effect of tip loss on figure of merit, lightly-loaded rotor.

We now wish to see if the finite-state methodology can give the correct optimum distribution and figure of merit as Goldstein (i.e., as the Prandtl-corrected Betz). Makinen showed that the inflow model can indeed match Goldstein provided that a correction is applied for the swirl kinetic energy. Thus, the added energy is added to the mass matrix; and the resultant induced flow is assumed parallel to the tilted lift vectors.

To be precise, the apparent mass matrix $[K_n^m]$ (diagonal), must be replaced to include the effect of the wake swirl. There are different swirl corrections that can be applied, but from Ref. 10 the following correction gives the best results.

$$[K_n^m] \Rightarrow [\sqrt{K_n^m}] \left[[I] + m \left(\frac{\kappa \lambda}{Q} \right)^2 \left[[I] - [A_{nj}^m]^2 \right]^{-m} \right] [\sqrt{K_n^m}] \quad (4.65)$$

where $\kappa = 2.2$, Q is the number of blades, and λ is the total inflow. It should be noted that for an actuator disk (no lift tilt), κ is set to zero.

Performing the optimization for this case, and using finite-state methods, the figure of merit is obtained. The vector $\{C_n^m\}$ remains the same as for an infinite number of blades. There is no change in the values because physically these coefficients are a fit of the function $v \cos \varphi$, and for an actuator disk $\cos \varphi = 1$.

$$F.M._{finite-state} = 2 \{C_n^m\}^T [\tilde{L}]^{-1} \{C_n^m\} \quad (4.66)$$

Once the theory has been verified, some useful plots of induced power for different numbers of blades at various climb rates can be obtained, as it is shown in Figure 4.22. The

importance of this graph is that the effect of finite number of blades on the induced power can be noticed. It is seen that induced power increases for a decreasing number of blades. It is an expected result, as the ideal induced power exists for an infinite number of blades (for Prandtl is $k = 1$). The profile of the curves is similar to the one observed for infinite numbers of blades at different thrust coefficients. The “bucket” effect is present here also, and the general profile is maintained. Thus, the effect of these differences for finite number of blades affecting the induced power is as less critical as the increase in induced power due to lift tilt.

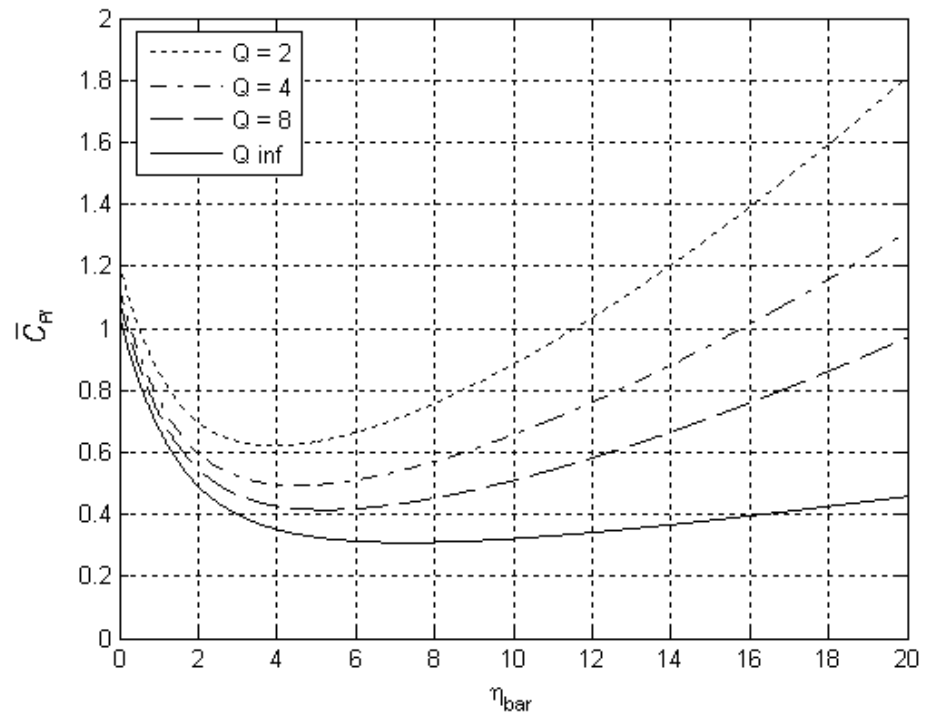


Figure 4.22: Induced power coefficient comparison for various numbers of blades ($C_T = 0.02$).

Finite-State methods should agree with the theory developed by Goldstein [19] for every flight condition in axial flow. There is no closed-form solution or expression that Goldstein developed for the theoretical figure of merit for a lifting rotor with a finite number of blades. However, Makinen [10],[11] was successful in the further development and application of the finite-state method to obtain circulation for a given induced velocity. These circulation results are in agreement with Goldstein's circulation for an optimal propeller, as it is shown in Figures 4.23 and 4.24. The fact that the application of finite-state methods provides an accurate optimal circulation results in the confidence that the calculations of figure of merit for this special case will also be accurate.

Figures 4.23 and 4.24 show the circulation at any radial position of the blade using Prandtl's approximation, Goldstein's optimal circulation, and Makinen's results with the swirl velocity corrections made to the apparent mass matrix in equation (4.48). Figure 4.23 is for a $\mu_0 = 5$ ($\lambda = 0.20$) and Figure 4.24 is for $\mu_0 = 20$ ($\lambda = 0.05$). It is noticed that Prandtl and Goldstein's circulations give results that are very close to each other. Since there is such close agreement in both approaches, and there is a figure of merit expression for Prandtl's approximation, the finite-state approach could be comparable to Prandtl's approximation. It is not surprising that the quadratic optimization with the dynamic wake model gives the correct figure of merit due to both lift tilt and finite number of blades. Figures 4.23 and 4.24 (from Ref. 8) show that the dynamic wake model (with swirl correction) gives the correct inboard (swirl) and outboard (tip loss) velocities.

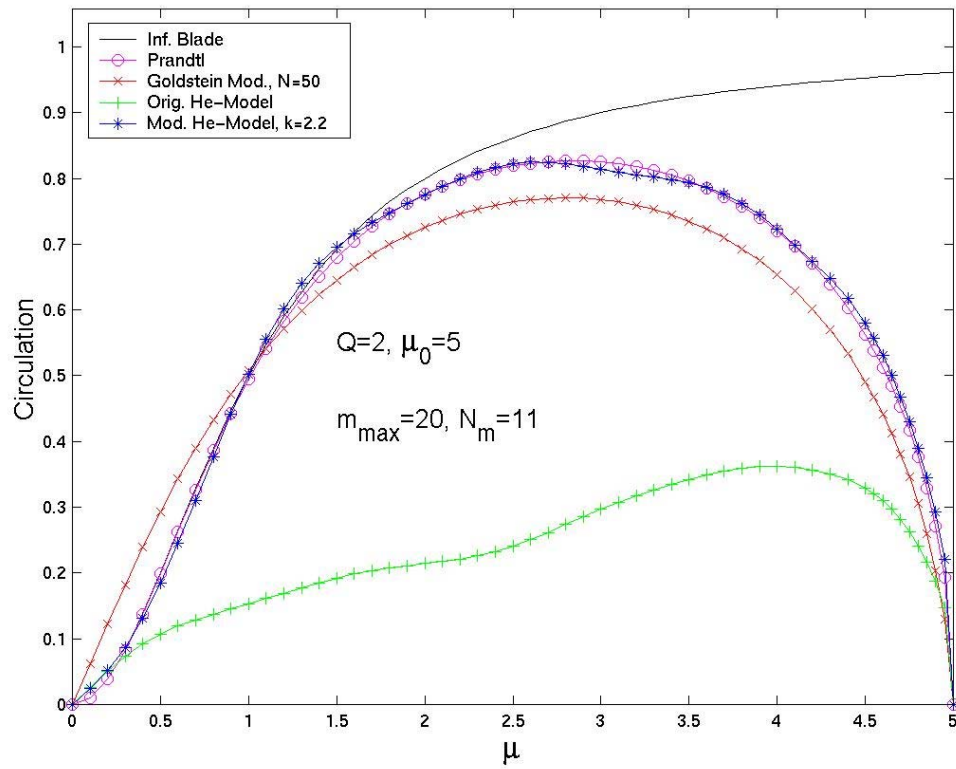


Figure 4.23: Circulation at any blade radial location for Prandtl, Goldstein, and using Finite-State methods. Plot obtained from [10],[11].

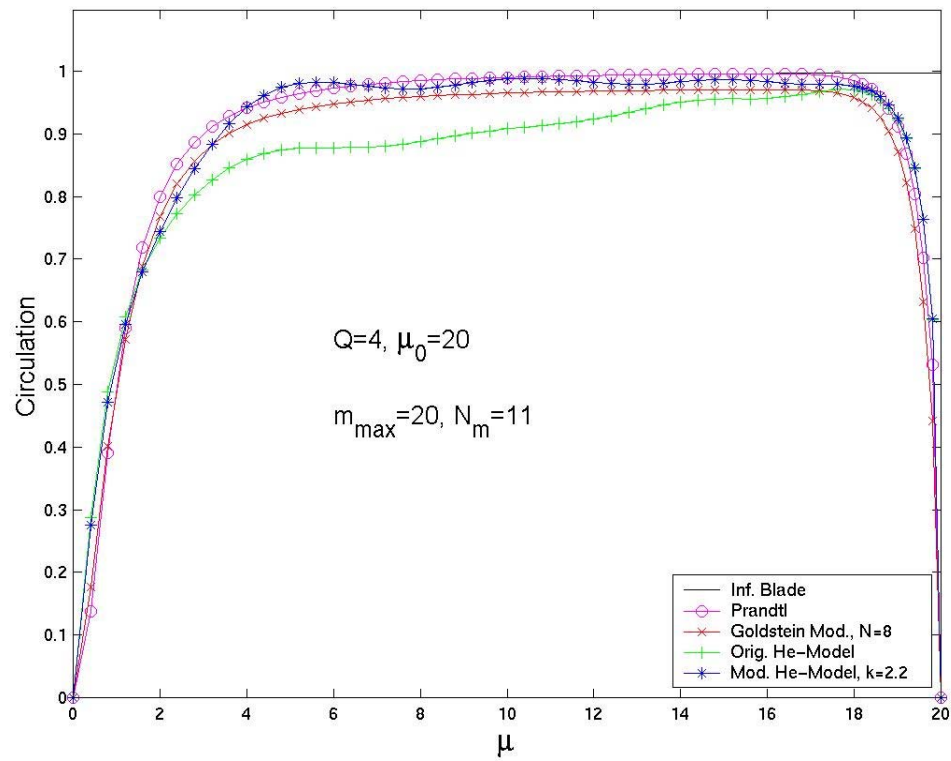


Figure 4.24: Circulation at any blade radial location for Prandtl, Goldstein, and using Finite-State methods. Plot obtained from [10],[11].

4.3 Finite-State Methods: Skewed Flow

Since the method has been validated, the theory can be applied to the same cases for skewed flow. Most of the approach for skewed flow is similar to that for axial flow.

4.3.1. Infinite Number of Blades

The case for an actuator disk with an infinite number of blades will be revisited. However some changes will be done for forward flight. For this case, momentum theory predicts that the optimum induced power is obtained for a constant pressure distribution (similarly as to what happened for axial flow) but the induced velocity profile will no longer be constant. For an actuator disk with an infinite number of blades, we have already applied the finite-state model and verified that it gives the Glauert solution of uniform pressure. However, to go on to the other cases, all harmonics (and their periodic coupling) will need to be included.

The rest of the special cases, for an actuator disk with a finite number of blades and for the two cases for a lifting rotor, will provide results never obtained before. The results will hopefully provide the conclusion as to why the experimental minimum induced power for a helicopter is orders of magnitude greater to what theory predicts should be. These results could allow determining what changes, if any, should be introduced in the rotor to reduce the minimum induced power.

The formulation for the figure of merit in forward flight will remain similar to the general figure of merit shown by equation (4.54):

$$F.M._{finite-state} = 2 \left\{ C_n^m \right\}^T \left[\bar{\bar{L}} \right]^{-1} \left\{ C_n^m \right\}$$

However, the coefficients and the L-matrix will be different than the ones obtained previously, and also different for each of the four cases.

The main difference for skewed flow is that when calculating the cosine of the inflow angle the advance ratio, μ , must be considered. Equation (4.28) again is:

$$\cos \varphi = \frac{r + \mu \sin \psi}{\sqrt{(r + \mu \sin \psi)^2 + \lambda^2}}$$

where r is the radial position along the blade and ψ is the angle at which the rotating blade is with respect to the aft position of the rotor.

For skewed flow, the total inflow also changes. The total inflow for axial flow was defined before as:

$$\bar{\lambda} = \bar{\eta} + \bar{v} = \frac{\bar{\eta}}{2} + \sqrt{\left(\frac{\bar{\eta}}{2}\right)^2 + 1}$$

and it was derived from momentum theory for a uniform induced flow distribution. In forward flight, the total inflow becomes:

$$\bar{\lambda} = \bar{\eta} + \bar{v} \quad (4.67)$$

where the normalized inflow is the solution of equation (4.53) for given normalized climb rate and advance ratio.

$$1 = \bar{v} \sqrt{\bar{\mu}^2 + (\bar{v} + \bar{\eta})^2} \quad (4.68)$$

These changes will affect the optimum coefficients, but the L-matrix will also be altered because the skew angle is no longer zero, and so there are more harmonics than the $m = 0$ for axial flow. The expression for this matrix will be obtained using He's formulation (Eqs. (3.9) and (3.10)).

Different cases have been considered for a rotor with low lift and with the tilt angle defined above. Table 4.1 shows all of the cases, including the axial flow cases shown in Section 4.2.3 (Figures 4.6 through 4.17). The Table provides, for each case the value of the skew angle used, the advance ratio, the total inflow and, based on these parameters, the type of case that the results show. None of the cases considers the swirl correction, because it is small in forward flight. Axial flow solutions (Section 4.2.3) are cases 1 through 7. Case number 1 is for no tilt and cases 2 through 7 are for a climbing actuator disk but a disk that is not traveling forward (i.e., no advance ratio). Cases 7 through 28 are for various conditions in forward flight. Of special attention are cases 8, 15 and 22 that show pure skewed flow, with no tilt or advance. Cases 23 through 28 show skewed flow advancing without climb.

For cases with low lift, the mass flow parameter, V becomes v . The theory developed enables anyone to obtain results for a case with lift just by introducing the modified values that affect the mass flow parameter and the total inflow, λ . The equations used to obtain the values of advance ratio and total inflow for all of the cases in Table 4.1 are shown in Equations (4.69) through (4.72).

$$V = \frac{\mu^2 + (\lambda + \nu)\lambda}{\sqrt{\mu^2 + \lambda^2}} \quad (4.69)$$

$$\alpha = 90^\circ - \chi \quad (4.70)$$

$$\mu = \nu \cos(\alpha) \quad (4.71)$$

$$\lambda = \nu \sin(\alpha) + \nu \quad (4.72)$$

where $\nu = 0$ for low-lift cases, χ is the skew angle and ν is the total inflow.

The cases on Table 4.1 are applied to figure of merit calculations and to obtain pressure and induced velocity distributions for all of the points around the rotor.

Figure 4.25 shows the figure of merit for all skew angles. Figure 4.26 shows the figure of merit change with increasing climb and advance ratio.

Table 4.1: Cases for FM, Pressure and Inflow Figures.

CASE:	ν	χ (DE G)	μ	λ	TYPE:
1	0.0	0	0.0000	0.0000	Actuator disk, axial flow, No tilt
2	0.1	0	0.0000	0.1000	
3	0.2	0	0.0000	0.2000	
4	0.4	0	0.0000	0.4000	
5	0.6	0	0.0000	0.6000	
6	0.8	0	0.0000	0.8000	
7	1.0	0	0.0000	1.0000	
8	0.0	30	0.0000	0.0000	Actuator disk, skewed flow No tilt, no advance
9	0.1	30	0.0500	0.0866	Actuator disk, skewed flow
10	0.2	30	0.1000	0.1732	
11	0.4	30	0.2000	0.3464	
12	0.6	30	0.3000	0.5196	
13	0.8	30	0.4000	0.6928	
14	1.0	30	0.5000	0.8660	
15	0.0	60	0.0000	0.0000	Actuator disk, skewed flow No tilt, no advance
16	0.1	60	0.0866	0.0500	Actuator disk, skewed flow
17	0.2	60	0.1732	0.1000	
18	0.4	60	0.3464	0.2000	
19	0.6	60	0.5196	0.3000	
20	0.8	60	0.6928	0.4000	
21	1.0	60	0.8660	0.5000	
22	0.0	90	0.0000	0.0000	Actuator disk, skewed flow. No tilt, no advance
23	0.1	90	0.1000	0.0000	Actuator disk, skewed flow No tilt
24	0.2	90	0.2000	0.0000	
25	0.4	90	0.4000	0.0000	
26	0.6	90	0.6000	0.0000	
27	0.8	90	0.8000	0.0000	
28	1.0	90	1.0000	0.0000	

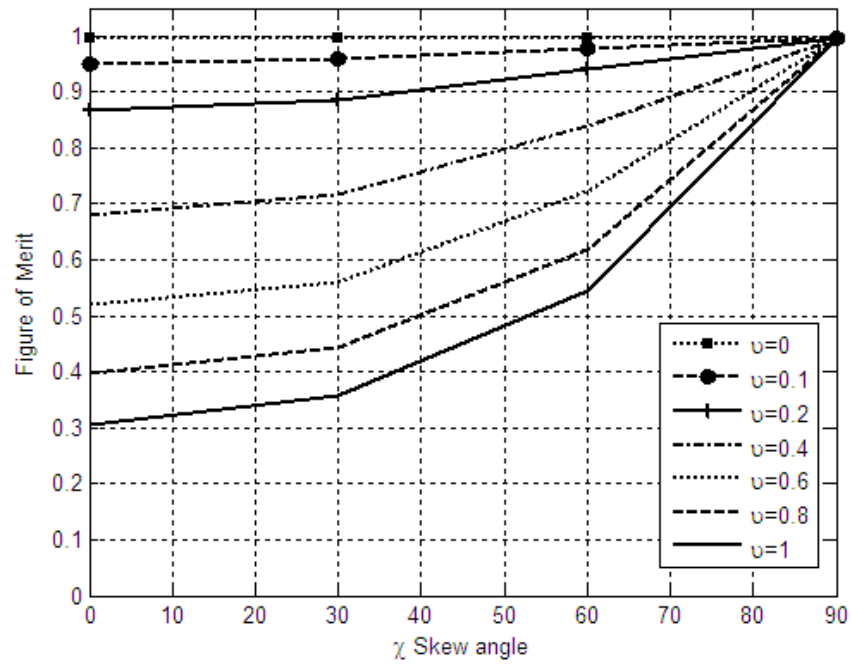


Figure 4.25: Figure of Merit change with Skew Angle. 20 harmonics.

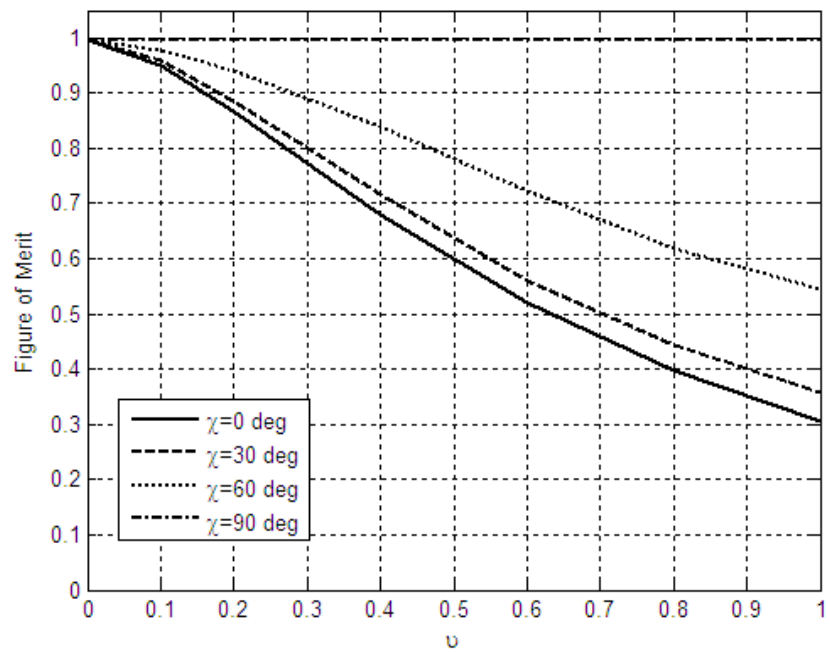


Figure 4.26: Figure of Merit change with Total Inflow. 20 harmonics.

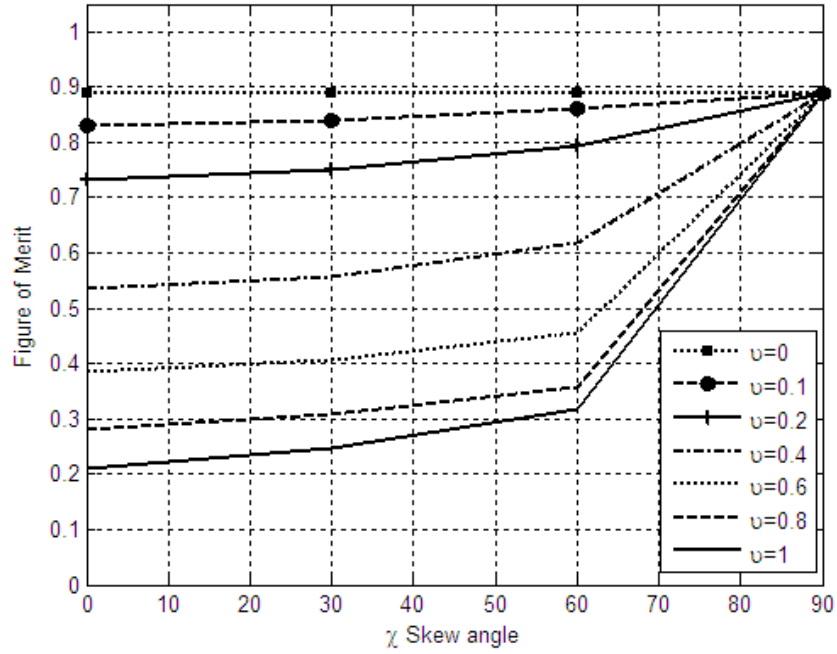


Figure 4.27: Figure of Merit change with Skew Angle. 1 harmonic.

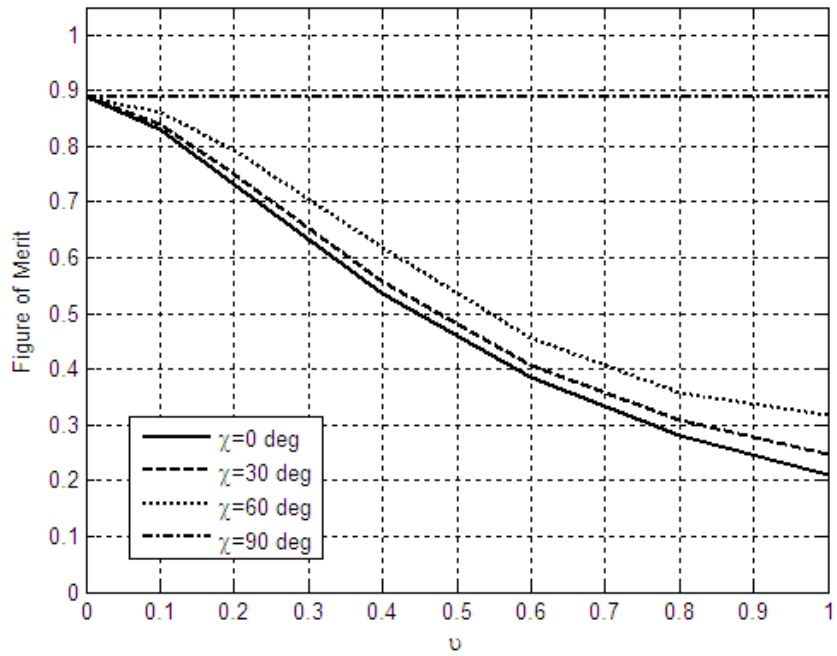


Figure 4.28: Figure of Merit change with Total Inflow. 1 harmonics.

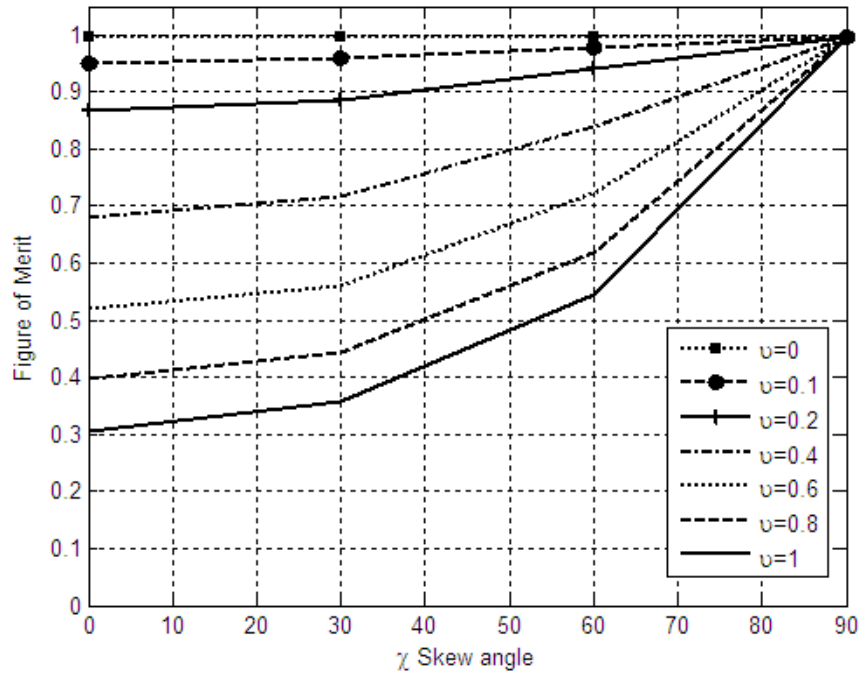


Figure 4.29: Figure of Merit change with Skew Angle. 20 harmonics, constrained inflow states

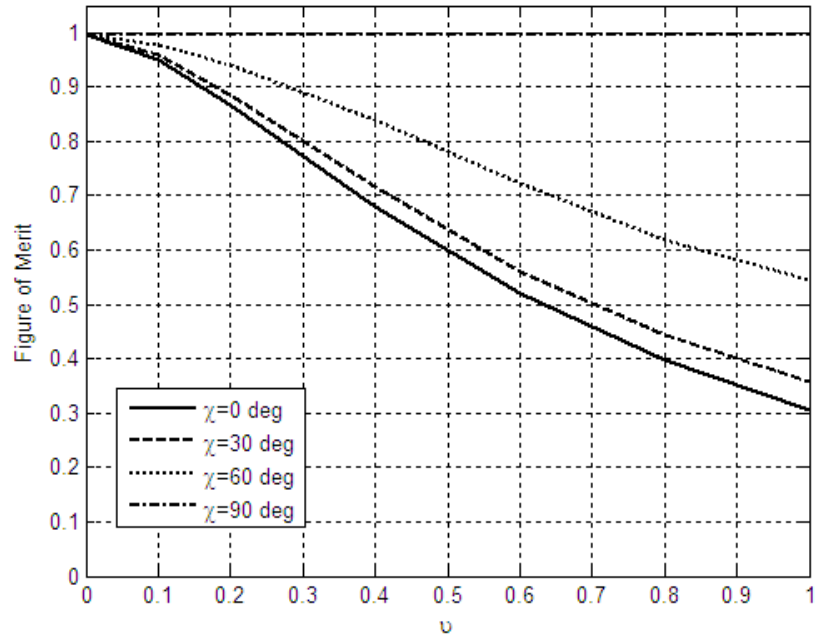


Figure 4.30: Figure of Merit change with Total Inflow. 20 harmonics, constrained inflow states

Figure 4.26 shows the figure of merit change for different skew angles. For the case of edgewise flow ($\chi=90^\circ$), the figure of merit does not change with v because there is no tilt, λ . To understand what is happening with this curve, we can see the definition of the cosine of tilt angle, $\cos\varphi$ in Equation (4.28). For any advance ratio, if $\lambda=0$, $\cos\varphi$ equals 1. Therefore, the influence coefficient vectors for all of these cases are the same, which make the figure of merit equal for all cases. Physically, the fact that the figure of merit does not change for edgewise flow is predictable since all of the incoming flow is oriented on the same plane of the rotor, so there are no losses on the perpendicular direction.

The tendency for the figure of merit for the rest of the skew angles in Figure 4.26 is given by a combination of tilt and advance. For the case of axial flow ($\chi=0^\circ$), the loss of efficiency is the greatest. For axial flow, the advance ratio is zero, therefore all of the reduction in figure of merit is due to tilt.

Several test points are taken and compared to previous results and validate the method to obtain the curves in Figure 4.26. Figure 4.21 is used to check for the case of axial flow (lowest-ordinate curve in Figure 4.26). Figure 4.21 provides the figure of merit change with total inflow for different cases. The curves for Betz and Finite-state methods for infinite number of blades are used to check the curve for $\chi=0^\circ$ of Figure 4.26. For $v=1$, $\lambda=1$. For example, the value of figure of merit for this point in Figure 4.26 is 0.3. On the curve for Betz's figure of merit in Figure 4.21, for a $\lambda=1$, the value is also 0.3. This result proves that

the curves for Figure 4.26 are accurate and depict the change in figure of merit for different conditions.

Figures 4.27 and 4.28 show the same as the above but for the case of one harmonic. The number of terms is drastically reduced from 231 to 3 (due to the harmonics and the corresponding inflow states). A table to determine the inflow states for any number of harmonics is shown in Appendix E. To understand the effect of introducing a larger number of harmonics, we take the rotor and divide it radially and azimuthally into sections. The more harmonics, the more azimuthal stations and the more inflow states, the more radial partitions. Because of the reduced number of partitions, it is not surprising that the accuracy of the calculations is greatly reduced. Hence the reduction of the figure of merit reading for all of the cases. Figures 4.27 and 4.28 demonstrate the importance of the use of more harmonics and their corresponding inflow states in the calculations. A similar conclusion was drawn for the case of axial flow prior to making the necessary calculations for forward flight. The determination of the appropriate number of harmonics is discussed more in detail on Appendix E. If only one harmonic is considered, the optimization would be performed taking into account that only one characteristic can be varied. For example, if only collective pitch could be controlled, then once the optimization is performed, the efficiency values on Figures 4.27 and 4.28 would be the result of this only variation. It is seen that the figure of merit decreases considerably if only one characteristic could be varied.

Finally, Figures 4.29 and 4.30 are calculated to check the impact on figure of merit when the inflow states are constrained. For these cases the number of harmonics is chosen to give

accurate results, but the number of inflow states is constrained. Physically, the pressure distribution (through the pressure coefficients, τ_n^m 's) is constrained to only allow non-zero values for the zeroth and the first harmonic ($m=0$ and $m=1$ for sine and cosine only). The impact on figure of merit is not perceptible, which means that we could disregard the rest of the partitions as they do not contribute on figure of merit. However, the repercussion on pressure and induced flow would be greater, since some of the areas where the distributions have abrupt changes would not be depicted as accurately.

Figures 4.31 through 4.52 show the pressure and velocity distributions for all of the cases in Table 4.1 that correspond to skewed flow. Note that the pressure distribution in Figure 4.55 and the induced velocity distribution shown in Figure 4.56 correspond to edgewise flow for **all** values of tilt and advance. For the induced velocity plots, the shape for all will be the same, but the magnitude will change proportional to v . When the skew angle is 90° , then $\lambda = 0$. Going back to the equation for the cosine of the tilt angle, if the climb is zero, then $\cos\phi = 1$, independently of the advance ratio μ . Therefore, the pressure and velocity distributions do not change.

It has already been explained how the inflow and pressure distributions change for axial flow. In general, for increasing tilt and advance, the distributions at the root of the rotor decreases with increasing tilt. A similar pattern appears for all of the cases in forward flight but with a main difference. In forward flight, as v increases, and the skew angle is increased,

the depression at the root shifts to the reversed-flow region and becomes downwash (negative).

Figure 4.27 shows the pressure distribution around the rotor. As predicted by momentum theory, this optimal distribution occurs when the pressure is constant. As mentioned before, no previous classical theories could predict how the induced velocity would behave for skewed flow. Figure 4.33 shows that the induced velocity has a gradient when in forward flight conditions. The rotor forward position is for $r \cos \varphi = -1$, where the inflow distribution is smaller and it steadily increases towards the aft rotor position.

Since the general pattern for different skew angles is similar, let us discuss the cases for $\chi=60^\circ$. This case is chosen because the figure of merit has a value half-way between the ideal of 1 and the minimum for axial flow ($\chi=0^\circ$). Starting with the simplest case shown in Figure 4.39, the rotor presents a constant pressure distribution and a sloped inflow distribution, as discussed above. When the combination of tilt and advance increases a region of downwash appears at the center of the rotor. The downwash keeps increasing and shifting sideways. This shift is mainly due to the fact that for skewed flow, the sine terms of the equations are present and contribute to the shape of the pressure and inflow distributions. The sine part of the definition for both pressure and induced velocity is now present, and it changes sign for $\psi>180^\circ$, where the rotor changes from advancing to retreating side and the reverse flow region occurs.

Similar conclusions can be drawn for the cases where $\chi=30^\circ$ or any other skew angle ranging between these values. The main differences are the point at which the downwash appears and the magnitude of this downwash.

Figures 4.51 and 4.52 show the pressure and induced velocity distributions for edgewise flow ($\chi=90^\circ$) and all values of tilt and advance ratios. For edgewise flow, these distributions do not change, as was discussed previously. Of importance is to notice that, in particular, the profile of the inflow has a slope (similar to what happened for all other skewed flow cases). It is also important to notice the appearance of spikes or peaks at (areas of increased inflow) at $\psi=90^\circ$ and $\psi=270^\circ$. For pure edgewise flow, all the incoming flow is at the plane of the rotor. This means that no flow will develop on the perpendicular plane. It is, in some ways, similar to what happens to a fixed-wing, and the points where the peaks occur are really tip vortices due to the fact that the rotor does not have an infinite length. (Recall that the flow is coming from $\psi=180^\circ$).

Figures 4.53 through 4.58 show specific views for all of the cases in the previous figures (including the ones for axial flow shown in Section 4.2.3). Figures 4.53 and 4.56 show the top view of the rotor area. These are important to show because in the previous figures the downwash appears to be located in the center of the rotor, while in fact it is shifting towards the reversed-flow region as the climb and advance increase (increasing v). For an explanation for the reversed-flow region see Appendix F. Figures 4.54 and 4.57 show side views for the pressure and induced velocity distributions for the same cases. The flow is coming into the rotor at $r \cos \varphi = -1$, and $r \cos \varphi = 1$ is the aft of the rotor. The asymmetry

is depicted in these figures, showing a downwash on the retreating side. This asymmetry is also present on the aft view shown in Figures 4.55 and 4.58, where the downwash is clearly present on the left-hand portion of the rotor.

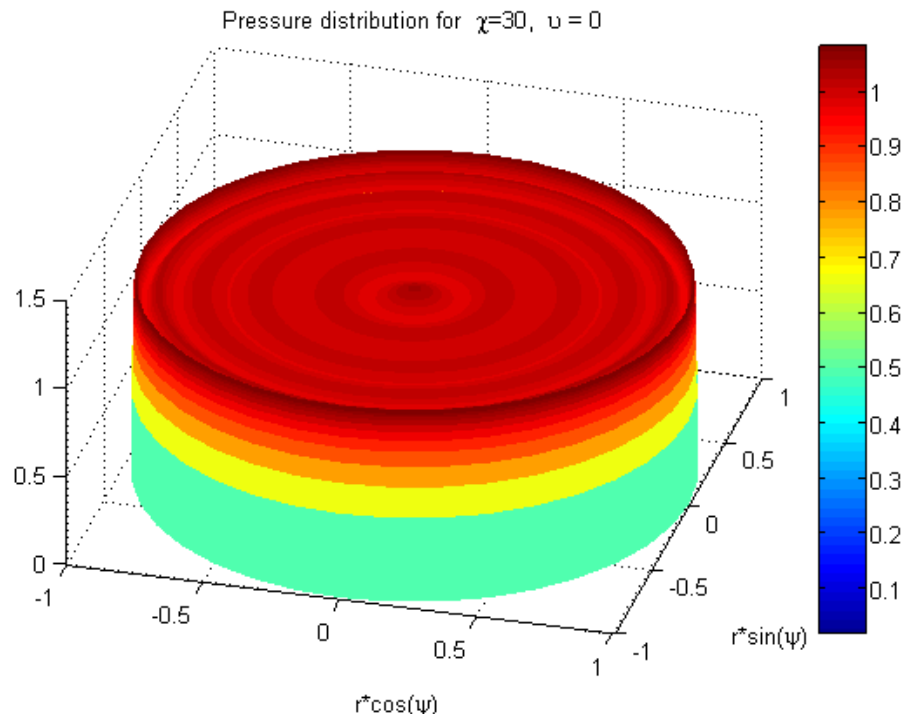


Figure 4.31: Pressure Distribution, $\chi = 30, v = 0.0, FM=1.0$.

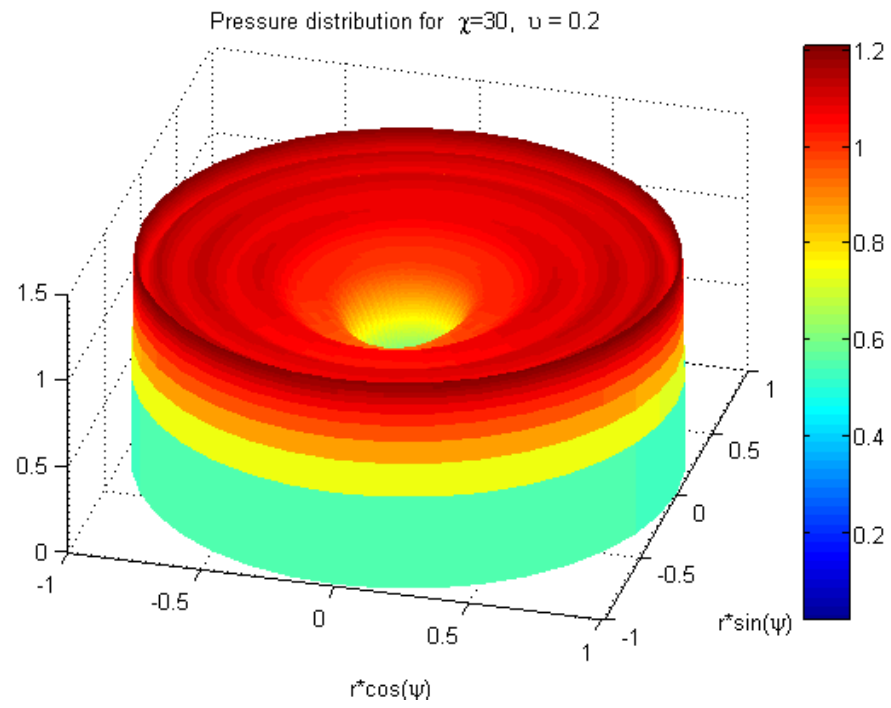


Figure 4.32: Pressure Distribution, $\chi = 30$, $\nu = 0.2$, FM=0.89.

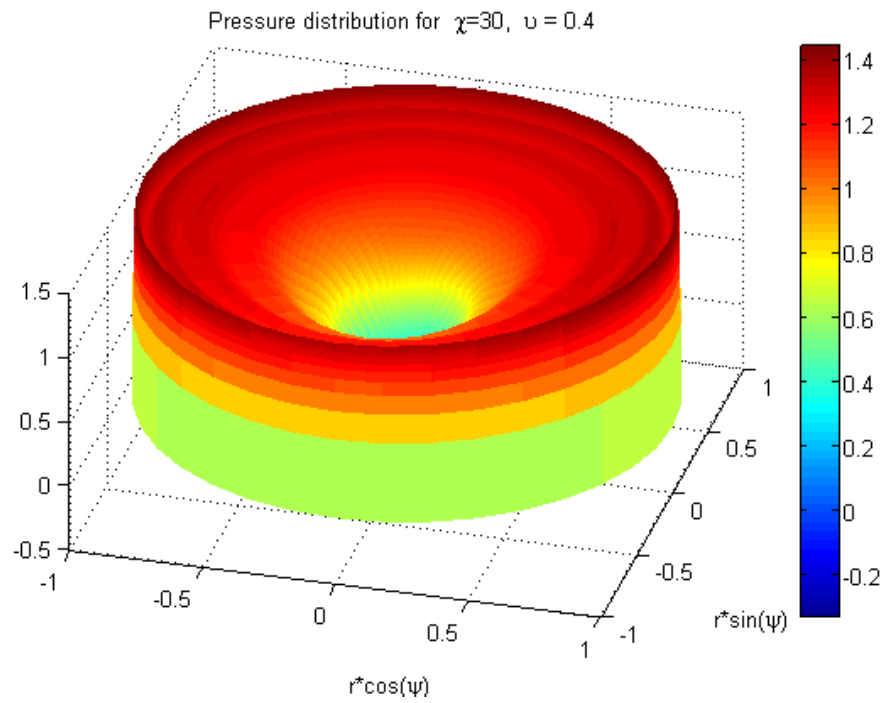


Figure 4.33: Pressure Distribution, $\chi = 30$, $\nu = 0.4$, FM=0.72.

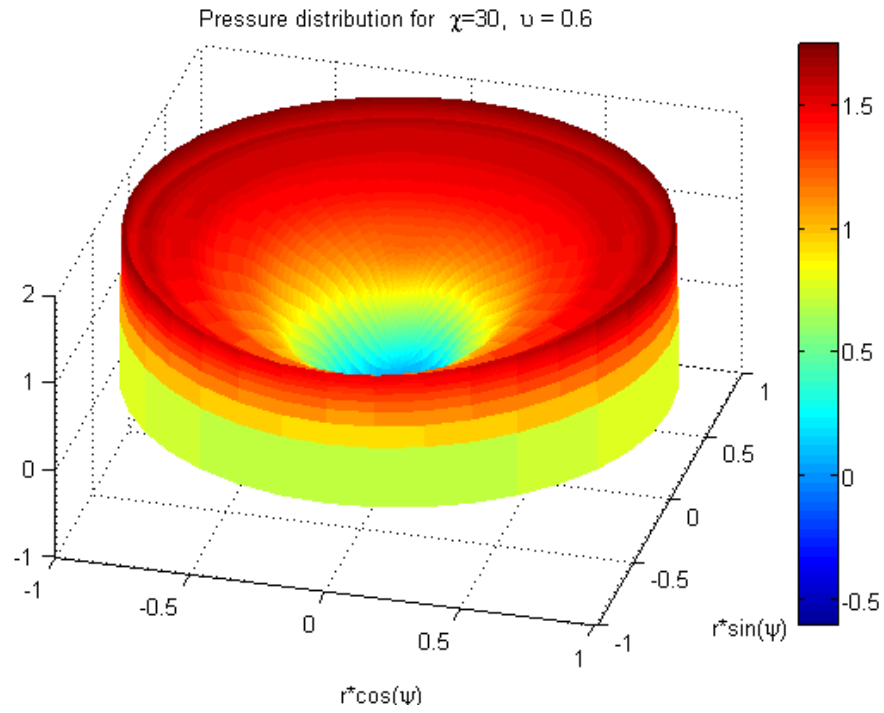


Figure 4.34: Pressure Distribution, $\chi = 30$, $\nu = 0.6$, FM=0.56.

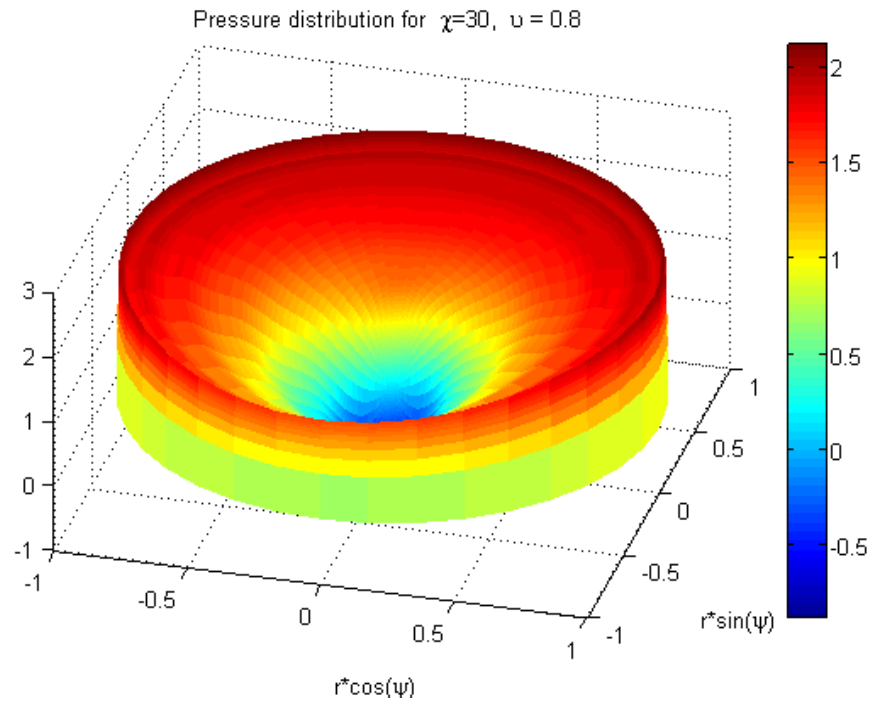


Figure 4.35: Pressure Distribution, $\chi = 30$, $\nu = 0.8$, FM=0.44.

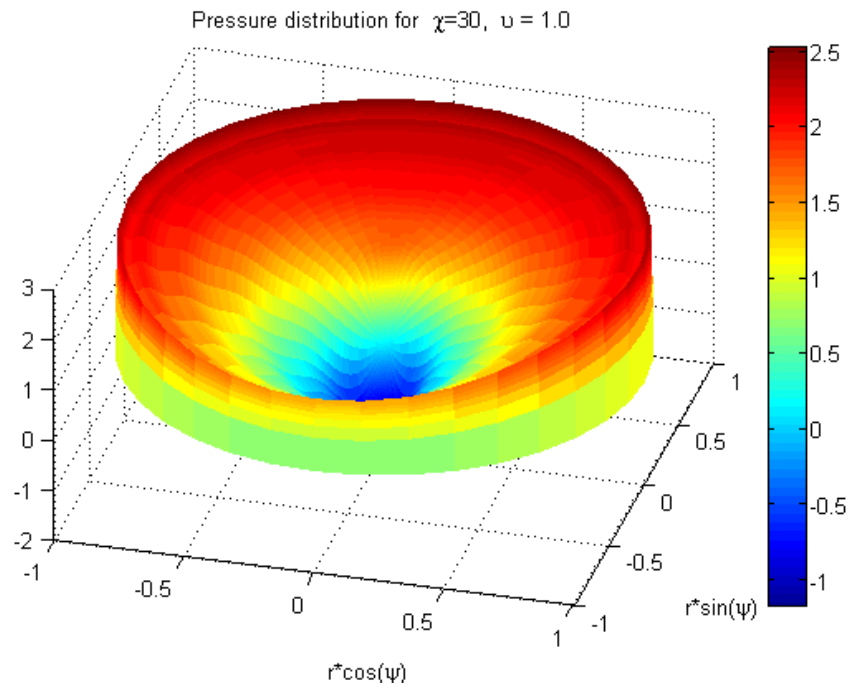


Figure 4.36: Pressure Distribution, $\chi = 30$, $\nu = 1.0$, FM=0.36.

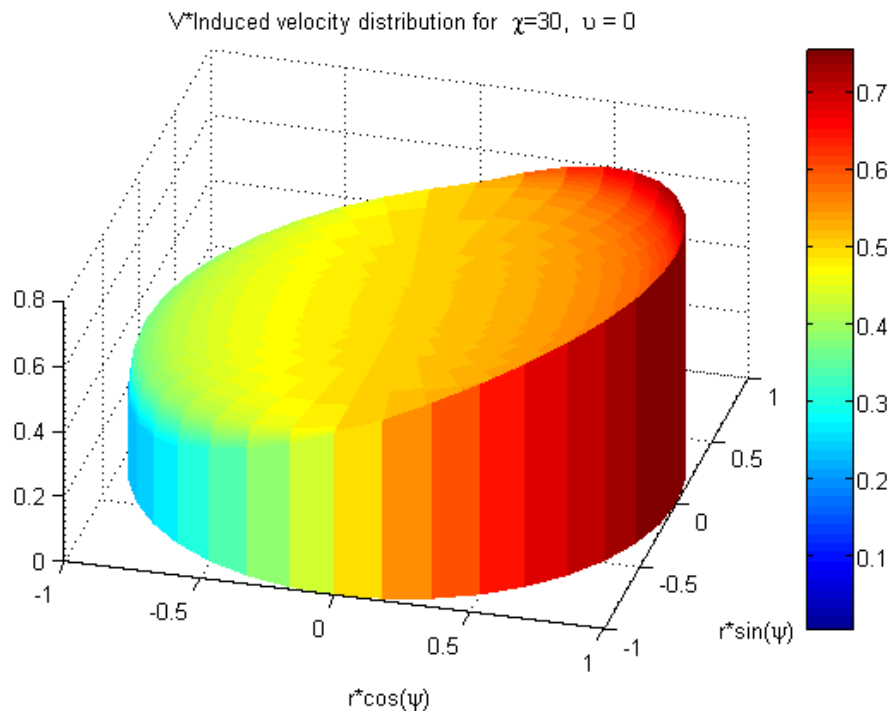


Figure 4.37: Induced Velocity Distribution, $\chi = 30$, $\nu = 0.0$, FM=1.0.

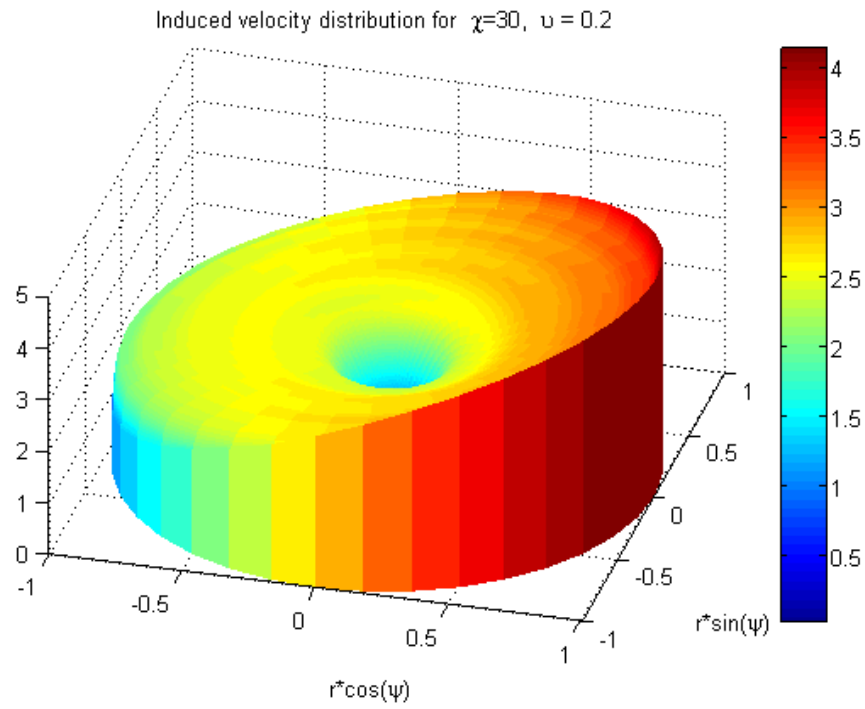


Figure 4.38: Induced Velocity Distribution, $\chi = 30$, $\nu = 0.2$, FM=0.89.

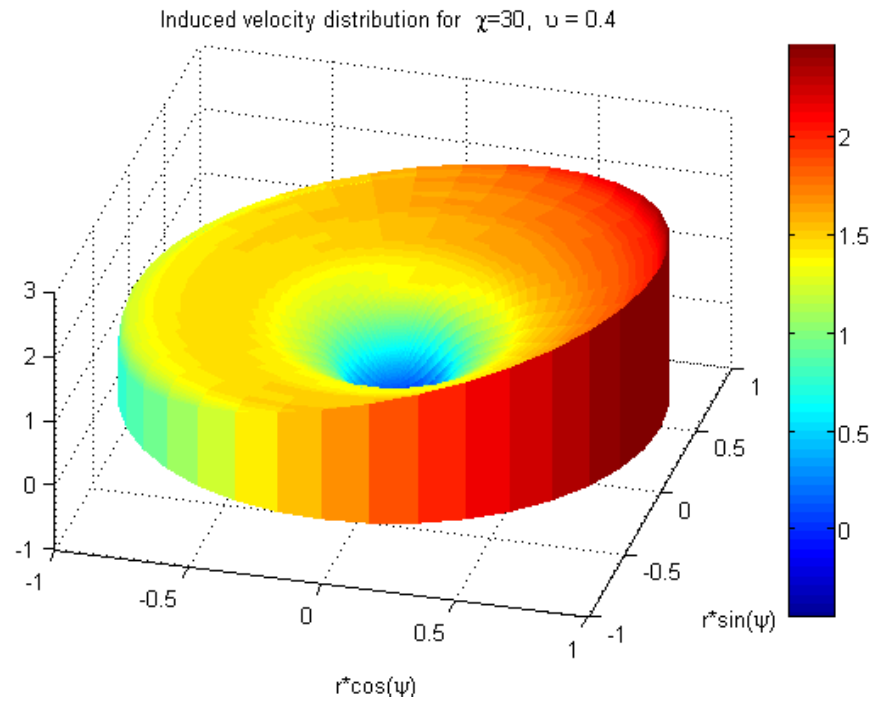


Figure 4.39: Induced Velocity Distribution, $\chi = 30$, $\nu = 0.4$, FM=0.72.

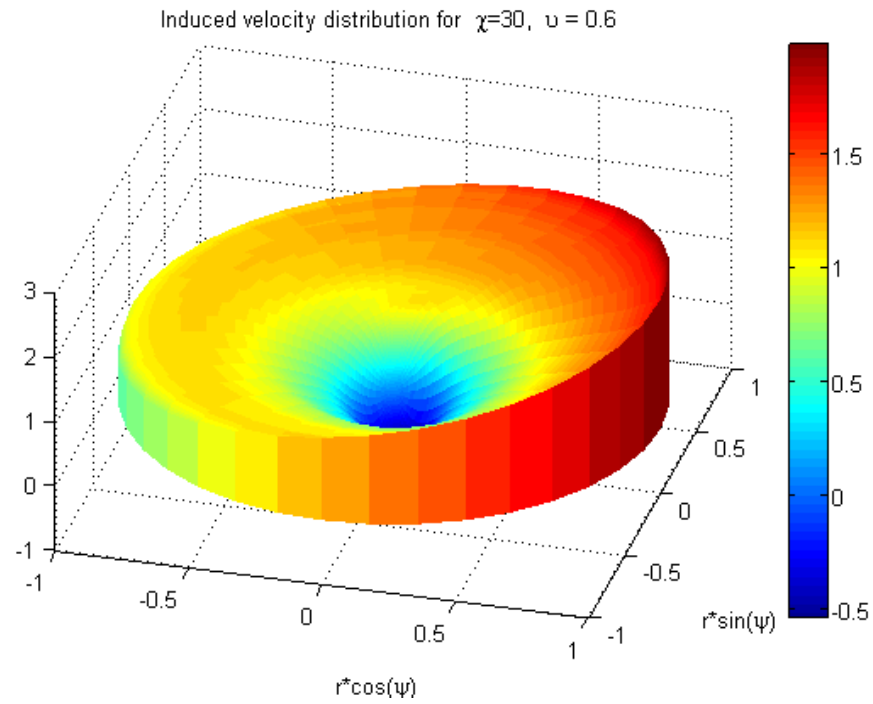


Figure 4.40: Induced Velocity Distribution, $\chi = 30$, $\nu = 0.6$, FM=0.56.

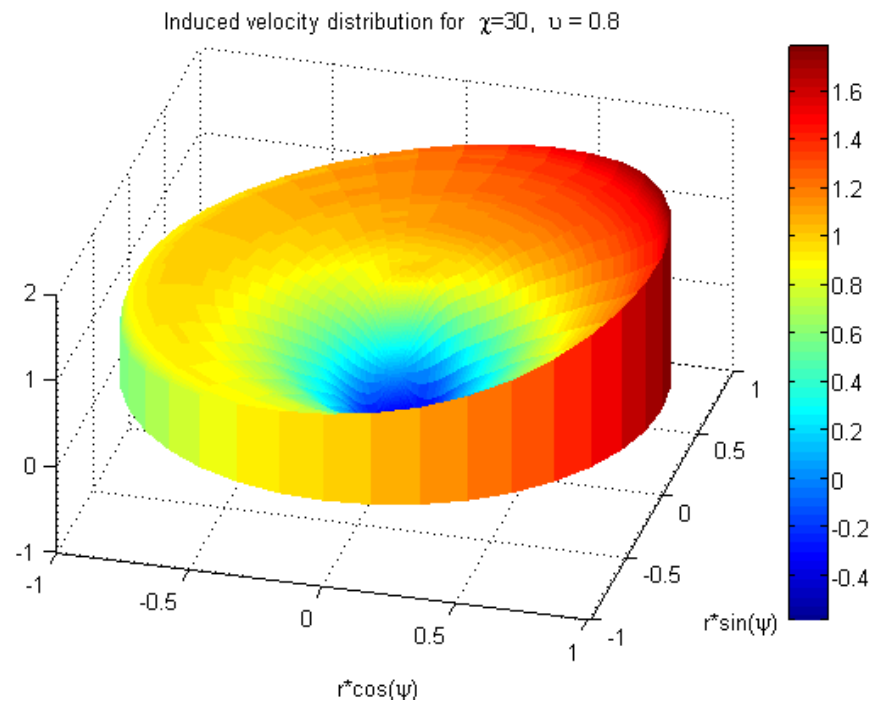


Figure 4.41: Induced Velocity Distribution, $\chi = 30$, $\nu = 0.8$, FM=0.44.

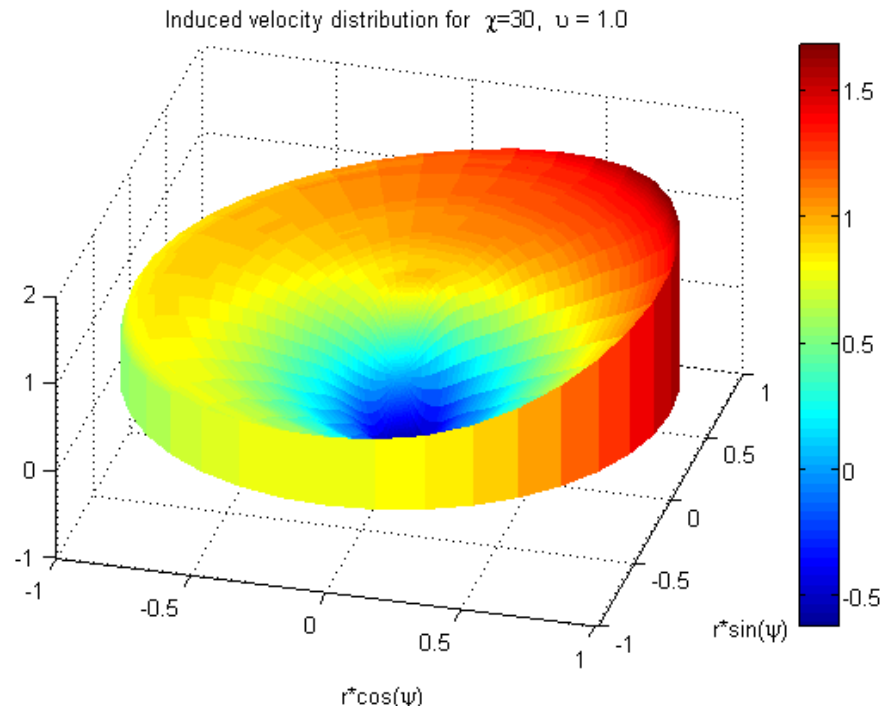


Figure 4.42: Induced Velocity Distribution, $\chi = 30$, $\nu = 1.0$, FM=0.36.

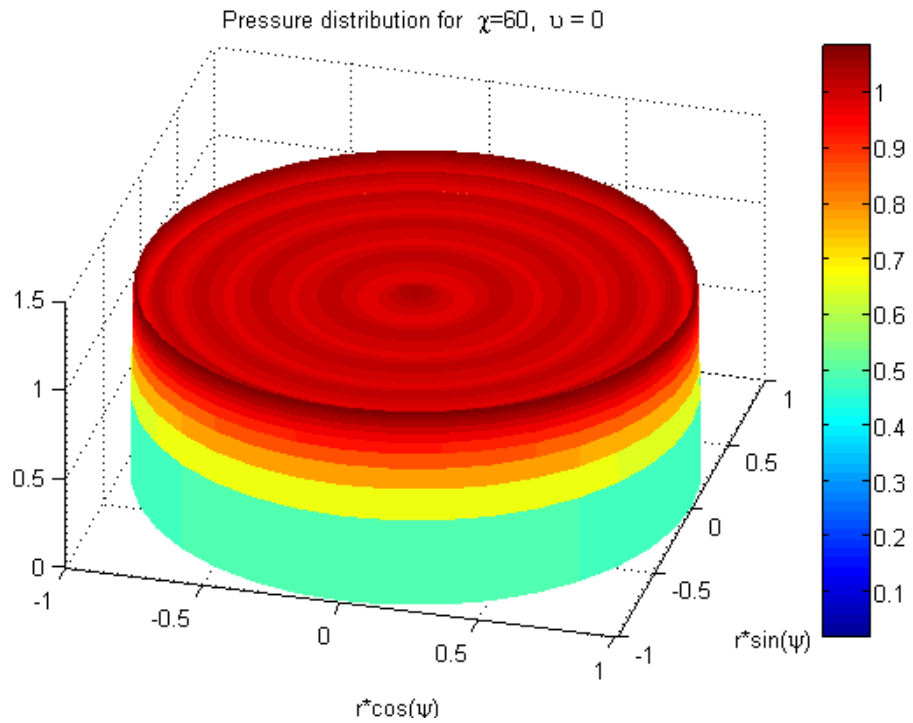


Figure 4.43: Pressure Distribution, $\chi = 60$, $\nu = 0.0$, FM=1.0.

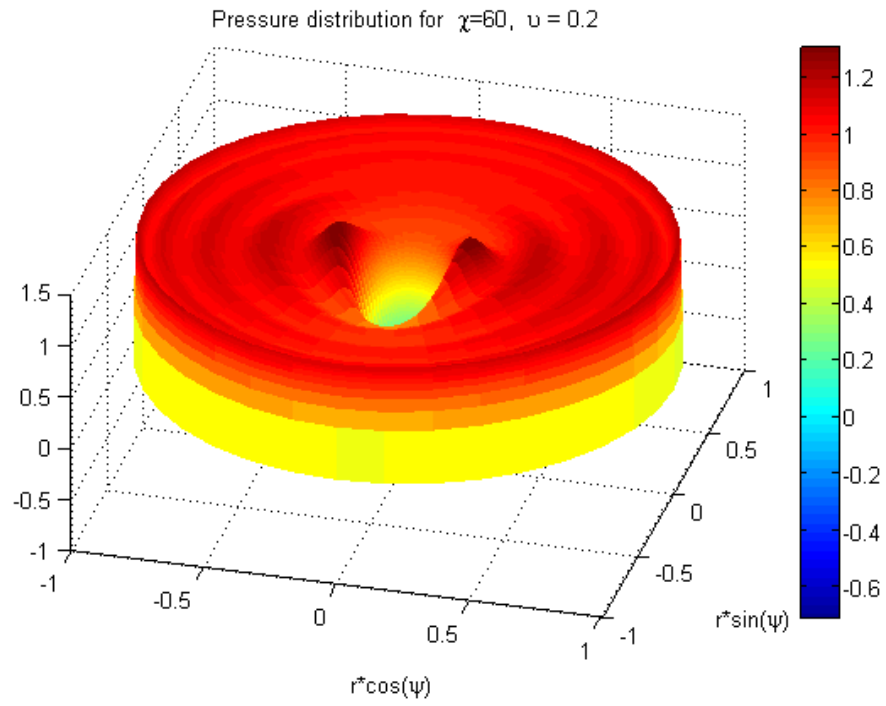


Figure 4.44: Pressure Distribution, $\chi = 60$, $\nu = 0.2$, FM=0.94.

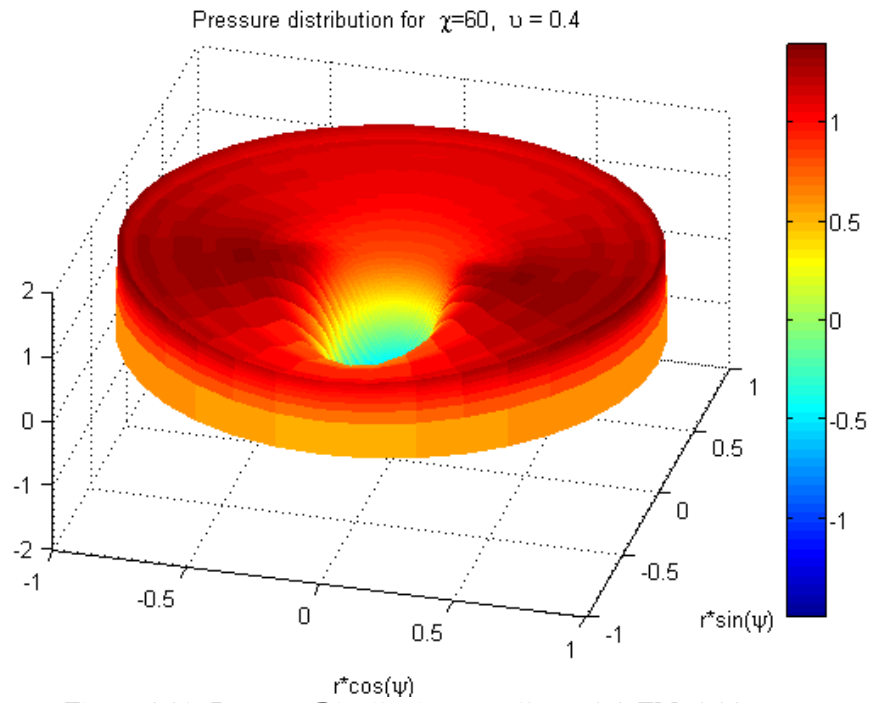


Figure 4.45: Pressure Distribution, $\chi = 60$, $\nu = 0.4$, FM=0.84.

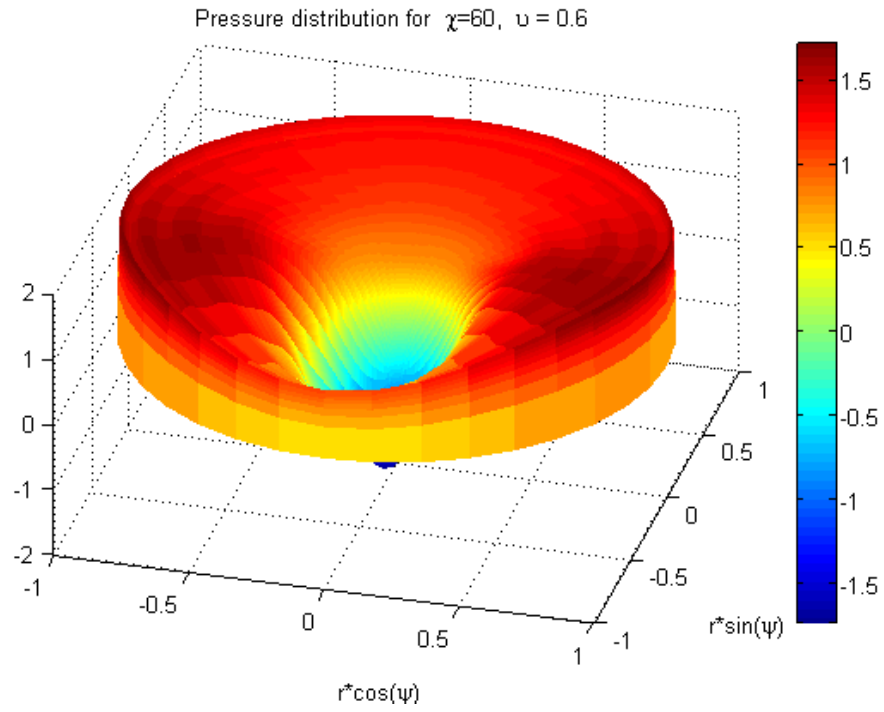


Figure 4.46: Pressure Distribution, $\chi = 60$, $\nu = 0.6$, FM=0.72.

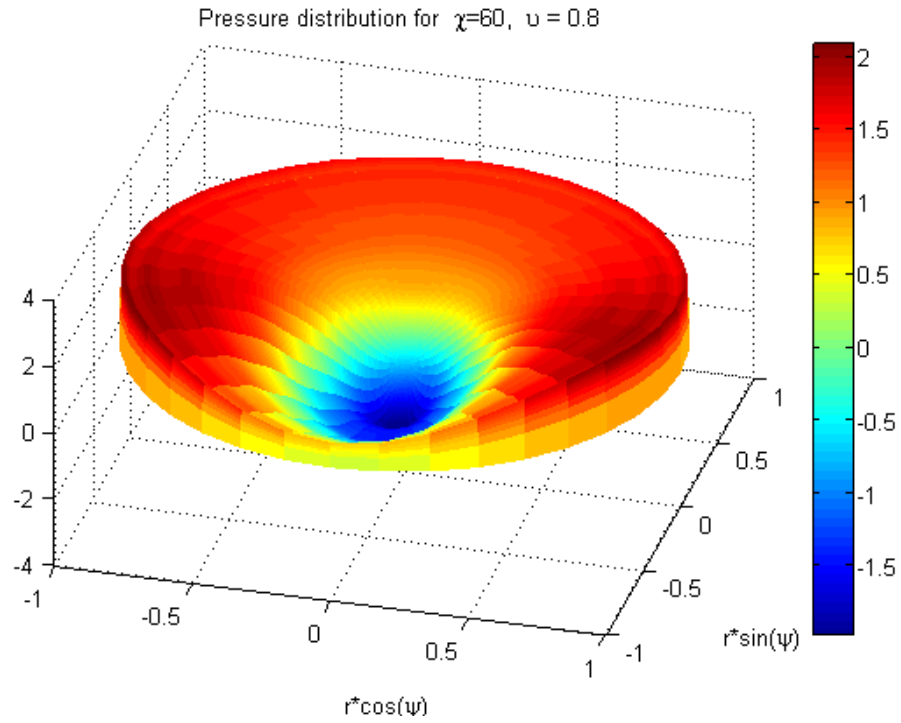


Figure 4.47: Pressure Distribution, $\chi = 60$, $\nu = 0.8$, FM=0.62.

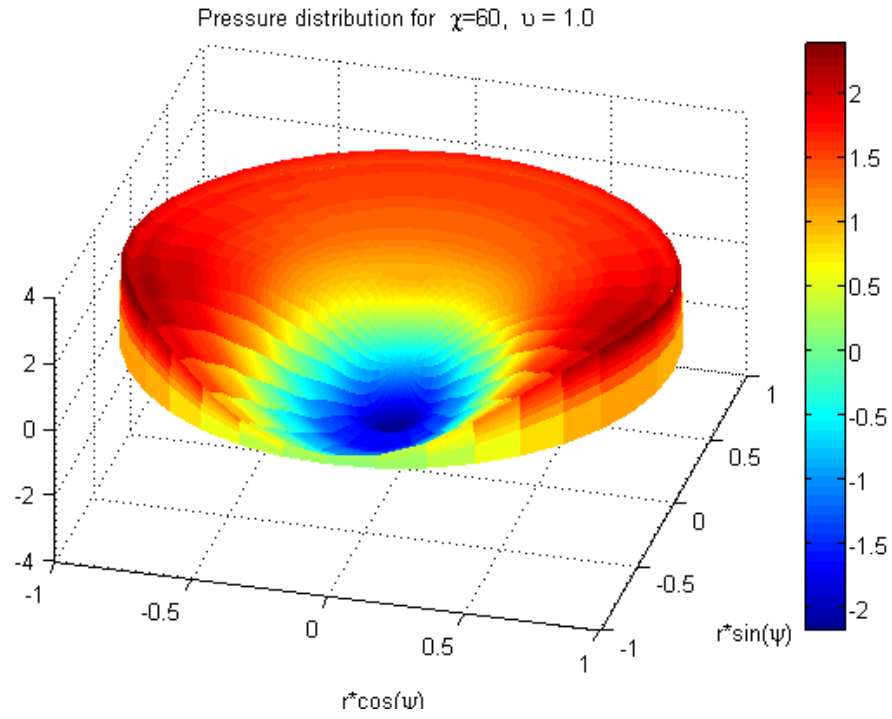


Figure 4.48: Pressure Distribution, $\chi = 60$, $\nu = 1.0$, FM=0.54.

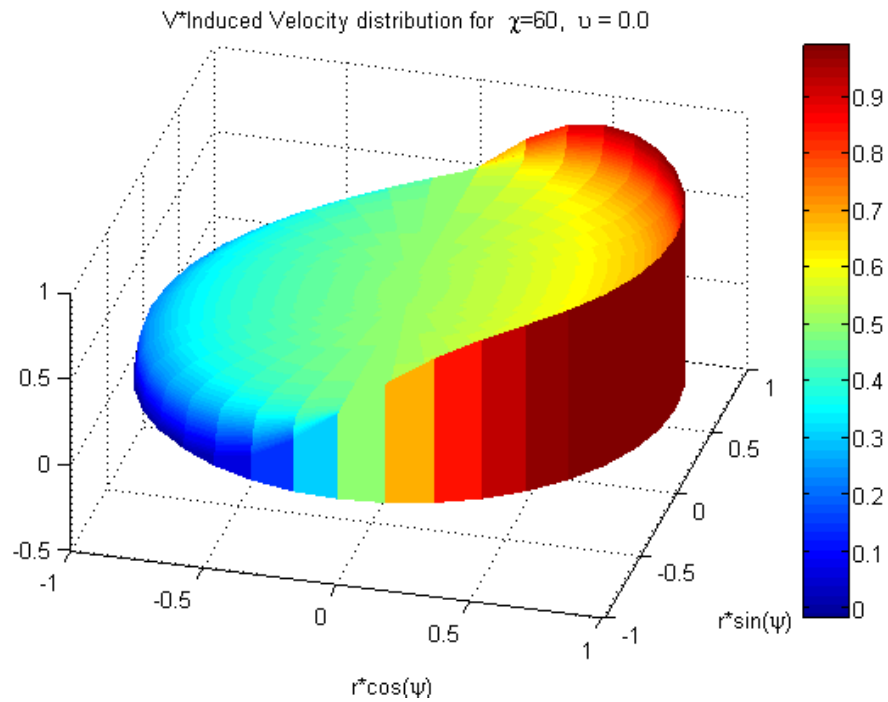


Figure 4.49: Induced Velocity Distribution, $\chi = 60$, $\nu = 0.0$, FM=1.0.

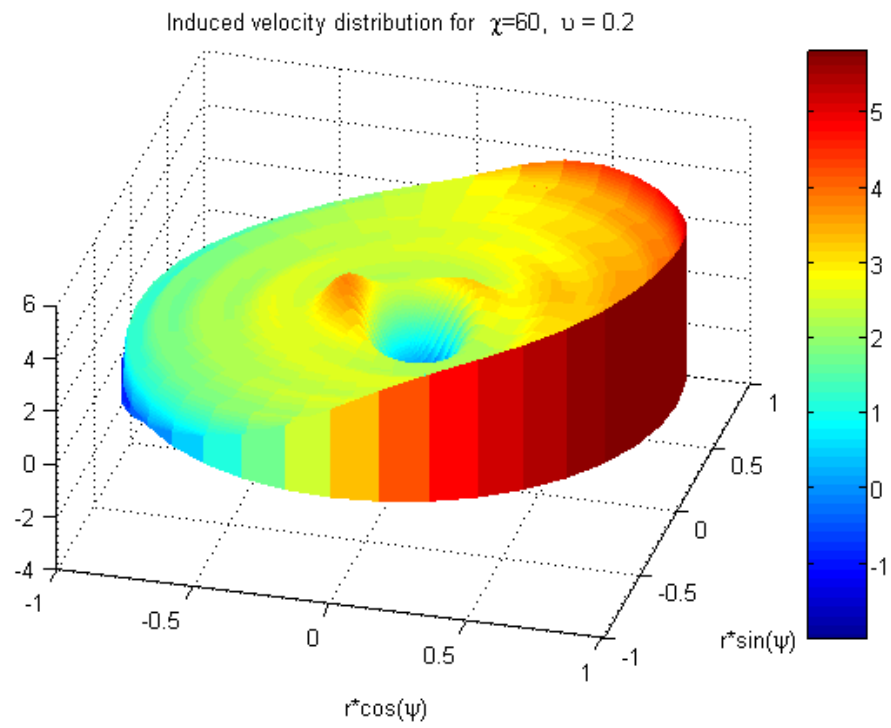


Figure 4.50: Induced Velocity Distribution, $\chi = 60$, $\nu = 0.2$, FM=0.94.

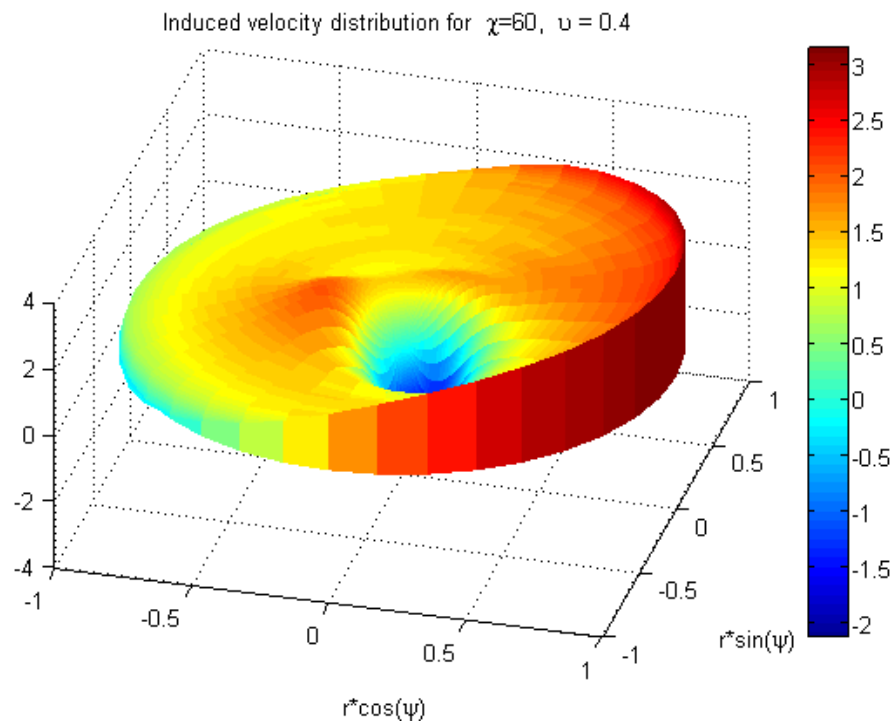


Figure 4.51: Induced Velocity Distribution, $\chi = 60$, $\nu = 0.4$, FM=0.84.

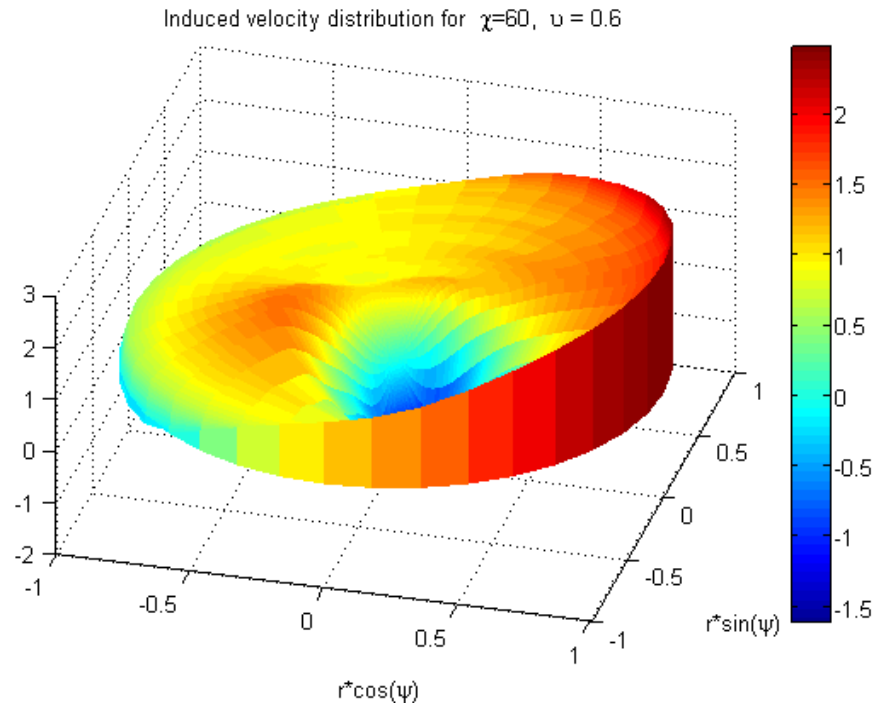


Figure 4.52: Induced Velocity Distribution, $\chi = 60$, $\nu = 0.6$, FM=0.72.

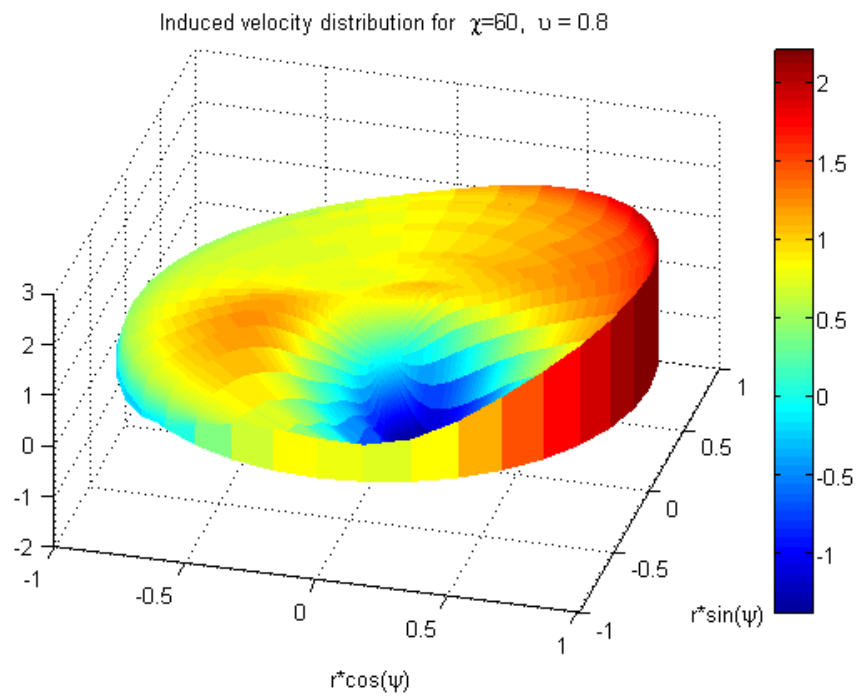


Figure 4.53: Induced Velocity Distribution, $\chi = 60$, $\nu = 0.8$, FM=0.62.

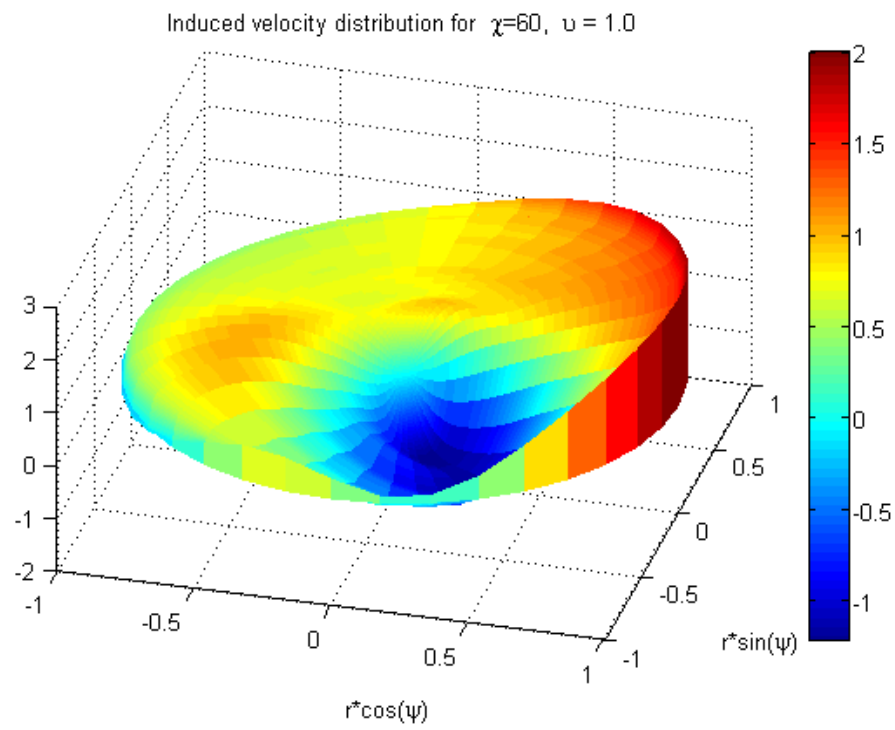


Figure 4.54: Induced Velocity Distribution, $\chi = 60$, $\nu = 1.0$, FM=0.54.

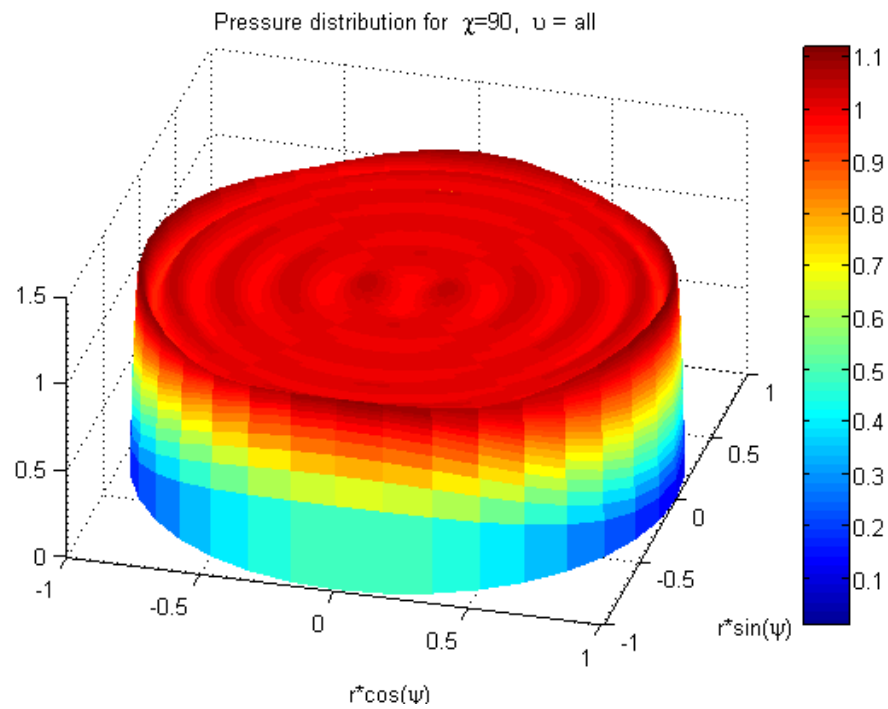


Figure 4.55: Pressure Distribution, $\chi = 90$, all values of ν , FM=1.0.

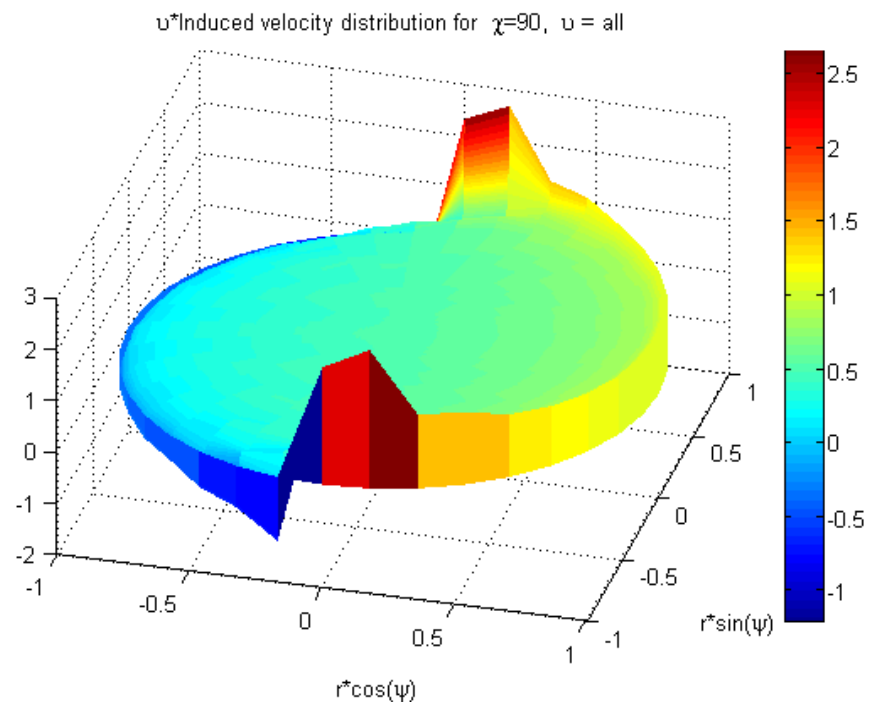


Figure 4.56: Induced Velocity Distribution, $\chi = 90$, all values of ν , FM=1.0.

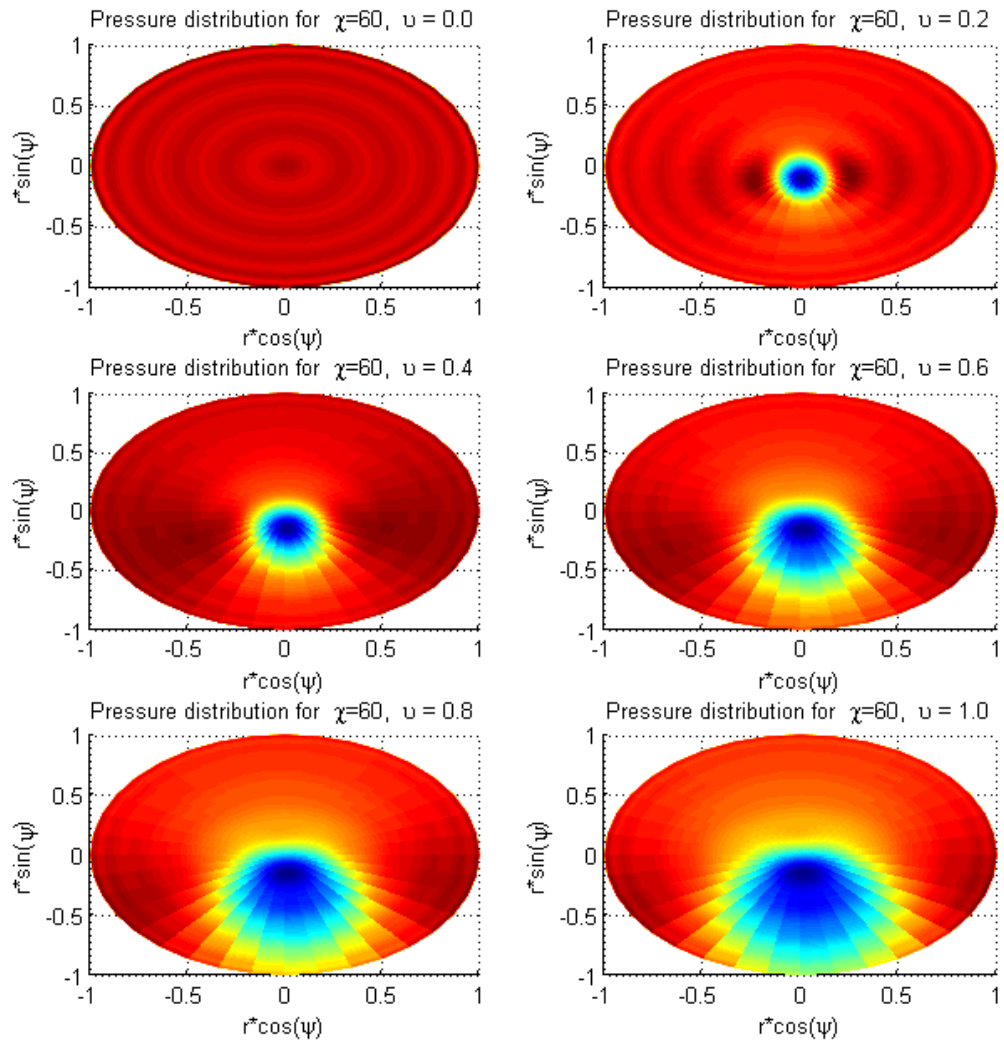


Figure 4.57: XY-plane View of Pressure Distribution, $\chi = 60$, various ν .

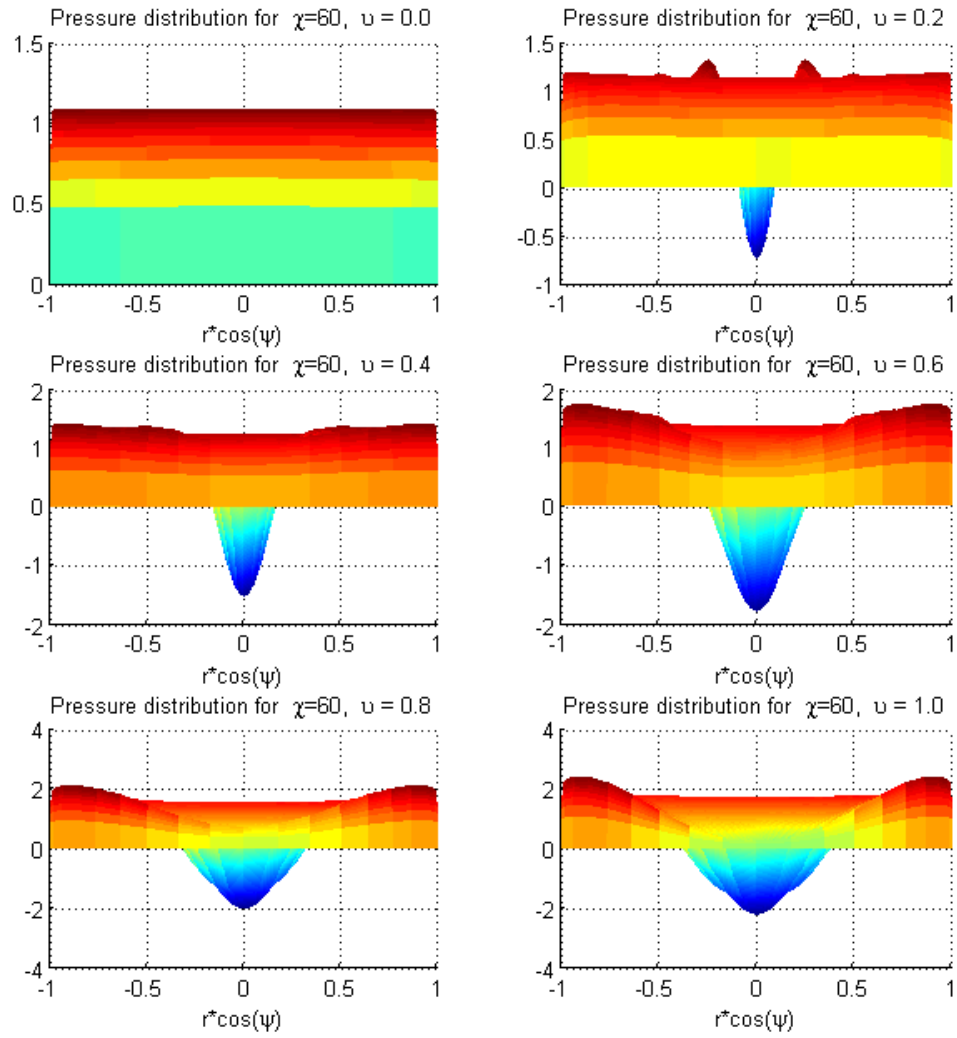


Figure 4.58: XZ-plane View of Pressure Distribution, $\chi = 60$, various ν .

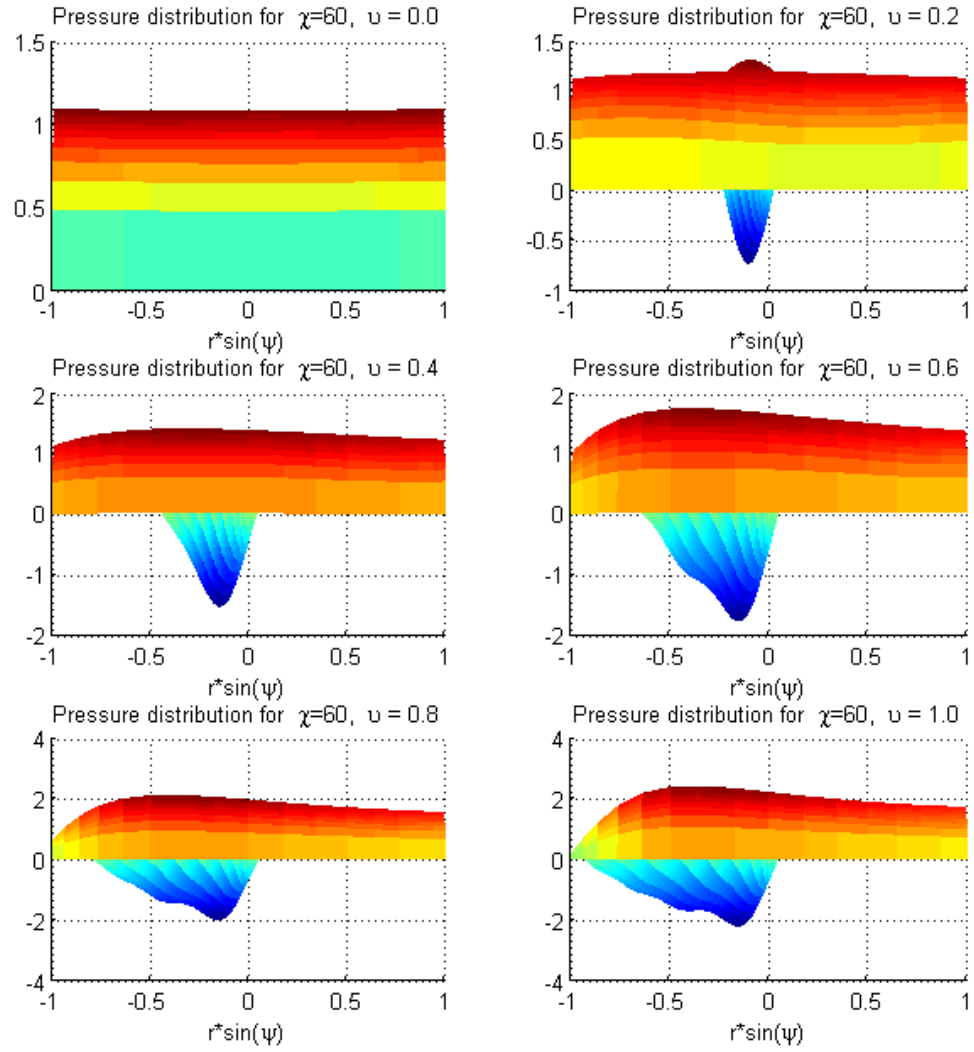


Figure 4.59: YZ-plane View of Pressure Distribution, $\chi = 60$, various ν .

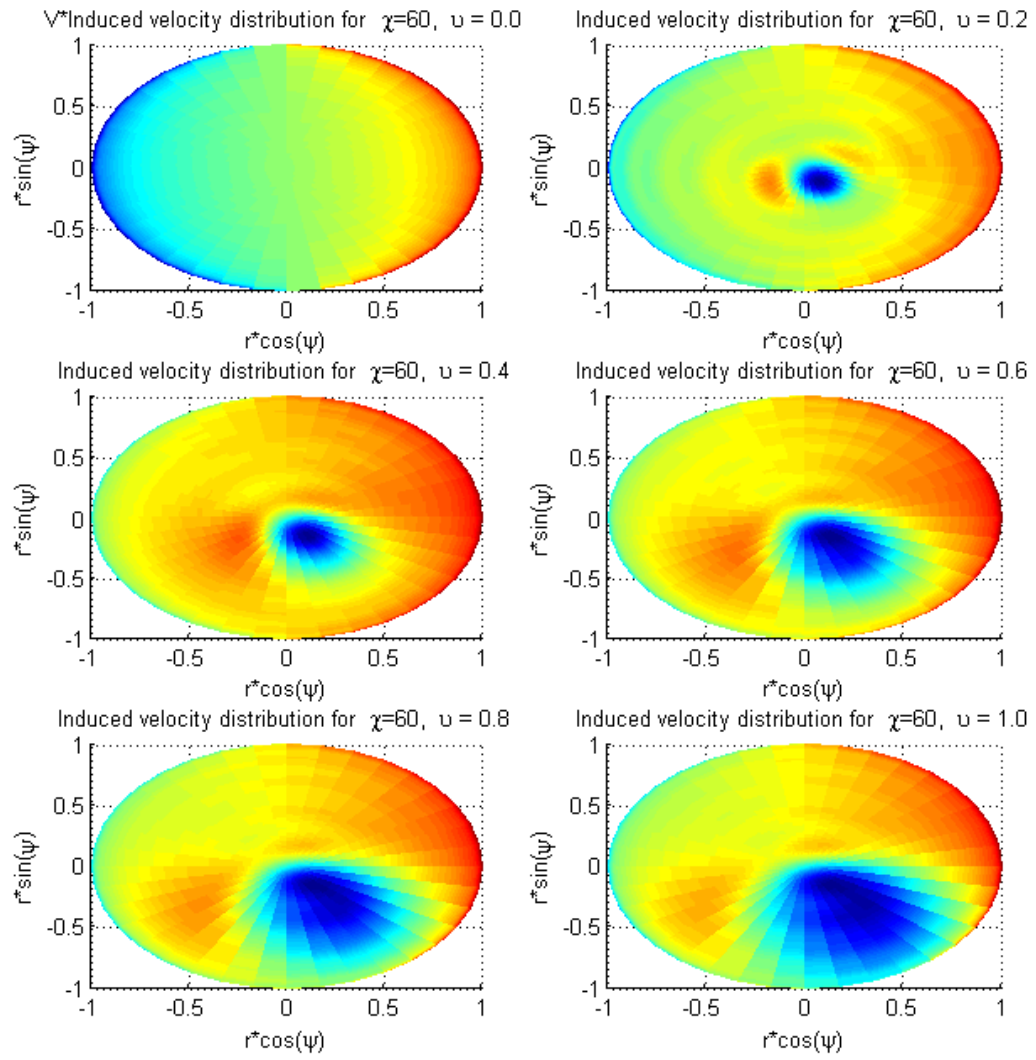


Figure 4.60: XY-plane View of Induced Velocity Distribution, $\chi = 60$, various ν .

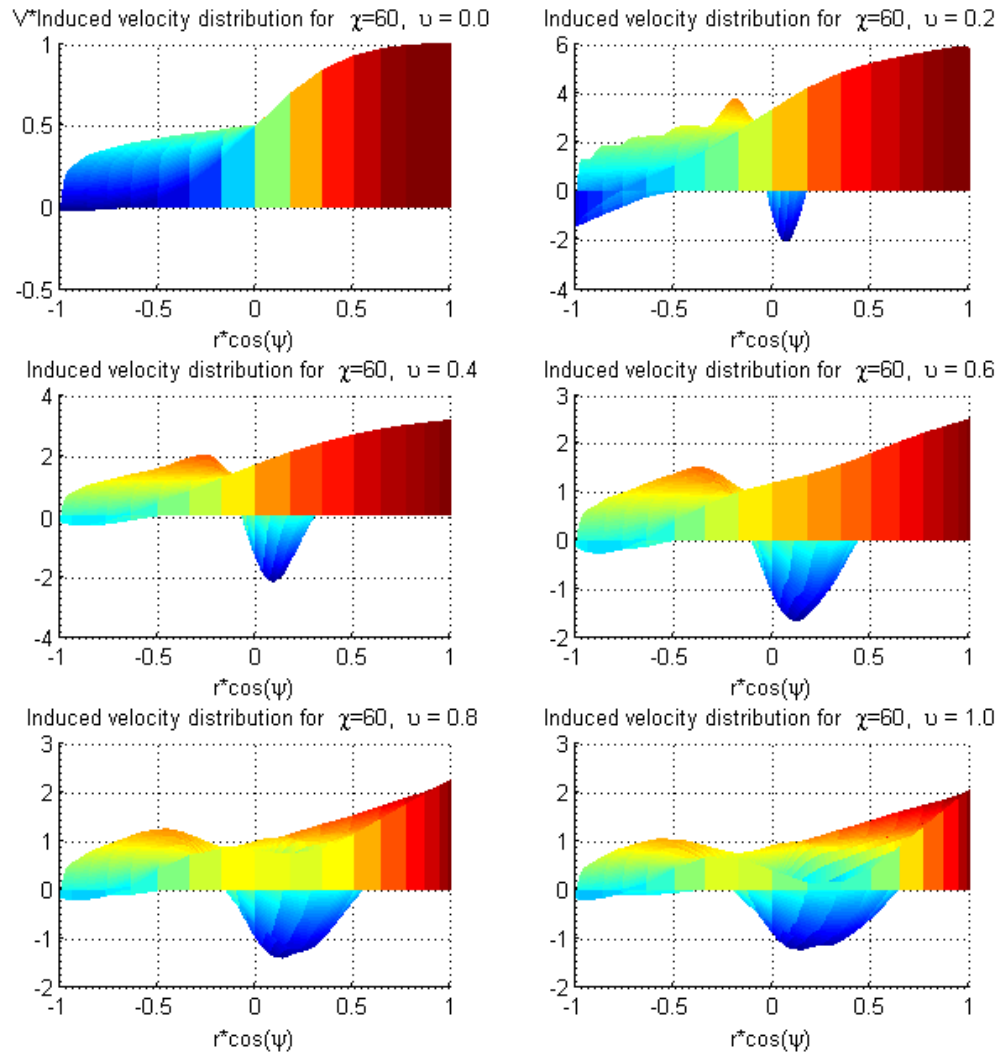


Figure 4.61: XZ-plane View of Induced Velocity Distribution, $\chi = 60$, various ν .

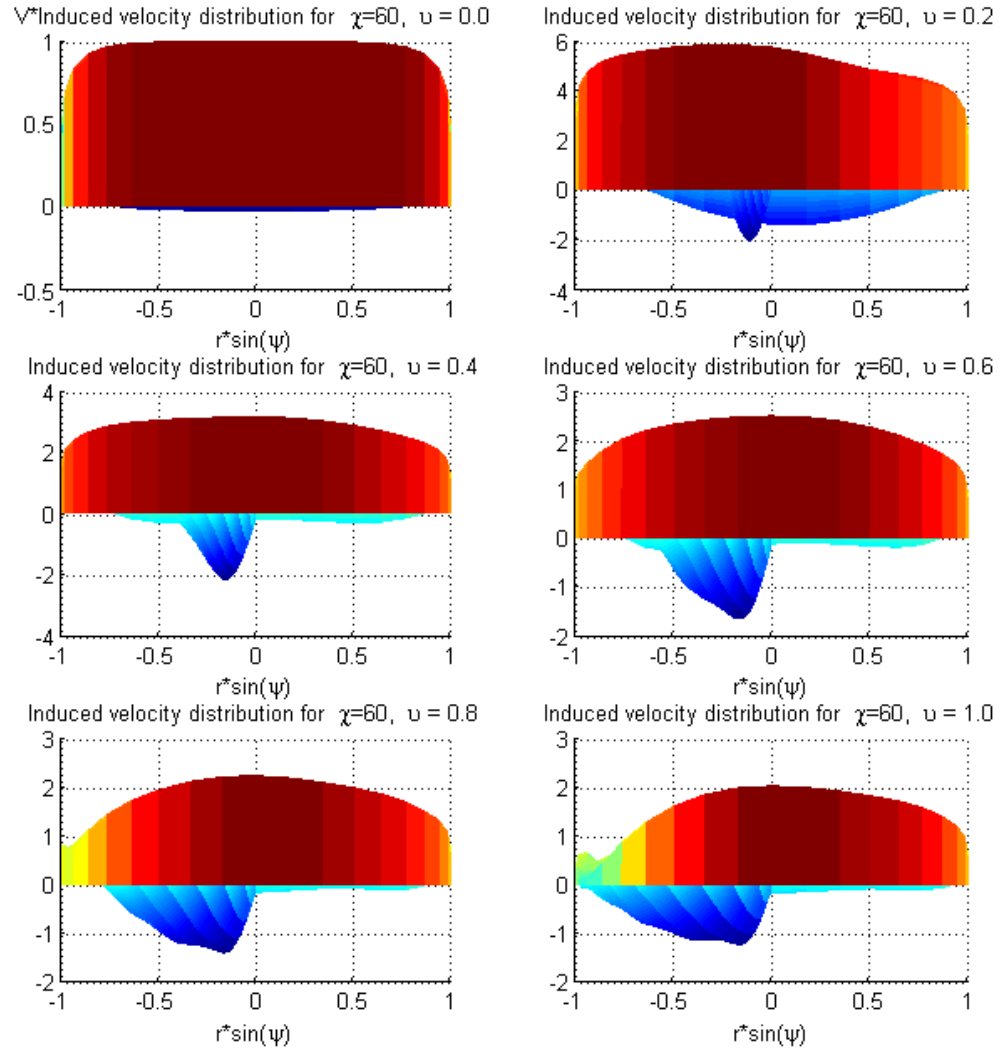


Figure 4.62: YZ-plane View of Induced Velocity Distribution, $\chi = 60$, various ν .

With the results in forward flight, the study of minimum induced power will be complete for any flight condition.

4.3.2. Finite Number of Blades

The theoretical development of the cases for a finite number of blades in skewed flow will be shown in this section. Theory for the cases of an actuator disk and tilted lift with a finite number of blades in forward flight can be derived using a modified system shown in the set of differential equations (3.9) and (3.10) described in Section 3.1.

$$\left[\bar{K}_n^{mc} \right] \{ \dot{\bar{\alpha}}_n^m \} + V \left[\bar{L}^c \right]^{-1} \{ \bar{\alpha}_n^m \} = \frac{1}{2} \{ \tau_n^{mc} \} \quad (4.73)$$

$$\left[\bar{K}_n^{ms} \right] \{ \dot{\bar{\beta}}_n^m \} + V \left[\bar{L}^s \right]^{-1} \{ \bar{\beta}_n^m \} = \frac{1}{2} \{ \tau_n^{ms} \} \quad (4.74)$$

The influence coefficient matrices, $\left[\bar{L}^c \right], \left[\bar{L}^s \right]$ are the matrices defined by Equation (3.12) where the row partitions where $m \neq 0$ have been divided by two. The multiplication enables the computation to become simpler due to the fact that the matrices can then be divided into symmetric and asymmetric parts. Both symmetric and asymmetric parts of the matrices are used. Note that the symmetric part provides only $r+m$ even terms only, and the asymmetric part gives the $r+m$ odd for $j = n \pm 1$ terms only.

$\left[\bar{K}_n^{mc}\right]$ and $\left[\bar{K}_n^{ms}\right]$ are the apparent mass matrices also provided in Section 3.1 where again, the row partitions for $m \neq 0$ have been divided by two, and so on for the rest of the terms in Equations (4.73) and (4.74).

So far, this formulation is valid for a system with an infinite or a finite number of blades in both axial and skewed flow conditions and for an actuator disk, or for the case where the tilt on the lift is considered. The changes made for each of the cases has been discussed in previous sections. Certain variations will be included for this particular case of skewed flow and a finite number of blades.

First of all, in previous cases where an infinite number of blades was considered, the system described by Equations (4.73) and (4.74) was reduced to a steady case. For the case of finite number of blades, this is no longer a steady system. Moreover, for previous cases in axial flow, the sine-related equations all reduced to zero, but that is no longer the case, since both cosine and sine contribute for the case of skewed flow and finite number of blades.

Because of the time dependence of the system, the pressure coefficients, $\{\tau_n^{mc}\}$ and $\{\tau_n^{ms}\}$, become unsteady. As a direct consequence of the unsteadiness of the pressure, the induced velocity coefficients, $\{\bar{\alpha}_n^m\}$ and $\{\bar{\beta}_n^m\}$, also become unsteady. Equations (4.75) and (4.76) show the unsteady pressure and inflow coefficient expressions.

$$\begin{aligned}\{\tau_n^{mc}\} &= \{\tau_n^{mc}\}_0 + \sum_{p=Q,2Q,3Q,\dots} \left(\{\tau_n^{mc}\}_{\varphi} \cos p\bar{t} + \{\tau_n^{mc}\}_{\varphi} \sin p\bar{t} \right) \\ \{\tau_n^{ms}\} &= \{\tau_n^{ms}\}_0 + \sum_{p=Q,2Q,3Q,\dots} \left(\{\tau_n^{ms}\}_{\varphi} \cos p\bar{t} + \{\tau_n^{ms}\}_{\varphi} \sin p\bar{t} \right)\end{aligned}\tag{4.75}$$

The solution for the set of differential equations is given by the induced velocity coefficients as

$$\begin{aligned}\{\bar{\alpha}_n^m\} &= \{\bar{\alpha}_n^m\}_0 + \sum_{p=Q,2Q,3Q,\dots} \left(\{\bar{\alpha}_n^m\}_{\varphi} \cos p\bar{t} + \{\bar{\alpha}_n^m\}_{\varphi} \sin p\bar{t} \right) \\ \{\bar{\beta}_n^m\} &= \{\bar{\beta}_n^m\}_0 + \sum_{p=Q,2Q,3Q,\dots} \left(\{\bar{\beta}_n^m\}_{\varphi} \cos p\bar{t} + \{\bar{\beta}_n^m\}_{\varphi} \sin p\bar{t} \right)\end{aligned}\quad (4.76)$$

where Q is the number of blades, m is the spatial harmonic number of distributions, p is the time-wise harmonic of unsteadiness, $\bar{\alpha}$ are cosine of space, $\bar{\beta}$ terms are sine of space, φ are cosine of time and φ are sine of time.

The solution for the space variables in time can be obtained from the general form the set of differential equations by the use of harmonic balance. The expressions are shown in Equations (4.77) and (4.78).

$$\begin{Bmatrix} \{\bar{\alpha}_n^m\}_{\varphi} \\ \{\bar{\alpha}_n^m\}_{\varphi} \end{Bmatrix} = \frac{1}{2} \begin{bmatrix} [\bar{D}_n^{mc}]^{-1} & -[\bar{D}_n^{mc}]^{-1}[\bar{K}_n^{mc}][\bar{L}^c]\frac{p}{V} \\ \frac{p}{V}[\bar{L}^c][\bar{K}_n^{mc}][\bar{D}_n^{mc}]^{-1} & [\bar{D}_n^{mc}]^{-1} \end{bmatrix} \begin{Bmatrix} \{\tau_n^{mc}\}_{\varphi} \\ \{\tau_n^{mc}\}_{\varphi} \end{Bmatrix} \quad (4.77)$$

$$\text{where } [\bar{D}_n^{mc}] = [\bar{L}^c]^{-1} + \frac{p^2}{V^2} [\bar{K}_n^{mc}][\bar{L}^c][\bar{K}_n^{mc}]$$

$$\begin{Bmatrix} \{\bar{\beta}_n^m\}_{\varphi} \\ \{\bar{\beta}_n^m\}_{\varphi} \end{Bmatrix} = \frac{1}{2} \begin{bmatrix} [\bar{D}_n^{ms}]^{-1} & -[\bar{D}_n^{ms}]^{-1}[\bar{K}_n^{ms}][\bar{L}^s]\frac{p}{V} \\ \frac{p}{V}[\bar{L}^s][\bar{K}_n^{ms}][\bar{D}_n^{ms}]^{-1} & [\bar{D}_n^{ms}]^{-1} \end{bmatrix} \begin{Bmatrix} \{\tau_n^{ms}\}_{\varphi} \\ \{\tau_n^{ms}\}_{\varphi} \end{Bmatrix} \quad (4.78)$$

$$\text{where } [\bar{D}_n^{mc}] = [\bar{L}^c]^{-1} + \frac{p^2}{V^2} [\bar{K}_n^{mc}][\bar{L}^c][\bar{K}_n^{mc}].$$

If instead of an actuator disk, the case considered includes the tilt on the lift, then the apparent mass matrices $\left[\bar{K}_n^{mc}\right]$ and $\left[\bar{K}_n^{ms}\right]$ must be replaced by the corresponding ones using the swirl correction specified in Section 2.6.

The optimization for this case would be to find the pressure coefficients, $\left\{\tau_n^m\right\}_0, \left\{\tau_n^m\right\}_{cp}$ and $\left\{\tau_n^m\right\}_{sp}$ for both cosine and sine that will provide the Goldstein circulation distribution shown in Figures (4.17) and (4.18) and translate these to obtain the figure of merit. The pressure coefficients can be obtained from the optimum circulation distribution given by reference [10] that uses a generalized dynamic wake model with a correction for the swirl. Since it has been proven that finite-state methods are able to provide the Goldstein distribution, the same theory can be used for forward flight with the changes needed to accommodate for the skewed flow conditions.

4.4 Special Case of Hover

The previous results show that Finite-State methods can be used to compute induced power for a rotor in climb. It has been shown that a formal optimization with finite-state models was successfully performed in closed form and that such an optimization recovers the form of solution for all of the classical theories for a lifting rotor under lightly-loaded conditions. That is, it agrees with the Prandtl solution for an actuator disk with a finite

number of blades, with the Betz distribution for a lifting rotor with an infinite number of blades, and with the Goldstein solution for a lifting rotor with a finite number of blades.

According to Betz, the optimum induced flow distribution is one that maintains a constant helix screw angle, ϕ . The induced optimum flow and circulation are nearly identical to what can be obtained from momentum theory and the Prandtl tip correction term, k . The theory of Betz also applies to the case of hover. The power and thrust can be determined from the lift and drag perpendicular and parallel to the vortex sheet, and can be expressed in terms of the lift and drag coefficients respectively. For the optimum rotor, one should find the optimum circulation that will result in the maximum lift-to-drag ratio. If the effect of drag in the vertical direction is neglected, then one can formulate some simple, closed-form results for the lift, power, and thrust in hover of an optimum rotor.

4.4.1. Closed-Form Results in Hover

First of all is to define the geometry of the problem. According to Betz, the optimum induced flow distribution is one that maintains a constant helix screw angle, ϕ . Thus, for optimum performance:

$$w = w_0 \cos \phi \quad (4.79)$$

$$\cos \phi = \frac{\Omega x}{\sqrt{\Omega^2 x^2 + (V + w_0)^2}} \quad (4.80)$$

$$\sin \phi = \frac{V + w_0}{\sqrt{\Omega^2 x^2 + (V + w_0)^2}} \quad (4.81)$$

$$w = \frac{w_0 \Omega x}{\sqrt{\Omega^2 x^2 + (V + w_0)^2}} \quad (4.82)$$

where w_0 is a nominal value chosen to obtain a given thrust for a given rotor radius and rotational speed. The induced flow normal to the disk w_N and the swirl induced flow w_s are given by:

$$w_N = w_0 \cos^2 \phi = \frac{w_0 \Omega^2 x^2}{\Omega^2 x^2 + (V + w_0)^2} \quad (4.83)$$

$$w_s = w_0 \cos \phi \sin \phi = \frac{w_0 (V + w_0) \Omega x}{\Omega^2 x^2 + (V + w_0)^2} \quad (4.84)$$

Induced Flow computation

Due to the Betz geometry of similar triangles (and the fact that w is always perpendicular to the vortex sheet, the following are alternative representations to the relationships in Equations (4.80) and (4.81) of cosine and sine of the sheet angle.

$$\sin \phi = \frac{V + w_0 \cos \phi}{\sqrt{(\Omega x - w_0 \cos \phi \sin \phi)^2 + (V + w_0 \cos^2 \phi)^2}} \quad (4.85)$$

$$\cos \phi = \frac{\Omega x + w_0 \cos \phi \sin \phi}{\sqrt{(\Omega x - w_0 \cos \phi \sin \phi)^2 + (V + w_0 \cos^2 \phi)^2}} \quad (4.86)$$

In some situations, the above are more convenient.

The induced flow and circulation can be determined from momentum theory, the lift, and the Prandtl tip correction term, k .

$$Q_L = Q \rho \Gamma \left(\frac{\Omega x - w_0 \cos \phi \sin \phi}{\cos \phi} \right) = 4\pi k x Q w_0 \cos \phi (V + w_0 \cos^2 \phi) \quad (4.87)$$

Equation (4.87) implies that,

$$L = \frac{4\pi k x \rho w_0 \cos \phi}{Q} (V + w_0 \cos^2 \phi) \quad (4.88)$$

$$L = \frac{4\pi k x \rho w_0 \cos^2 \phi}{Q} \cdot \frac{V + w_0 \cos^2 \phi}{\Omega x - w_0 \cos \phi \sin \phi} \quad (4.89)$$

After substitution of the geometrical formulas for $\cos \phi$ and $\sin \phi$, one obtains

$$L = \frac{4\pi k \rho w_0}{\Omega Q} \cdot \frac{V + w_0 \Omega^2 x^2}{\Omega^2 x^2 + (V + w_0)^2} \cdot \frac{\Omega^2 x^2}{\sqrt{\Omega^2 x^2 + (V + w_0)^2}} \quad (4.90)$$

$$L = \frac{4\pi k w_0}{\Omega Q} \cdot \frac{V + w_0 \Omega^2 x^2}{\Omega^2 x^2 + (V + w_0)^2} \cdot \frac{\Omega^2 x^2}{\Omega^2 x^2 + V(V + w_0)} \quad (4.91)$$

For lightly-loaded rotors (i.e., $w_0 \ll V$), the above formulas revert to the Goldstein relationships.

$$L = \frac{4\pi k \rho (\Omega x) V w_0 \cos \phi}{\Omega Q} \quad (4.92)$$

$$L = \frac{4\pi k V w_0 \cos^2 \phi}{\Omega Q} \quad (4.93)$$

For the case of hover, $V=0$, the relationships become:

$$L = \frac{4\pi k \rho (\Omega x) w_0^2 \cos^3 \phi}{\Omega Q} = \frac{4\pi k \rho w_0^2}{\Omega Q} \cdot \frac{\Omega^4 x^4}{(\Omega^2 x^2 + w_0^2)^{3/2}} \quad (4.94)$$

$$L = \frac{4\pi k \rho w_0^2}{\Omega Q} \cdot \frac{\Omega^2 x^2}{\Omega^2 x^2 + w_0^2} \quad (4.95)$$

These, then, form the basis of an efficient propeller design.

Power and Thrust

The power and thrust can be determined from the lift and drag perpendicular to and parallel to the vortex sheet. The lift and drag on each blade can be expressed in terms of the lift coefficient and drag coefficient.

$$L = \frac{\rho c}{2} \left[\left(\Omega x - w_0 \cos \phi \sin \phi \right)^2 + \left(V + w_0 \cos^2 \phi \right)^2 \right] C_L \quad (4.96)$$

$$D = \frac{\rho c}{2} \left[\left(\Omega x - w_0 \cos \phi \sin \phi \right)^2 + \left(V + w_0 \cos^2 \phi \right)^2 \right] C_D \quad (4.97)$$

The thrust and power arise from the geometry of the vortex angle.

$$T = Q [L \cos \phi - D \sin \phi] \quad (4.98)$$

$$P = Q (\Omega x) [L \sin \phi + D \cos \phi] \quad (4.99)$$

We assume that the angle of attack at each radial station has been chosen to give the best C_L/C_D and that the chord has then been chosen to give the ideal inflow.

$$v = \frac{v_0}{\sqrt{r^2 + v_0^2}} \quad (4.100)$$

where r is the radial position.

First, the integral of the thrust results in a relationship between C_T and inflow ratio, v_0 .

$$C_T = 2v_0^2 B^2 \left[1 - 2v_0^2 \ln \left(1 + \frac{1}{v_0^2} \right) + \frac{v_0^2}{(1 + v_0^2)} \right] \quad (4.101)$$

where

$$B = 1 - \frac{2\ln(2)v_0}{Q\sqrt{1+v_0^2}} \quad (4.102)$$

From the above, one can find (for any given C_T) the appropriate v_0 for that desired thrust.

Note that we have included the tip-loss correction in terms of v_0 .

Similarly, the total power coefficient (including profile power) can be done in closed form

based on the equation for the power, which shows that the profile power must be $\frac{C_L}{C_D} \cot \phi$

times the induced power. Thus, we have (after integration in closed form) for hover:

$$C_p = 2v_0^3 B^2 \left[1 - 2v_0^2 \ln \left(1 + \frac{1}{v_0^2} \right) + \frac{v_0^2}{(1+v_0^2)} \right] + \frac{2}{3} v_0^2 B^3 \frac{C_D}{C_L} \left[\frac{2 - 10v_0^2 - 15v_0^4}{1+v_0^2} + 15v_0^3 \arctan \left(\frac{1}{v_0} \right) \right] \quad (4.103)$$

Note that, because this is an optimum rotor, v_0 is controlled by chord. Thus, as v_0 goes to zero, the chord and profile power also go to zero. The figure of merit can be obtained from

the above equations as $\frac{C_T^{3/2}}{\sqrt{2}C_p}$. For induced power only, this reduces to:

$$\text{Hover F.M.} = B \left[1 - 2v_0^2 \ln \left(1 + \frac{1}{v_0^2} \right) + \frac{v_0^2}{1+v_0^2} \right]^{1/2} \quad (4.104)$$

This is very close to (but not identical to) the climb figure of merit.

$$\text{Climb F.M.} = B^2 \left[1 - \lambda^2 \ln \left(1 + \frac{1}{\lambda^2} \right) \right] \quad (4.105)$$

where the tip loss factor, B , is expressed in terms of the non-dimensional climb rate, λ .

Equations for C_T and C_P imply an optimum chord (i.e., optimum solidity) for maximum Figure of Merit. For small v_0 , the profile power dominates; and Figure of Merit goes to zero. For large v_0 , the log term causes the Figure of Merit to decay as $1/v_0^2$. Thus, there is an optimum thrust, v_0 , chord, and solidity for any lift-to-drag ratio.

As stated previously, for the optimum rotor, one should find the combination of angle of attack or blowing that will result in the maximum C_L/C_D . The expression for optimum drag-to-lift ratio is:

$$\frac{C_D}{C_L} = \frac{3}{2} \left[\frac{2 \ln 2 \frac{v_0^2}{Q} + 4v_0^3 \ln \left(\frac{1}{v_0} \right) - 2v_0^3}{1 - 6v_0^2 \ln \left(\frac{1}{v_0} \right) + 6v_0^2} \right] \quad (4.106)$$

The use of this expression for a particular airfoil will yield a maximum drag-to-lift ratio.

4.4.2. Example Calculation

Results were obtained for an optimum propeller in hover. The results are shown for the case of infinite number of blades and for a propeller with four blades. Of importance is the plot of figure of merit variation with thrust coefficient shown. The figure of merit decreases for higher thrust coefficient, and the effect of finite number of blades can be seen in Figure 4.59.

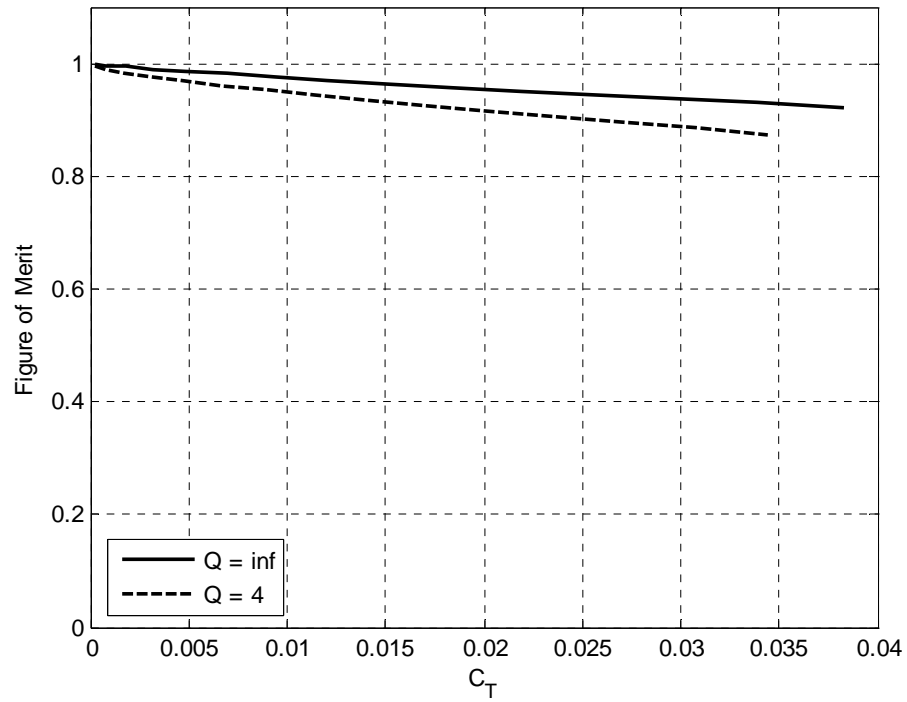


Figure 4.59: Figure of merit variation with thrust coefficient in hover (no induced drag).

Figure 4.59 shows the case where the effect of C_D has been neglected. Figure 4.60 shows the same graph for a specific NACA 0012 airfoil with a lift-to-drag ratio of 22, for which the effect of the drag coefficient is considered. It is seen that there is an optimum value for the thrust.

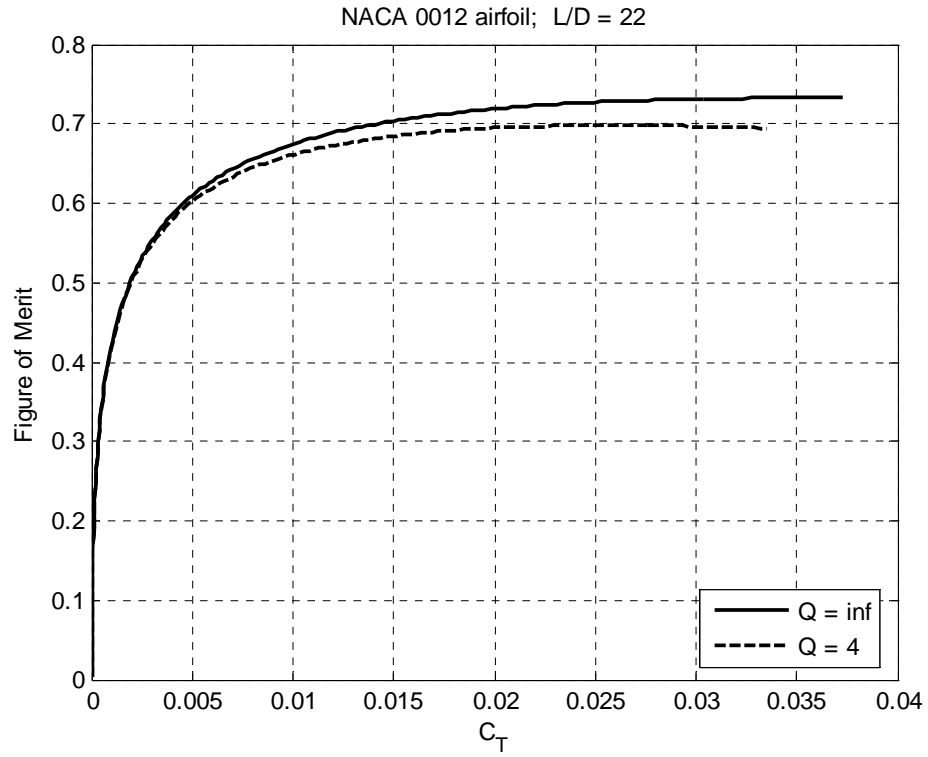


Figure 4.60: Figure of merit variation with thrust coefficient for a NACA 0012 airfoil.

The optimum Figure of Merit for different drag-to-lift ratios is shown in Figure 4.61.

As it has been shown, different quantities can be plotted to determine different aspects of the optimum rotor, such as the optimal inflow ratio for different drag-to-lift ratios. Moreover, if a specific airfoil configuration is provided, results can be shown for the specific case in climb and in hover conditions.

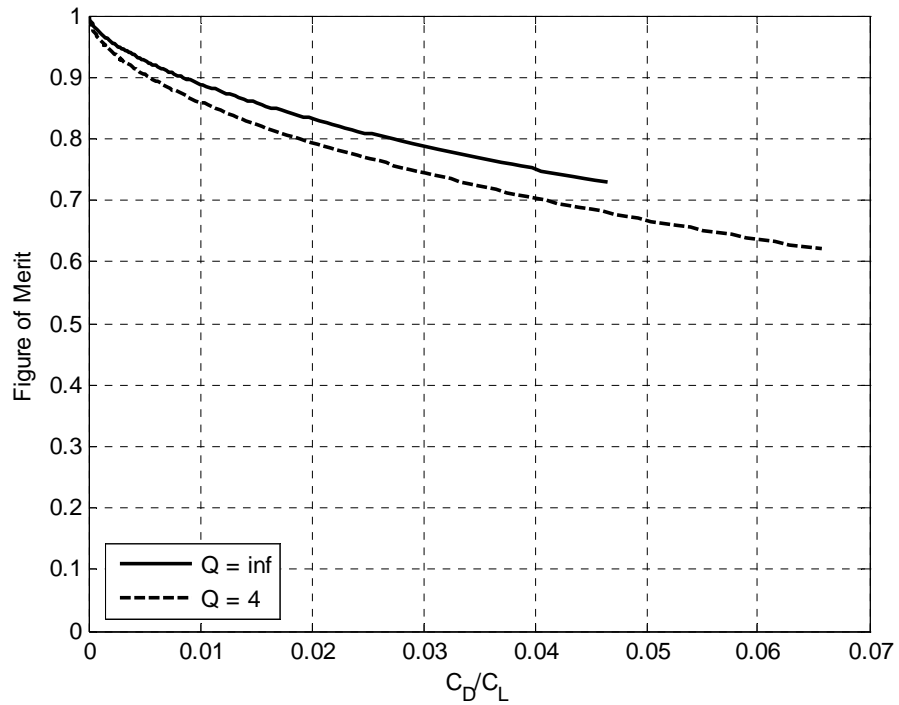


Figure 4.61: Optimum figure of merit change with drag-to-lift ratio effect.

The above shows how to design an optimum rotor (including the effects of lift tilt, tip loss and profile power) with a special case in closed form for hover. The best possible figure of merit is far below 1.0 but is still larger than is being obtained today.

Betz geometry was used to obtain power and thrust for a helicopter rotor and applied to the special case of hover. The result is a closed-form of the figure of merit that can be used to determine how the performance is affected by different conditions (finite number of blades, lift-to-drag ratio, etc.).

Chapter 5

Summary, Conclusions and Future Work

5.1 Summary and Conclusions

This dissertation shows various configurations can be studied for induced power calculations using Finite-state methods. The development of the solution is based on the need to achieve optimum induced power, therefore the optimization is set up to achieve this. However, the way in which the optimization is performed allows for different optimizations to be studied. Optimum pressure coefficients are obtained for the minimum induced power distribution. However, this could be changed to optimize for different situations. For example, if the need to optimize arises for a particular blade shape with concrete dimensions, the vector containing the influence coefficients can be modified to include the particular characteristics of the blade. Once the theory has been derived, many other cases can be studied using the same concepts. In a similar manner, the process can also be altered for conditions other than that the thrust must remain a constant, providing different results.

The results show enough information in axial flow for a finite number of blades to help in the determination of how exactly a finite number of blades affects the increase of induced

power. For this reason, study of the cases in forward flight (skewed flow) for a finite number of blades is unnecessary at this point. The theory has been developed for this particular case, but no results have been computed. In the future, some results for figure of merit or induced power coefficient calculations could be shown for the sake of completeness.

A complete inflow theory is developed to describe the flow in all regions around the rotor. Previous cases for regions above and on the rotor disk become particular solutions of this general formulation. The theory is then applied for the case of a quadratic optimization of power for a constant thrust. The optimization enables for the figure of merit, or efficiency of the rotor, to be found. The figure of merit is shown to be considerably less than the ideal (unity) for various cases, by the calculation of optimum pressure and induced velocity distributions at various skew angles, increasing tilt and advance ratio. The solutions validate the theory for axial flow when compared to classical results. In addition, it provides a formulation to use for ideal and real lightly-loaded rotors in forward flight. It is found that the figure of merit decreases with advance and tilt due to the downwash on inflow present primarily on and around the reversed-flow region.

The solution for the optimal pressure coefficients is performed and the values, along with the graphical representation of pressure and induced velocity distributions show that the solution is trimmed forward to aft on the rotor but that it is not trimmed sideways.

5.2 Future Work

5.2.1 Theory

Once the theory has been developed, many applications can be derived from the complete formulation. The most direct line of work that could be developed from the theory is to apply it to obtain results to see how the formulation can be validated for the region below the disk. Also with the complete formulation, many more applications can be analyzed. The complete theory can be implemented into computer programs and applied for rotor-body interactions, ground effect, noise reduction, etc.

Another direct application of the current theory would be to apply the complete inflow theory to in forward flight for a finite number of blades and see how the number of blades affect induced power and efficiency in forward flight.

Different computer-based optimizations could be used and introduced into a CFD (Computational Fluid Dynamics) environment to obtain results for various configurations. CFD provides a more accurate de description of the flow, but it is time consuming and cannot be implemented for real-time simulations. There are many other computer applications and comprehensive codes, such as RCAS and CAMRAD (I and II), simulation codes such as FLIGHTLAB, etc., that would benefit from the incorporation of the provided theory to apply to rotors with specific characteristics.

The theory could also be included into comprehensive codes to apply to real rotors and blades and see how the figure of merit and, most importantly, the induced power are affected and what changes would be needed to improve the efficiency of blade configurations used currently.

5.2.2 Optimization

Future work in optimization could apply the methodology to various constraints that improved structural hardware. That work could then determine how much figure of merit be improved by various devices.

Also on optimization, the optimal pressure coefficients could be constrained to obtain the trimmed solution.

Appendix A

Ellipsoidal Coordinate System

The ellipsoidal coordinate system $(\nu, \eta, \bar{\psi})$ is used in the dynamic wake model because it is convenient to express the boundary conditions for the problem in this system. Additionally, a solution by the use of separation of variables for the Laplace equation takes the form of Legendre's associated differential equation. The solution to the separated equations is easily recognized and applied.

The ellipsoidal coordinate system is defined as

$$x = -\sqrt{1-\nu^2}\sqrt{1+\eta^2}\cos\bar{\psi} \quad (\text{A.1})$$

$$y = \sqrt{1-\nu^2}\sqrt{1+\eta^2}\sin\bar{\psi} \quad (\text{A.2})$$

$$z = -\nu\eta \quad (\text{A.3})$$

where

$$-1 \leq \nu \leq +1 \quad (\text{A.4})$$

$$0 \leq \eta \leq \infty \quad (\text{A.5})$$

$$0 \leq \bar{\psi} \leq 2\pi \quad (\text{A.6})$$

Figure A.1 shows the coordinate system viewed in the xz plane with the outline of contours for some ν and η values.

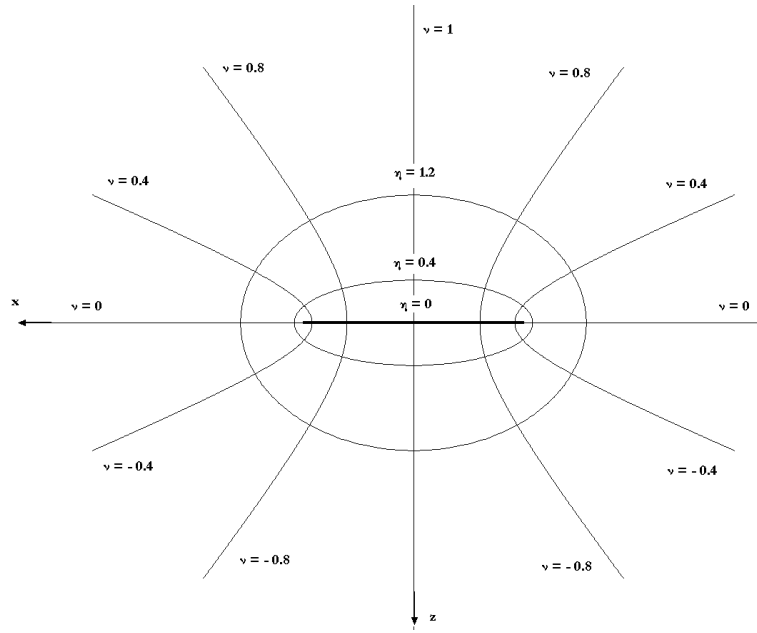


Figure A.1: Ellipsoidal Coordinate System, xz-plane view.

Examples of the contours of three dimensional plots for given values of η and ν are shown on Figures A.2 and A.3. Figure A.2 shows the contour for a fixed η of 0.4. Figure A.3 is the contour on a three dimensional plot for a ν of 0.8.

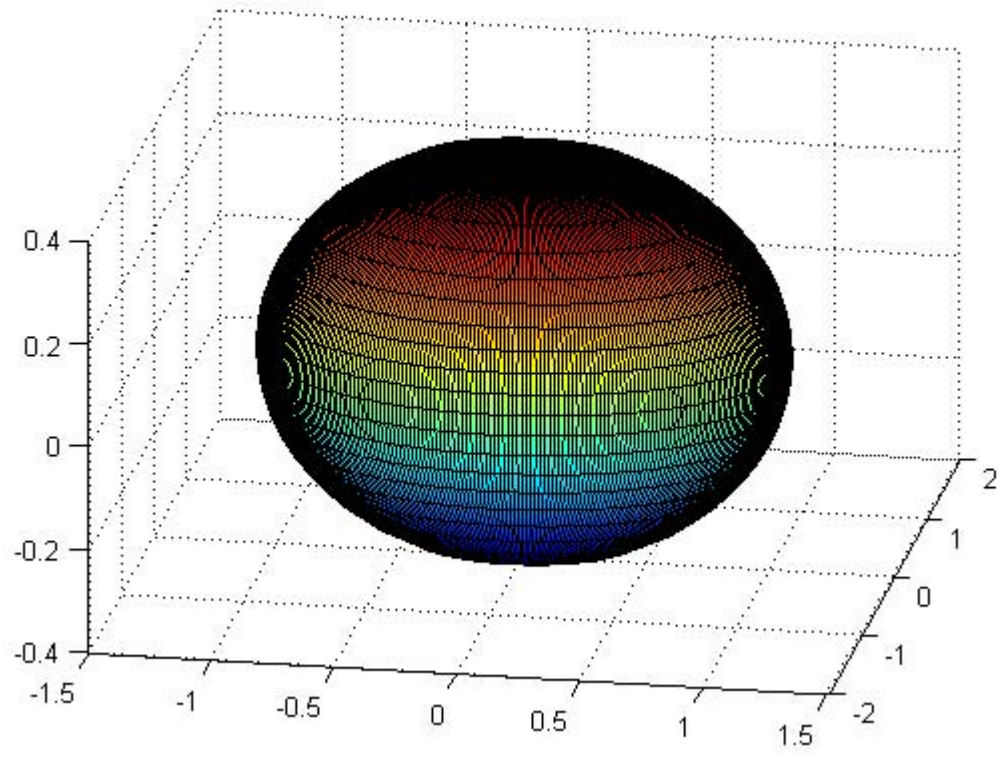


Figure A.2: Ellipsoidal Coordinate System Contour, $\eta = 0.4$, all ν , all $\bar{\psi}$

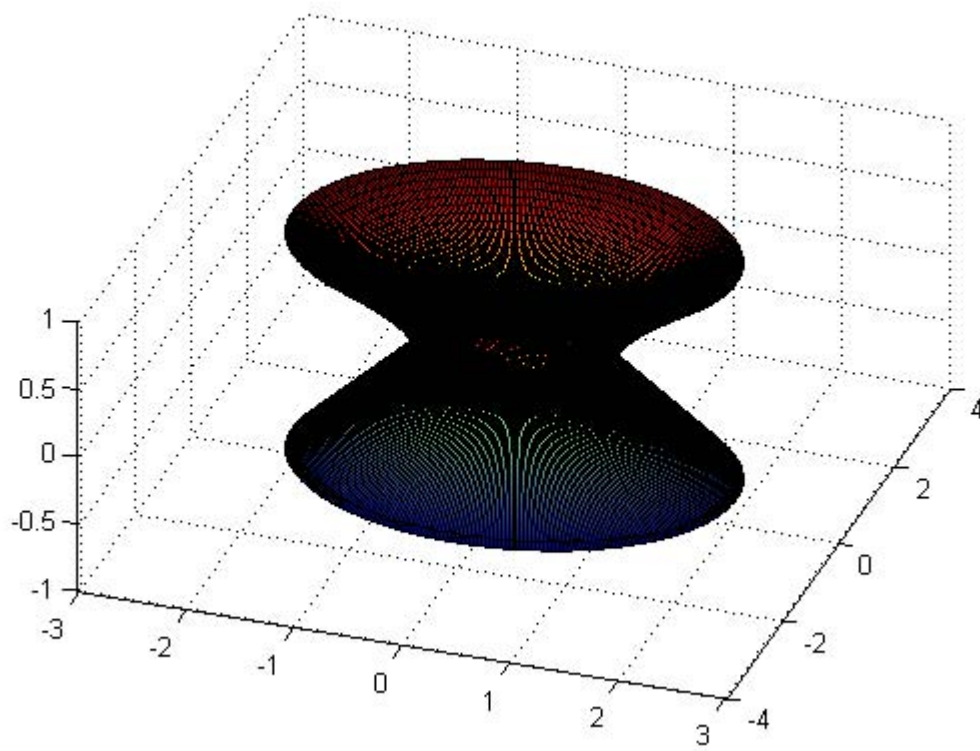


Figure A.2: Ellipsoidal Coordinate System Contour, $\nu = 0.4$ for $\varkappa \leq 0$, $\nu = -0.4$ for $\varkappa \geq 0$, all η , all $\bar{\psi}$

Appendix B

Normalized Associated Legendre Functions

Laplace's equation is

$$\nabla^2 \Phi = 0 \quad (\text{B.1})$$

Expressed in the ellipsoidal coordinate system $(\nu, \eta, \bar{\psi})$ becomes

$$\frac{\partial}{\partial \nu} \left[(1 - \nu^2) \frac{\partial \Phi}{\partial \nu} \right] + \frac{\partial}{\partial \eta} \left[(1 + \eta^2) \frac{\partial \Phi}{\partial \eta} \right] + \frac{\partial}{\partial \bar{\psi}} \left[\frac{(\nu^2 + \eta^2)}{(1 - \nu^2)(1 + \eta^2)} \frac{\partial \Phi}{\partial \bar{\psi}} \right] = 0 \quad (\text{B.2})$$

Equation (B.3) shows the separation of variables used to solve the partial differential equation of Equation (B.2)

$$\Phi(\eta, \nu, \bar{\psi}) = \Phi_1(\eta) \Phi_2(\nu) \Phi_3(\bar{\psi}) \quad (\text{B.3})$$

Substituting Equation (B.3) into (B.2) and separating the variables

$$\frac{d}{d\nu} \left[(1 - \nu^2) \frac{d\Phi_1}{d\nu} \right] + \left[-\frac{m^2}{1 - \nu^2} + n(n+1) \right] \Phi_1 = 0 \quad (\text{B.4})$$

$$\frac{d}{d\eta} \left[(1 + \eta^2) \frac{d\Phi_2}{d\eta} \right] + \left[\frac{m^2}{1 + \eta^2} - n(n+1) \right] \Phi_2 = 0 \quad (\text{B.5})$$

$$\frac{d^3 \Phi_3}{d\bar{\psi}} + m^2 \Phi_3 = 0 \quad (\text{B.6})$$

where m and n are separation constants.

Equations (B.4) and (B.5) are forms of the associated Legendre differential equations, and the associated Legendre functions of the first and second kind are solutions for Equations (B.4) and (B.5) respectively.

The associated Legendre function of the first kind is

$$P_n^m(\nu) = (1 - \nu^2)^{\frac{m}{2}} \frac{d^m}{d\nu^m} \sum_{k=0}^K (-1)^k \frac{(2n - 2k)!}{2^n k! (n - k)! (n - 2k)!} \nu^{n-2k} \quad (\text{B.7})$$

The normalized associated Legendre function of the first kind defined by Equation (B.8) is used throughout this dissertation because it provides a complete set of functions that can be used to expand the pressure and induced flow velocity distributions radially.

$$\bar{P}_n^m(\nu) = (-1)^m \frac{P_n^m(\nu)}{\rho_n^m} \quad (\text{B.8})$$

where $\rho_n^m = \sqrt{\frac{1}{2n+1} \frac{(n+m)!}{(n-m)!}}$.

The normalized associated Legendre function of the second kind, $\bar{Q}_n^m(i\eta)$, is explained more in detail in Ref. 2 and 3. Equation (B.9) shows the relationship between the associated and the normalized associated functions.

$$\bar{Q}_n^m(i\eta) = \frac{Q_n^m(i\eta)}{Q(i0)} \quad (\text{B.9})$$

Appendix C

General Galerkin Method

The Galerkin method, also known as the method of weighted residuals, is an approximate method to find the solution of a differential equation.

Given a differential equation, $L(u)=f$, on a domain D , with initial and boundary conditions, one can find an approximate solution, u_a , that will be dependent on x and t and has an expression:

$$u_a(\vec{x}, t) = \sum_{j=1}^N a_j(t) \phi_j(x) \quad (C.1)$$

where the ϕ_j 's are the shape functions, which are a complete set of predetermined functions that have to be chosen. They are also called trial functions and must be a linearly independent set of functions and must satisfy the boundary conditions and the initial conditions if any are present. The goal is then to determine the parameters a_j .

The approximate solution is then introduced into the differential equation. Because the solution is not exact, there is an error in the approximation that has to be found. The error is called a residual and can be seen in Equation (C.2). It is important to reduce the residual, for this, the error is minimized by multiplying the residual by some test functions, w_k , and then it is integrated over the domain, D .

$$R = L(u_a) - f \quad (C.2)$$

$$\iint_D w_k L(u_a) dD = \iint_D w_k f dD \quad (C.3)$$

The type of test, or also called weighting, functions depends on the approximation that is needed. There are different types of approximations that depend on what is satisfied. For all of the cases, the weighting functions are set to be equal to the shape functions.

$$w_k(x) = \phi_k(x) \quad (C.4)$$

Substituting Equation (C.1) into (C.3) yields an expression that provides the a_j coefficients.

$$\sum_{j=1}^N \left[\iint_D w_k L(\phi_j) dD \right] a_j = \iint_D w_k f dD \quad (C.5)$$

where N is the fewest number of members needed for a complete set of functions.

Appendix D

Transformation Matrices in Closed Form

The closed form expressions for the transformation matrices were obtained by Ref. 7.

The definition of the transformation matrix $\left[B_{jn}^r \right]$ comes from the solution for the induced flow expansion coefficients in the general set of differential equations that define the combined He theory (Eqs. 3.9 and 3.10). The definition for the transformation matrix is given in general form by:

$$B_{jn}^r \equiv \int_0^1 \bar{P}_j^r(\nu) \Psi_n^r(\bar{r}) d\nu \quad (D.1)$$

let $\Psi_n^r = \frac{1}{\nu} \bar{P}_n^r(\nu)$ and a closed form expression for the matrix is:

$$B_{jn}^r = \bar{B}_{jn}^r = (-1)^{\frac{n+j-2r-2}{2}} \sqrt{\frac{H_j^r}{H_n^r}} \sqrt{2n+1} \sqrt{2j+1} \sum_{q=r, r+2, \dots}^{j-1} H_q^r \frac{(2q+1)}{(n-q)(n+q+1)} \quad (D.2)$$

The formula often used is the one for a special case of the inverse, since the expression for B_{jn}^r requires more work.

$$\bar{A}_{jn}^r \equiv \left[B_{jn}^r \right]^{-1} = \frac{(-1)^{\frac{n+j-2r}{2}}}{\sqrt{H_n^r H_j^r}} \frac{2\sqrt{2n+1} \sqrt{2j+1}}{(n+j)(n+j+2) \left[(n-j)^2 - 1 \right]} \quad (D.3)$$

and A_{jn}^r is identical to \bar{A}_{jn}^r for the special case $\Psi_j^r = \bar{P}_j^r(\nu)$

Note that $\left[\bar{A} \right] = \left[\bar{B} \right]^{-1}$ only when n and j go to infinity.

Appendix E

Table Method

In order to compute the induced flow using the generalized dynamic wake model in Reference 2, one must define the number of harmonics chosen to expand the induced velocity. The number of harmonics is chosen based on the highest dynamic frequency of interest for any given case. This number provides the highest power or \bar{r} shown in Table E.1. The truncation for the number of radial shapes is given also in this table, and depends on the highest power of \bar{r} for the problem.

HIGHEST POWER OF \bar{r}	M						TOTAL INFLOW STATES
	0	1	2	3	4	5	
0	1						1
1	1	1					3
2	2	1	1				6
3	2	2	1	1			10
4	3	2	2	1	1		15
5	3	3	2	2	1	1	21

Table E.1: Choice of the Number of Spatial Modes (n+m=odd)

For example, if the highest power of \bar{r} is 3, then we will have three harmonics ($m_{\max} = 3$). The zero harmonic ($m=0$), will have two inflow states, the first harmonic ($m=1$) will have 2 terms but four inflow states (two for the cosine terms and two for the sine terms), the second harmonic ($m=2$) will have 1 term that corresponds to two inflow states, and so on. The total number of inflow states for this example will be 10.

A more detailed explanation on the choice of number of inflow states to be used for a study is given in References [2] and [3].

In order to determine the number of inflow states needed to obtain accurate results for the present research, the figure of merit for different number of harmonics was obtained. Table E.2 and Figures E.1 and E.2 show the values of figure of merit for the simplest case. That is, an actuator disk (no tilt) with an infinite number of blades in axial flow ($\chi = 0^\circ$). The ideal figure of merit is 1.0. However this number is only achieved as the number of terms approaches infinity.

Table E.2 shows that the value of figure of merit for a case with ten harmonics (highest power of \bar{r}) is sufficiently close to the ideal. Therefore, it can be assumed that the use of ten harmonics will achieve accurate results. Twenty harmonics provides a better figure of merit result, but the increase in computational time might not be worth the degree of additional accuracy. The number of harmonics used in this research is twenty. This statement contradicts the previous assumption of accuracy to be enough with ten harmonics, but since this is the first attempt to obtain results for skewed flow using finite-state methods, results were obtained with the greatest accuracy possible. However, in future calculations

the number of harmonics could be reduced to ten with no perceivable impact on the outcome results.

HIGHEST POWER OF \bar{r}	FIGURE OF MERIT
0	0.8889
1	0.8889
3	0.9600
6	0.9877
10	0.9941
20	0.9981

Table E.2: Figure of Merit for various Number of Harmonics

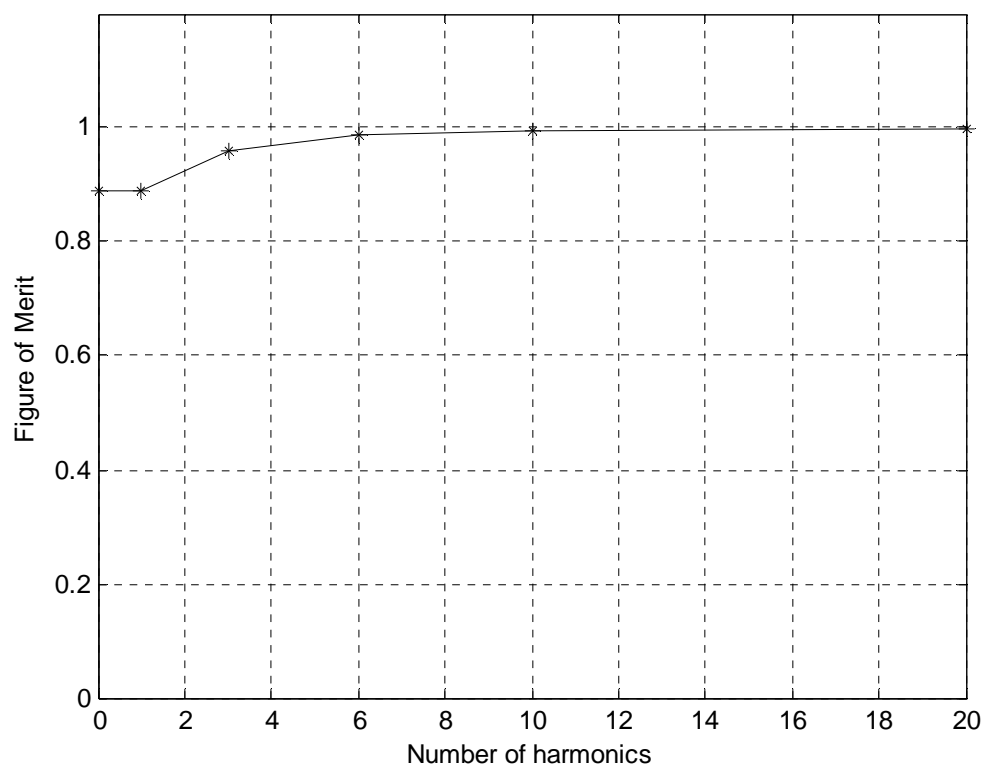


Figure E.1: Figure of Merit for Different Number of Harmonics.

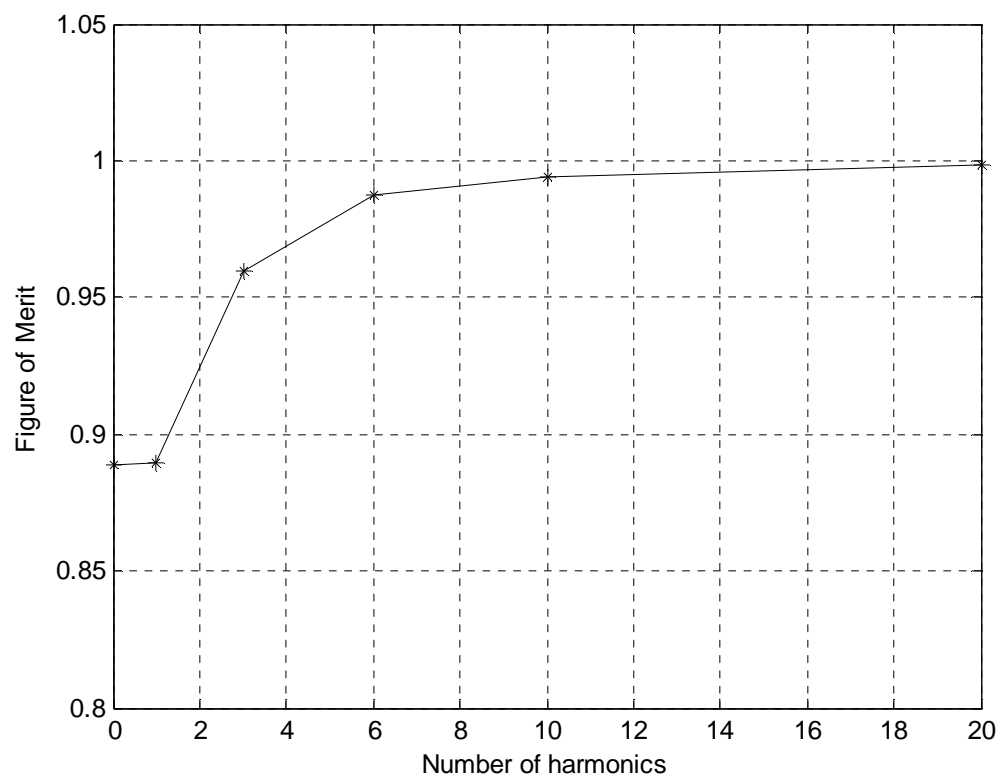


Figure E.2: Close-up of Figure of Merit versus the Number of Harmonics.

Appendix F

Influence Coefficients as a Fit of $\cos\varphi$

The influence coefficient vector, $\{C_n^m\}$, are a Legendre-function representation of $\cos\varphi$ which is the loss of thrust due to the tilt of the lift vector. Once more, they are defined as:

$$C_n^0 = \frac{1}{2\pi} \int_0^{2\pi} \int_0^1 \cos\varphi \bar{P}_n^0(v) v dv d\psi \quad (\text{F.1})$$

$$C_n^{mc} = \frac{1}{\pi} \int_0^{2\pi} \int_0^1 \cos\varphi \bar{P}_n^m(v) v dv \cos(m\psi) d\psi \quad (\text{F.2})$$

$$C_n^{ms} = \frac{1}{\pi} \int_0^{2\pi} \int_0^1 \cos\varphi \bar{P}_n^m(v) v dv \sin(m\psi) d\psi \quad (\text{F.3})$$

where

$$\cos\varphi = \frac{r + \mu \sin\psi}{\sqrt{(r + \mu \sin\psi)^2 + \lambda^2}} \quad (\text{F.4})$$

for a lightly-loaded rotor.

Then, the relationship between the coefficients and the function $\cos\varphi$ (cosine of the tilt angle) becomes:

$$\cos\varphi = \sum_n 2C_n^0 \frac{1}{v} \bar{P}_n^0(v) + \sum_{m,n} \frac{1}{v} \bar{P}_n^m(v) [C_n^{mc} \cos(m\psi) + C_n^{ms} \sin(m\psi)] \quad (\text{F.5})$$

This should be true for all skew angles, climb and advance conditions, and azimuthal locations on the rotor. To prove that this is actually the case, the distributions are plotted and compared. Figure F.1 shows the distribution for a random case using the expression for the cosine of the tilt in Equation (F.4). Figure F.2 shows the same distribution for a random case but using the right-hand side of Equation (F.5) (i.e., influence coefficient and Legendre functions expansion). Both of them have the same basic shape and dimensional values. However, the use of the coefficients does not quite match the close-form distribution, as it is shown in Figure F.3.

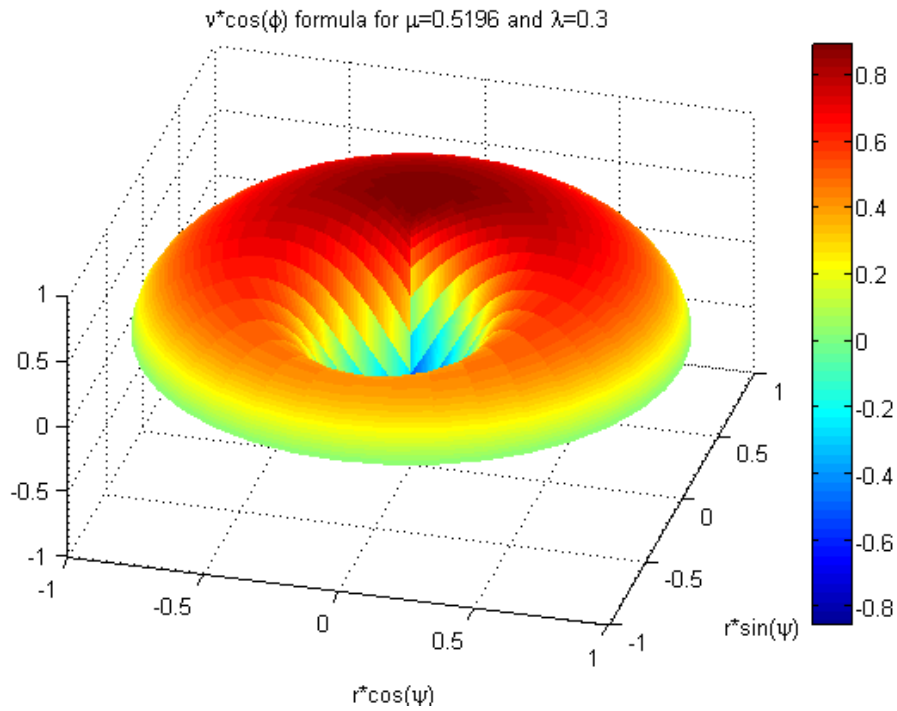


Figure F.1: $v \cos\phi$ Distribution to be fitted by Legendre-function representation.

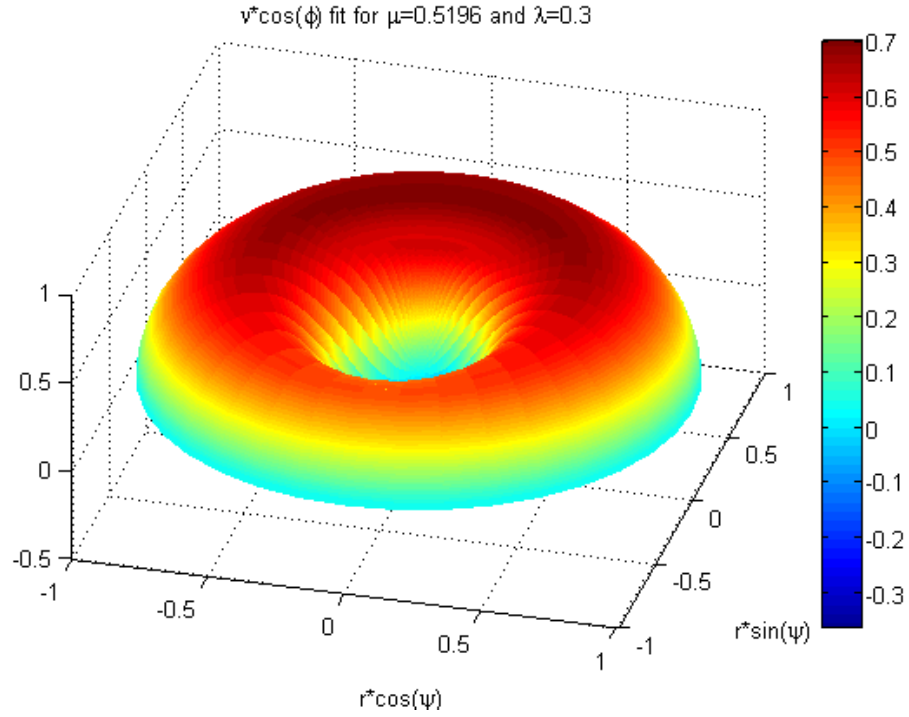


Figure F.2: Legendre-function Representation of $v \cos \phi$.

Figure F.3 shows different views for both a) $\cos \phi$ formula and b) Legendre-function representation. The top (or XY) view shows agreement, but differences are more perceptible when the side views are considered. Figures F.3a.3 and F.3b.3 in particular, show the tendency of the Legendre-function representation (F.3b.3) to mimic the $\cos \phi$ distribution (F.3a.3). The main difference is the fact that Figure (F.3a.3) has a singularity for $r=0$, whereas its Legendre-function counterpart does not. The Legendre-function representation is trying to introduce the singularity, but the number of terms used for the influence coefficient vector definition is not enough to obtain the effect. Twenty harmonics (231 inflow stated by the table method in Appendix E) were used, which has been proven sufficient to obtain induced power and figure of merit calculations along this dissertation. Therefore, although the Legendre-function representation shows slight disagreement with

what would be thrust lost due to the swirl velocity induced by the tilt on the lift for these many terms, an addition of a large amount of terms would be necessary to attain a closer fit but would not provide considerable increased accuracy for neither figure of merit nor induced power calculations. The provided results are for a skew angle, χ , of 60° and $v=0.6$, which results on a tilt, λ , of 0.3 and an advance ratio, μ , of 0.5196. Other cases were analyzed and the same conclusions could be drawn.

Finally, Figures F.4 through F.6 show excerpts from Figures F.1 and F.2 for specific azimuthal locations (specific ψ angle) around the rotor. The figures shown correspond to $\psi=10^\circ$ and 190° for Figure F.4, $\psi=60^\circ$ and 240° for Figure F.5, and $\psi=120^\circ$ and 300° for Figure F.6. The solid lines represent the cosine of the tilt equation and the dotted lines are the Legendre-function fit representation for all radial positions. Figure F.7 is a sketch of the rotor viewed from above. To understand what is happening and why the fit for some of these distributions differs from the close-form of $\cos\varphi$ we find the location of Figures F.4, F.5 and F.6 on Figure F.7. Figure F.4 corresponds to the distribution on the crossing solid line on Figure F.7 approximately. The differences are mostly present on the vicinity of root of the rotor ($r=0$) since there is a discontinuity present. The rest of the points across the rotor are adequately satisfied by the Legendre-function representation. Figure F.5 corresponds to the distribution on the crossing dashed line on Figure F.7 approximately. Differences are greater in this figure because the distribution crosses the area of reversed flow.

The reversed-flow area is a region on the rotor where the flow is reversed. This means that the total velocity of the flow is negative (that is, the flow has a tendency to move on the opposite direction). The area of reversed flow is created by the direction of the resulting total velocity (U_T) at a given point. The incoming velocity seen by the blades in the rotor ($U \sin \psi$) is added to the velocity of the individual blades (Ωx). For $180^\circ < \psi < 360^\circ$ the incoming value of the flow velocity is negative. Therefore, if $U \sin \psi > \Omega x$ for a given location x ($0 \leq x \leq 1$), the direction of the total velocity is negative (reversed flow). To see where these locations are in the rotor-frame

Figure F.6 corresponds to the distribution on the crossing dotted line on Figure F.7 approximately. This location passes through the complete reversed-flow region. This is the reason why the fit shows the most discrepancies.

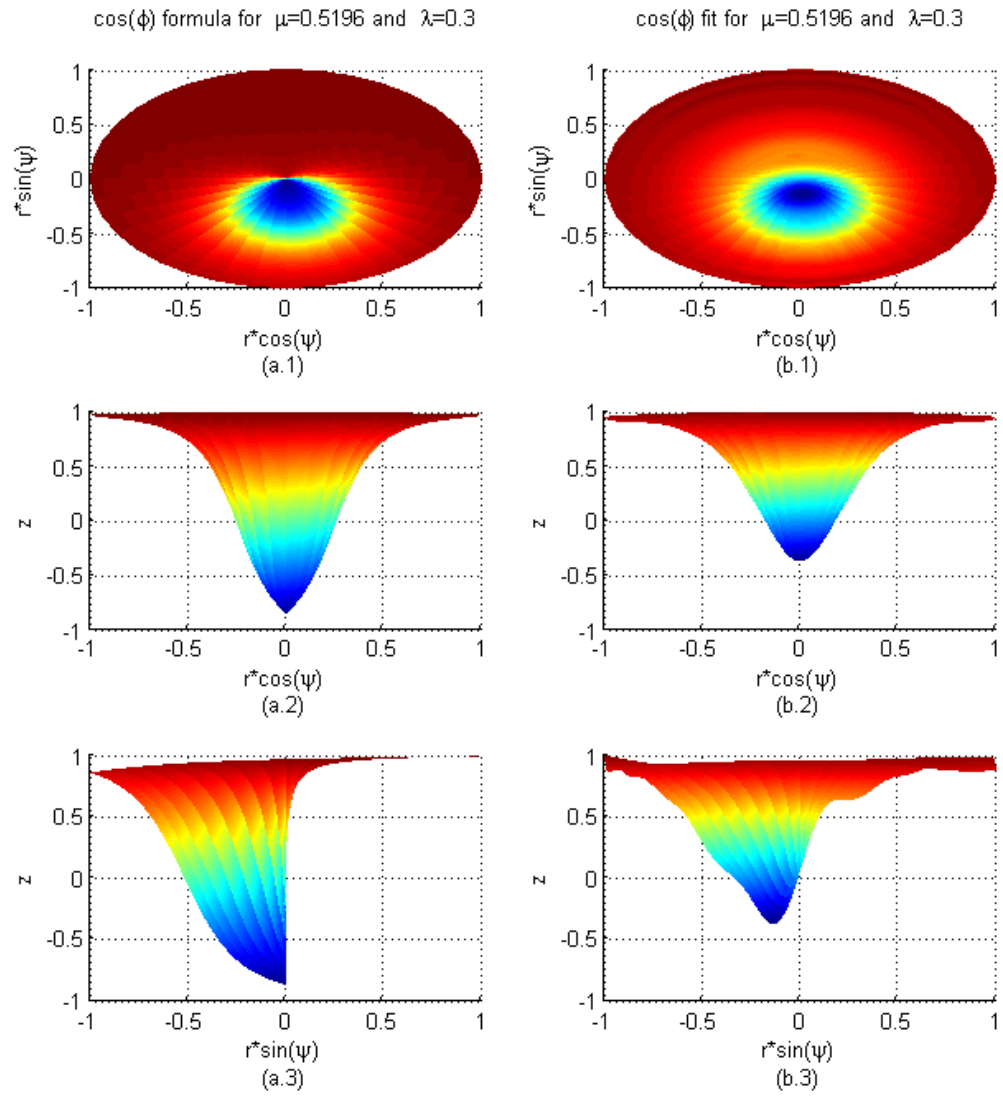


Figure F.3: Top and side views for: a) $\cos\varphi$ Formula and b) Influence Legendre-function representation of $\cos\varphi$.

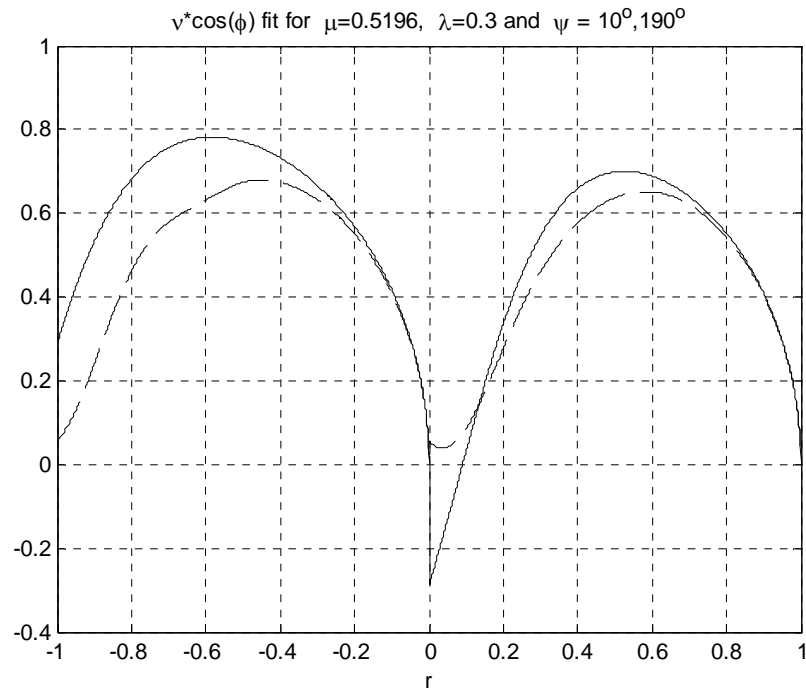


Figure F.4: $\text{Cos}(\varphi)$ fit for $\mu=0.5196$, $\lambda=0.3$, $\psi=10$ and 190° .

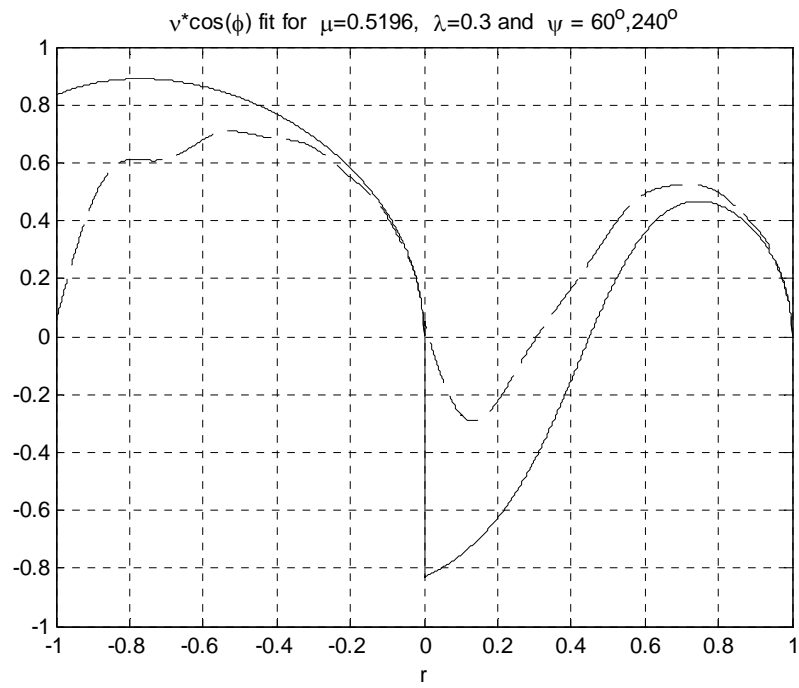


Figure F.5: $\text{Cos}(\varphi)$ fit for $\mu=0.5196$, $\lambda=0.3$, $\psi=60$ and 240° .

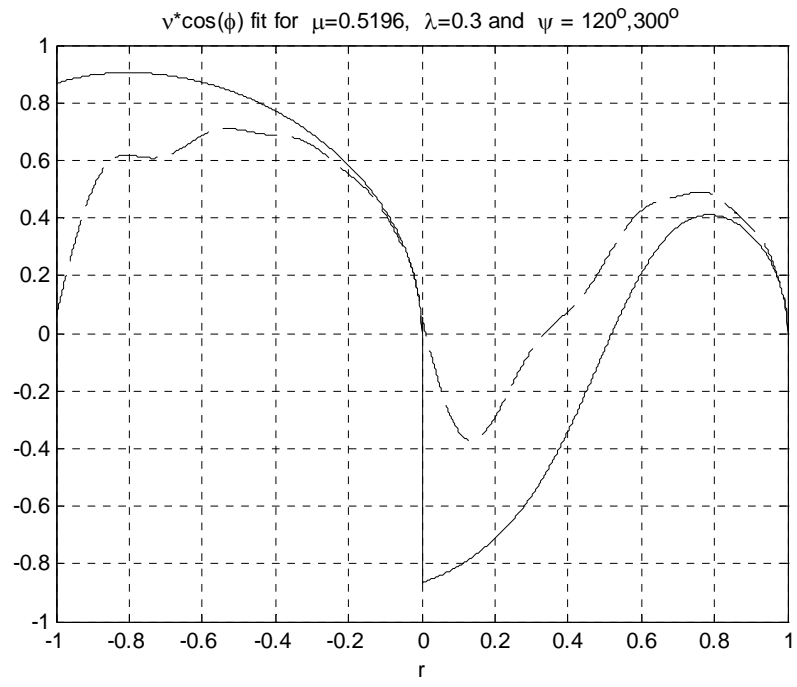


Figure F.6: $\text{Cos}(\psi)$ fit for $\mu=0.5196$, $\lambda=0.3$, $\psi=120$ and 300° .

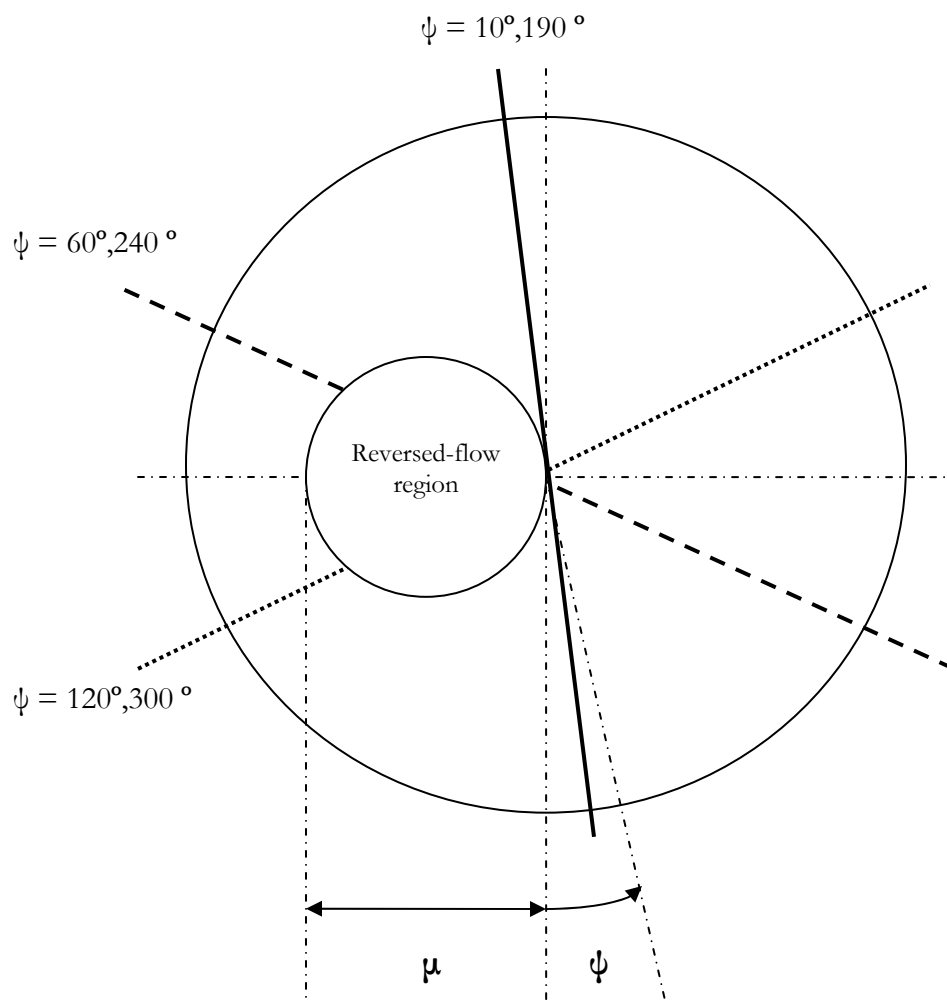


Figure F.7: Top view of Rotor. Advancing side is for $0 < \psi < 180^\circ$.

References

- [1] Pitt, Dale M., *Rotor Dynamic Inflow Derivatives and Time Constants from Various Inflow Models*. Doctor of Science thesis, Washington University in Saint Louis, December 1980.
- [2] Pitt, D.M. and Peters, D.A., "Theoretical Prediction of Dynamic Inflow Derivatives", *Vertica*, Vol.5, No.1 pp.21-34, March 1981.
- [3] Pitt, D. M. and Peters, D. A., "Rotor Dynamic Inflow Derivatives and Time Constants from various Inflow Models," 9th European Rotorcraft Forum, Stresa, Italy, September 13-15, 1983.
- [4] Chengjian, He, *Development and Application of a Generalized Dynamic Wake Theory for Lifting Rotors*, Ph.D. thesis, Georgia Institute of Technology, July 1989.
- [5] Chengjian, He and Peters, D.A., "Finite-State Induced Flow Model for Rotors in Hover and Forward Flight", Proceedings of the AHS International 43rd Annual Forum and Technology Display, Saint Louis, MO, May 18-20, 1987.
- [6] Peters, D.A. and Chengjian, He, "A Closed-Form Unsteady Aerodynamic Theory for Lifting Rotors in Hover and Forward Flight", Proceedings of the AHS International 43rd Annual Forum and Technology Display, Saint Louis, MO, May 18-20, 1987.
- [7] Morillo, J., *A Fully Three-Dimensional Unsteady Rotor Inflow Model from a Galerkin Approach*. Doctoral thesis, Washington University in Saint Louis, December 2001.
- [8] Peters, D.A. and Morillo, J., "Velocity Field Above a Rotor Disk by a New Dynamic Inflow Model", *Journal of Aircraft*, 39(5), September 2002.
- [9] Ke Yu, M., *Development of Three Dimensional State-Space Wake Theory and Application in Dynamic Ground Effect*, Doctoral thesis, Washington University in Saint Louis, August 2006.
- [10] Makinen, S.M., *Applying Dynamic Wake Models to Large Swirl Velocities for Optimal Propellers*, Doctoral thesis, Washington University in Saint Louis, May 2005.
- [11] Peters, D.A., and Makinen, SM., "A Comparison of Prandtl and Goldstein Optimum Propeller Solutions with Finite-State Dynamic Wake Models," Georgia Institute of Technology and Army Research Office 10th International Workshop on Aerolasticity of Rotorcraft Systems, Atlanta, GA, November 3-5, 2003.

- [12] Hsieh, M.A. and Peters, D.A., "Convergence and Conditioning of Dynamic Wake Models for Flight Dynamics," Proceedings of the 31st European Rotorcraft Forum, Florence, Italy, Sep 2005.
- [13] Hsieh, M.A., *A Complete, Finite-State Inflow Model for Rotors in Axial Flow*, Masters Thesis, Washington University in Saint Louis, August 2006.
- [14] Peters, D.A. and Hsieh, M.A., "Improvements to Robustness of Off-Disk Finite-State Wake Models," Proceedings of the Eleventh International Workshop on Rotorcraft Dynamics and Aeroelasticity, Boca Raton, FL, October 2005.
- [15] Glauert, H., *Aerodynamic Theory: A General Review of Progress*, volume IV, chapter Division L, Airplane Propellers. Dover Publications, Inc., New York, NY, 1963, pp. 169-368
- [16] Johnson Wayne, *Helicopter Theory*, Dover Publications, Inc., New York, NY, 1980.
- [17] Gessow, A. and Myers, Garry C., *Aerodynamics of the Helicopter*, Ungar, New York, 1952.
- [18] Betz, A., and Prandtl, L., " Schraubenpropeller mit geringstem energieverlust, " Goettinger Nachrichten, March 1919, pp. 193-217
- [19] Goldstein, S., "On the Vortex Theory of Screw Propellers," Proceedings of the Royal Society of London. Series A, Containing Papers of a Mathematical and Physical Character, volume 123. The Royal Society, April 6 1929, pp. 440-465
- [20] Harris, F.D. and McVeigh, M.A., "Uniform Downwash with Rotors Having a Finite Number of Blades", Journal of the American Helicopter Society, Vol. 21, (1), January 1976
- [21] Ormiston, Robert A., "Helicopter Rotor Induced Power, " Proceedings of the AHS International 60th Annual Forum and Technology Display, Baltimore, MD, June 8-10, 2004.
- [22] Ormiston, Robert A., "Further Investigations of Helicopter Rotor Induced Power, "Proceedings of the AHS International 61st Annual Forum and Technology Display, Grapevine, TX, June 1-3, 2005.
- [23] Wachspress, D.A., Quackenbush, T.R., and Solomon, C.L., "On Minimum Induced Power of the Helicopter Rotor", Proceedings of the AHS International 61st Annual Forum and Technology Display, Grapevine, TX, June 1-3, 2005.

- [24] Rosen, A., "Approximate Actuator Disk Model of a Rotor in Hover or Axial Flow Based on Potential Flow Equations", Journal of the American Helicopter Society, Vol. 49, (1), January 2004
- [25] I.G. Currie. *Fundamental Mechanics of Fluids*. McGraw-Hill, New York, NY, 2nd edition, 1976.
- [26] Karunamoorthy, S., Peters, D.A., Garcia-Duffy, C., "Study of Root Inflow for a Propeller Blade of Infinite Length," Proceedings of the Heli Japan 2006, Aichi, Japan, November 15-17, 2006.

Vita

Cristina Garcia-Duffy

Date of Birth	May 1, 1980
Place of Birth	Madrid, Spain
Degrees	B.S. Cum Laude, Aerospace Engineering, May 2003 M.S. Aerospace Engineering, May 2005
Professional	American Helicopter Society (AHS) American Institute of Aeronautics and Astronautics (AIAA)
Publications	<p>Karunamoorthy, S., Peters, D.A., Garcia-Duffy, C., "Study of Root Inflow for a Propeller Blade of Infinite Length," Proceedings of the Heli Japan 2006, Aichi, Japan, November 15-17, 2006.</p> <p>Peters, D.A., Garcia-Duffy, C. "Optimum Rotor Performance in Axial Flow by Finite-State Methods," Proceedings of the AHS International 63rd Annual Forum and Technology Display, Virginia Beach, VA, May 1-3, 2007.</p> <p>Peters, D.A., Garcia-Duffy, C. "Theoretical Optimum Rotor Performance in Hover and Climb," Proceedings of the AHS Aeromechanics Specialist's Meeting, San Francisco, CA, January 23-25, 2008.</p> <p>Garcia-Duffy, C., Hsieh, M.A, Peters, D.A., "A Complete, Nonlinear Induced Flow Theory for Rotors in Incompressible Flow," 27th AIAA Applied Aerodynamics Conference, June 22-25, 2009. In preparation.</p>

November 2008

Short Title: Dynamic Wake on Induced Power

Garcia-Duffy, Ph.D. 2008